Melt electrospinning using Polycaprolactone (PCL) polymer for various applications: Experimental and Theoretical analysis

by

Junghyuk Ko
BEng, University of Konkuk, 2007
MASc, University of Victoria, 2011

A Dissertation Submitted in Partial Fulfillment
of the Requirements for the Degree of

Doctor of Philosophy

in the Department of Mechanical Engineering

Supervisory Committee

Melt electrospinning using Polycaprolactone (PCL) polymer for various applications: An experimental and theoretical analysis

by

Junghyuk Ko
BEng, University of Konkuk, 2007
MASc, University of Victoria, 2011

Supervisory Committee

Dr. Martin Byung-Guk Jun
Department of Mechanical Engineering, University of Victoria, BC, Canada
Supervisor

Dr. Stephanie Willerth
Department of Mechanical Engineering, Division of Medical Science, and Department of Biomedical Engineering, University of Victoria, BC, Canada
Departmental Member

Dr. Chris Papadopoulos
Department of Electrical Engineering, University of Victoria, BC, Canada
Outside Member

Abstract

Supervisory Committee
Dr. Martin Byung-Guk Jun
Department of Mechanical Engineering, University of Victoria, BC, Canada
Supervisor
Dr. Stephanie Willerth
Department of Mechanical Engineering, Division of Medical Science, and Department of Biomedical Engineering, University of Victoria, BC, Canada
Departmental Member
Dr. Chris Papadopoulos
Department of Electrical Engineering, University of Victoria, BC, Canada
Outside Member

This thesis presents a melt electrospinning technique to fabricate highly porous and controllable poly (ε-caprolactone) (PCL) microfibers for tissue engineering applications and rehabilitation applications. Electrospinning without solvents via melt methods may be an attractive approach to tissue engineering of cell constructs where solvent accumulation or toxicity is an issue. This method is also able to produce microfibers with controllable parameters. However, the fiber diameters resulting from melt electrospinning processes are relatively large when compared to the fibers from solution electrospinning. The typical microfiber diameter from melt electrospinning was reported to be approximately 0.1mm. In order to further develop the melt electrospinning technique, we focused on the design of a melt electrospinning setup based on numerical analysis using the Solidworks 2013 simulation package and practically established a melt electrospinning setup and thermal control system for accurate experiments. One of main purposes of this thesis is the build-up of mathematical modeling to control and predict the electrospun microfiber via a more intricate understanding of their parameters such as the nozzle diameter, applied voltage, distance between the nozzle and counter electrode, temperature, flow rate, linear transitional speed, among others. The model is composed of three parts: 1) melt electrospinning process modeling, 2) fibrous helix movement modeling, and 3) build-up of microfibers modeling. The melt electrospinning process model describes an electric field, the shape of jet's continuously changing shape, and how the polymer melt is stretched into a Taylor cone and a straight jet. The fibrous helix movement model describes movement of electrospun microfibers influenced by Lorentz force, which moves along the helix pattern. Lastly, the build-up microfiber modeling describes the accumulation of the extruded microfibers on both flat and round counter electrodes based on the physical forces involved. These models are verified by experimental data from our own customized melt electrospinning setup. Moreover, the fabricated scaffolds are tested by seeding neural progenitors derived from murine R1 embryonic stem cell lines and it demonstrates the potential of scaffolds for tissue engineering applications. To increase cell attachment and proliferation, highly porous microfibers are fabricated by combination of melt electrospinning and particulate leaching technique. Finally, auxetic stretchable PCL force sensors are fabricated by melt electrospinning for hand rehabilitation. These stretchable sensors can be used to measure applied external loads or displacement and are also attachable to various substrates. We have attempted to apply the sensors to real human hand in order to prove their functionality.

Table of contents

List of Tables

List of Figures

Abbreviations

Auxetic Microfiber Sheet (AMS)
Auxetic Solid Sheet (ASS)
Computer Numerical Controlled (CNC)
Embryoid bodies (EBs)
Embryonic Stem Cells (ESCs)
Extracellular Matrix (ECM)
Micro Electromechanical Systems (MEMS)
Microfiber Sheet (MS)
One way analysis of variance (ANOVA)
Poly ε-caprolactone (PCL)
Scanning Electron Microscopy (SEM)
Solid Sheet (SS)
Standard Deviation (SD)
3-Dimensional (3D)

Acknowledgments

I would like to thank Dr. Martin Jun for their support and guidance over the course of this research. I have greatly appreciated the knowledge and experience he have shared with me. I am very grateful to have been given the chance to work on this research.

I would also like to thank Nima Khadem Mohtraram for their involvement in this research. Their knowledge in the area of cell biology and polymer was very helpful. And they offered advice through all stages of the research as a fellow researcher.

I must also extend tanks to Laboratory for Advanced Multi-scale Manufacturing (LAMM) members, which are Yonghyun, Farid, Max, Shan, Ahmad, Mohammad, Vahid, Akram, Tim, and Jason. The friendships that were made will extend well beyond the duration of our graduate careers.

Finally, I would like to thank my family for their encouraging and understanding. Their support has been fundamental.

Thank you to everyone who has helped and supported me again.

Dedication

To my family (Haecheong Park, Sungwon Ko, Sungchan Ko)……

Chapter 1. Introduction

1.1 Literature review

Tissue engineering has become an increasingly promising approach towards functional tissue repair. Injuries to the central and peripheral nervous system are an especially challenging target due to limited efficacy of current treatment methods, where the "gold standard" of nerve repair consists of invasive autografts [1]. As a result, current reviews call for the development of alternative engineered nerve conduits that can exceed or match the success rate of autografts [2]. Modern approaches to *in vitro* neural tissue engineering have utilized embryonic stem cells (ESCs) to direct differentiation into desired cell types [3]. The pluripotent nature of ESCs allows for their use in virtually any tissue engineering application, but can also present difficulties as they often times produce heterogeneous cell populations. To circumvent undesirable cell differentiation in neural tissue engineering, ESCs can be induced to form neural progenitor cells through a combination of chemical [4] and mechanical factors [5]. Chemically induced differentiation encompasses the addition of small molecules and growth factors to undifferentiated ESCs to influence gene expression. Extracellular mechanical forces exerted on the dividing cell due to topography, fiber diameter and stiffness of attachment substrate have also been demonstrated to influence ESC fate. While previous studies explored chemical models of stem cell differentiation [6], the past decade has seen increasing emphasis placed on 3-dimensional (3D) biomimetic scaffolds designed to replicate the extracellular matrix (ECM) conditional to neurogenesis [7].

Manufacturing of biomimetic scaffolds has progressed rapidly. Particulate leaching, gas foaming, fiber bonding, solid-free form fabrication, solvent casting and electrospinning are well documented techniques used to fabricate 3D biomimetic scaffolds [3, 8-10]. Electrospinning can produce scaffolds with high porosity, sub-micron fiber size and structural homogeneity [11]. The diversity of biocompatible natural and synthetic polymers conducive to electrospinning lends the technique an additional advantage when fabricating synthetic ECM [12]. Electrospinning can be accomplished through dissolving a polymer in solution or melting the polymer and the resulting polymer solution is then extruded into a fiber through use of a strong electrostatic force. When a sufficiently high force is applied to overcome the surface tension of a liquid polymer droplet, ejections of polymer solution occur from a Taylor Cone. Subsequent solidification of the polymer flow can result in fine fibers being formed as the polymer chains stretch out and orient in flight [13, 14]. While there has been a surge in solution electrospinning of biocompatible polymers over the past decade, melt electrospinning has been largely ignored.

Although solution electrospinning has been used to easily produce nanofibers from a wide variety of polymers, one of the major limitations of this technique for tissue engineering applications is the use of toxic solvents, a significant barrier to eventual clinical applications. On the other hand, melt electrospinning bypasses any toxic solvents and has been directly applied to mammalian cells in vitro. Additionally, increased stability of the fiber jet allows for far greater control over the deposition process, a point illustrated through direct writing of different polymer melts [15, 16]. Disadvantages associated with melt electrospinning include increased thermal degradation of polymer, and generally larger fiber diameters than solution electrospinning. Fiber diameter can be

controlled through various parameters in the melt-electrospinning setup: polymer viscosity, applied electrostatic force, flow rate and nozzle diameter [17]. Pioneering work by Larrondo and Manley in the early 1980s characterized dependences of fiber diameter on the applied electrical field as well as temperature and viscosity of the polymer melt [18-20]. Later studies by Zhou and colleagues demonstrated control over fiber diameter through optimization of nozzle size and temperature [17], building on the influence of polymer weight and tacticity observed by Lyon and co-workers [21].

Here, we have utilized poly (ε-caprolactone) (PCL) to produce biocompatible melt electrospun fiber mesh scaffolds using a controlled deposition process. To further optimize of melt-electrospinning parameters, modeling of melt electrospinning is necessary required for the effects of nozzle size on fiber diameter and the properties of the scaffolds. In addition, various topologies of scaffolds are fabricated based on the modelling. In order to fabricate appropriate scaffolds for specific cells, hybrid techniques mixed with the other fabrication techniques are necessary since scaffolds composed of different geometry and fiber conditions are demanded according to cell properties. In an attempt to enhance cell attachment and proliferation, additional scaffolds were coated with additives like gelatin before scaffold seeding [22, 23].

1.2 Thesis objectives

The primary aim of this work is to fabricate controlled electrospun microfibers using melt electrospinning and establish numerical modeling of the electrospun microfibers to enhance understanding of the parameters that determine fiber properties for various applications. Further, we have developed melt electrospinning technique for the specific applications and applied it to stretchable force sensors, auxetic polymeric stent, elastin

sprayed tubular scaffolds and various morphologies of scaffolds through understanding of the electrospinning process.

1.3 Novel contribution

The contribution of this thesis is the development of melt electrospinning technology for effective fabrication of biomedical scaffolds and other applications. The entire melt electrospinning setup has been built from scratch by myself. The comprehensive model for the melt electrospinning process is also developed, which involves physics of electric fields, gravity, temperatures, viscous fluid flow, etc. It will be the first model to capture the physical and geometrical aspects of the melt electrospinning process.

1.4 Thesis organization

Chapter 2 describes melt electrospinning setup and is to investigate the significant parameters associated with the melt electrospinning process that influence fiber diameter and scaffold morphology, including processing temperature, collection distance, applied voltage and nozzle size. Additionally, the porosity of scaffolds was determined by combining experimental data with mathematical modeling. To test the cytocompatability of these fibrous scaffolds, we seeded neural progenitors derived from murine R1 embryonic stem cell lines onto these scaffolds where they could survive, migrate, and differentiate into neurons, demonstrating the potential of these melt electrospun scaffolds for tissue engineering applications.

Chapter 3 is to establish mathematical modeling enables a better understanding of the parameters that determine the topography of scaffolds. We modeled two types of mathematical modeling: i) the melt electrospinning process by incorporating parameters

such as nozzle size, counter electrode distance, applied voltage that influences fiber diameter and scaffold porosity. ii) the accumulation of the extruded microfibers on flat and round surfaces using data from the microfiber modeling. These models were validated through the use of experimentally obtained data.

Chapter 4 describes the development of a novel mathematical model using numerical simulations to demonstrate the effect of temperature, feed rate and flow rate on controlling topographical properties such as fiber diameter of these electrospun fibrous scaffolds. Helix movement modeling and scaffold modeling are added to the previous models, which are described in Chapter 3, to further understand the effect of operational parameters on these properties of microfiber scaffolds. Our novel mathematical model can also predict the topographical properties affected by key operational parameters such as change in temperature, flow rate and feed rate.

Chapter 5 describes the combination with melt electrospinning and particulate leaching technique to fabricate highly porous poly (ε-caprolactone) (PCL) fibers. Water soluble sugar particles are added into PCL prior to melt electrospinning. Various sugar concentrations are added to PCL to determine the effect of increasing sugar concentrations on fiber porosity.

Chapter 6 describes the fabrication of novel stretchable Poly (ε-caprolactone) (PCL) force sensors. PCL sensors made of laser-machined PCL microfiber sheet, laser-machined PCL sheet, no machined PCL microfiber sheet, and no machined PCL sheet have been fabricated. Subsequently, these sensors were coated with gold particles to make them conductive for the electrical current resistance assays. Under the auxetic effect of materials patterned geometrical structure is automatically adjustable with

strength and thickness in response to applied forces because having memory ability to return to its neutral state on dissipation of the stresses. This stretchable sensor could be possibly manageable by applied external loads or displacement and also be attachable on the desired substrate. In order to verify our desired sensors working practically, we have attempted the sensors working on real human hand. To our knowledge, it is the first attempt to produce the stretchable force sensor with melt electrospinning technique.

Chapter 7 describes the fabrication and characterization of an non-woven auxetic polymer stent. It composes of three parts: i) to fabricate a polymeric sheet of electrospun microfibers of PCL using melt electrospinning, ii) to tailor auxetic geometry by micromachining on PCL and microfiber PCL sheet, iii) to roll them into a cylindrical tube to make auxetic stents. Final results for mechanical characterization and performance analysis of auxetic polymer stents are discussed.

Chapter 2. Fabrication of Poly (ε-caprolactone) microfiber scaffolds with varying topography and mechanical properties for stem cell-based tissue engineering applications[1]

2.1 Introduction

Tissue engineering often uses biomaterial scaffolds that mimic the microenvironment present in healthy tissue [22, 23]. Such scaffolds should function in a manner similar to the extracellular matrix (ECM) found in normal tissue when engineering substitutes for bone, cartilage, skin, liver and nerve [24-30]. Recently, the field has focused on developing scaffolds that induce stem cells to differentiate into desired phenotypes necessary for proper tissue formation and function [29-32]. Many techniques, including particulate leaching, gas foaming, fiber bonding, solvent casting and electrospinning, have been used to fabricate scaffolds with different morphological properties [30, 33-40]. Electrospinning offers a number of advantages over these other techniques. These advantages include controlling topography and consequently tailoring the mechanical properties of electrospun scaffolds, as well as the capability to encapsulate drugs inside fibers for controlled release applications. Electrospinning can produce fibrous scaffolds with controllable porosity, sub-micron fiber size and structural homogeneity [39, 40].

Solution electrospinning requires dissolving a polymer in solvent and then applying a high voltage to this solution to induce nanofiber formation [41, 42]. Obtaining a uniform distribution of fiber sizes can be challenging when using solution electrospinning to produce nanofiber scaffolds [43]. The process of melt electrospinning involves heating up

[1] The following chapter is from: **Fabrication of poly (ε-caprolactone) microfibers scaffolds with varying topography and mechanical properties for stem cell-based tissue engineering application**. Junghyuk Ko, et al. Accepted for publication by the Journal of Biomaterials Science Polymer Edition in 2014. Copyright Permission Approved.

the desired polymer with the resulting melt being extruded into fibers, resulting in better reproducibility than solution electrospinning [16, 21, 44]. The melt electrospinning process does not require the use of undesirable toxic solvents for dissolving polymers like solution electrospinning does [45]. More importantly, melt electrospinning enables better control of topography compared to solution electrospinning. Pioneering works by Larrondo and Manley in the early 1980s characterized dependences of fiber diameter on the applied electrical field as well as temperature and viscosity of the polymer melt [18-20]. Additionally, other researchers characterized the mechanical and structural properties of melt electrospun fibers compared to the bulk properties of the polymer and they observed that fiber orientation influenced the bulk properties of the scaffold [46, 47].

Recent tissue engineering approaches have combined embryonic stem cells (ESCs) with biomaterial scaffolds to direct differentiation into functional tissue replacements [32]. For instance, neural tissue engineering can be used to develop therapies for reconstructing damaged nerves through the use of biomaterial scaffolds and stem cells that can mimic the microenvironment present in healthy tissue [29, 32]. ESCs are pluripotent cells, having the potential to differentiate into any cell type found in body [29]. The pluripotent nature of ESCs means they can serve as a potential cell source for virtually any tissue engineering application [48]. Many studies have successfully shown that chemical cues presented by biomaterial scaffolds can promote ESC differentiation [29, 49-51]. A similar body of work demonstrates the role of physical cues presented by scaffolds such as elasticity, micro and nanostructures of these structures can influence stem cell differentiation as well [30, 52-54]. For example, aligned nanoscale topography significantly enhanced the neuronal differentiation of ESCs [30, 55]. For electrospun

fibers, these physical and mechanical factors include morphological and mechanical properties of such scaffolds, which are highly influenced by altering fiber diameter.

In this work, we used melt electrospinning to fabricate poly (ε-caprolactone) (PCL) microfiber scaffolds for ESC culture. Scaffolds made from PCL can be tailored to have different mechanical properties and exhibit long term stability when implanted in vivo [56]. The purpose of this study was to analyze the parameters that influence the microfiber morphology of these scaffolds. To our knowledge, we are unique to investigate the effect of melt electrospun microfiber diameter on the mechanical properties of the scaffolds along with their microstructure characteristics such as porosity. We determined the effect of fiber diameter on mechanical properties, such as tensile strength, the Young's modulus and strain at break, for a wide range of scaffolds as well. The influence of fiber diameter on morphological properties, such as torus volume and porosity of the scaffolds was also evaluated. Finally, ESC-derived embryoid bodies (EBs) containing neural progenitors were seeded upon the PCL microfibers to determine if these scaffolds could support stem cell culture and their neuronal differentiation. Our melt electrospun scaffolds supported cell adhesion and neuronal differentiation of ESC-derived neural progenitors. Overall, this novel combination of microfiber scaffolds and ESC-derived neural progenitors serves as a promising strategy for stem cell based tissue engineering applications.

2.2 Materials and methods

2.2.1 Melt electrospinning setup

Poly (ε-caprolactone) (PCL) (Mn ~45,000) was purchased from (Sigma Aldrich, USA) with a melting point of 60°C. A custom-made melt electrospinning apparatus (Figure 1) consisted of a computer numerical controlled (CNC) machine (K2 CNC Inc., USA), a custom-made chamber press, a syringe pump (New Era Pump Systems Inc., USA), a heating band (Orion Telescopes Inc., USA), a custom-made machined melting chamber, a custom-made collecting drum and custom-made nozzles that could be interchanged. Appendix A shows drawings of custom-made melt electrospinning setup. The flat tipped nozzles used to extrude the melt were fabricated from aluminum 6061 with internal diameters ranging from 150 to 1,700 μm ($\pm$10 μm). The custom-made nozzle was machined using a 3-axis CNC milling machine. The irradiation power used in machining the nozzles was 300 mW at a beam diameter of 3 mm. The beam was focused through a 20X microscope objective lens (Mitutoyo Co.) with a numerical aperture of 0.4. The femtosecond laser system (Spectra-Physics) operating at 800 nm with pulse duration of 120 fs and repetition rate of 1 kHz was used to produce the nozzle hole. The motion of the sample stage followed a helical path (generated using the software, GOL3D (GBC&S, France)) to ablate material from the nozzle head and cut a circular hole.

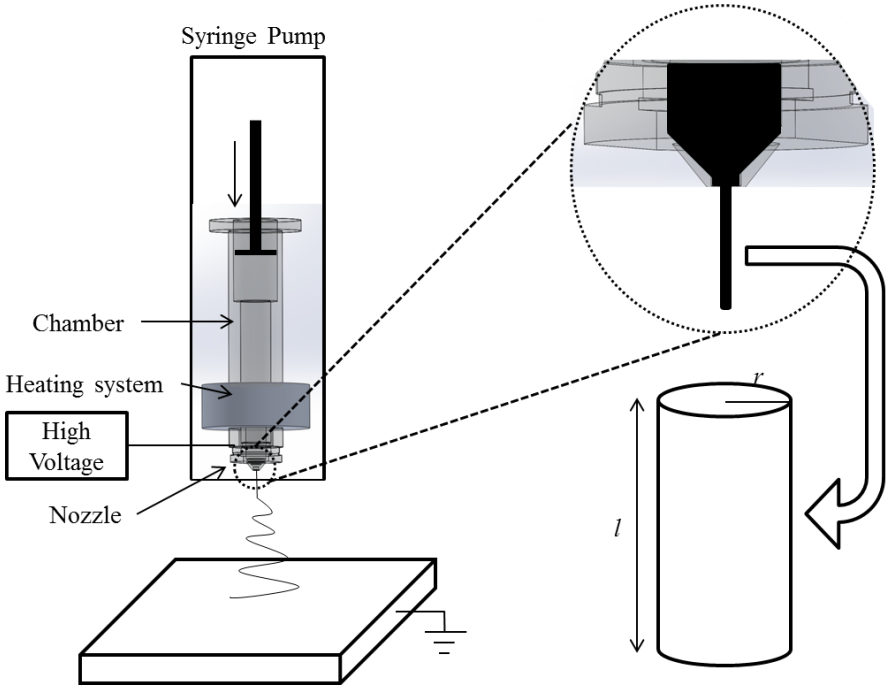

Figure 1. Schematic of custom-built melt electrospinning device

During the melt electrospinning process, 10, 15 and 20kV were applied to the molten PCL using a high applied voltage supply (Gamma High Voltage Research Inc., USA) with the working distance between the nozzle and aluminum foil collector ranging from 5 and 10cm. The PCL granules were dispensed into melting chamber with the nozzle attached and then heated to the desired temperature. The zero shear rate viscosity of PCL was measured using an ARES-G2 rheometer (TA Instruments, USA) as 291.5 Pa.sec. at 80°C using 25mm parallel plates geometry with the gap of 25mm. For the collection of randomly aligned scaffolds, a wood plate covered with aluminum foil served as the counter electrode.

2.2.2 Scaffold fabrication

Parameters related to fiber diameter and morphology of scaffold when melt electrospinning includes nozzle diameter, processing temperature, collection distance,

applied voltage, flow rate of syringe pump and linear velocity of x and y axis in CNC machine [16, 18-21, 57]. A syringe pump was mounted vertically and connected with the heated chamber, delivering molten polymer at a flow rate of 2 mL per hour. Wood plate was covered with aluminum foil in order to make conduction as a counter electrode and the foil connected to the power supply as negative charge. The nozzle was pulled away by CNC machine controller after experiments to avoid disruption to the voltage or the flow rate.

To investigate the influence of electrical force, nozzle diameter and linear velocity were respectively fixed at 200 μm and 8.5 mm/sec. To investigate the effect of temperature, the melting chamber temperature was varied from 80°C to 120°C by the temperature control system as shown in Appendix B. Based on our parameter analysis, the melt temperature was set at 80°C with an applied voltage of 20 kV and a collection distance of 5 cm when melt electrospinning scaffolds when analyzing the effect of the varying nozzle diameter. These conditions ensured proper fiber formation during the electrospinning process. Nozzle diameters ranged in size from 150 to 1,700 μm (Table 1).

Table 1. Microstructure of scaffolds fabricated at 80°C. (All data presented as the mean (n=3) ± the standard deviation)

Nozzle diameter(μm)	*Fiber diameter(μm)*	*Overlap percentage(%)*	*r(μm)*	*R(μm)*
1,700	220±9	30.1±1.2	110	1,600±60
1000	180±7	35.2±1.3	90	1,300±40
838	132±5	40.1±1.6	66	1,100±40
741	100±4	50.3±2.0	50	1,020±40
500	82±3	57.0±2.3	41	800±30
300	52±4	65.1±2.6	26	710±30

200	28±1	70.4±2.8	14	620±20
150	12±1	80.2±3.2	6	510±10

2.2.3 Mechanical properties

For further analysis, 100 x 100 mm rectangular scaffolds were fabricated using CNC machine stage and then the scaffolds were cut into 100x10 mm cuboid samples. Using a micrometer (Mitutoyo, Japan), sample thicknesses were confirmed to be 2 mm. The scaffolds were confirmed for no damage during cutting by optical microscope. Conventional macro-tensile measurements were performed using an electromechanical tensile tester (Adelaide Testing Machines, Canada). All samples were mounted between holders at a distance of 5 cm. Tensile testing was conducted at a rate of 0.08mm/s at room temperature (21°C) (n=3). The amount of strain at the breaking point was calculated using the Adelaide Testing Machines software. The Adelaide Testing machine has been used for macro scale tensile testing so it would not be able to accurately measure scaffolds with thicknesses in the range of 12-220 microns. In order to measure displacement accurately, the scaffolds were fabricated as the maximum thickness 2mm which was able to accumulate without any disturbances.

2.2.4 Analysis of microfiber topology

In order to manufacture a mesh of fibers, a CNC machine was used. The maximum speed of each axis is 8.5mm/s as controlled by G-code. PCL microfibers were transferred to loading stubs before carbon coating for imaging analysis. The Cressington 208 carbon was used to coat a 3nm thick carbon layer to non-conductive PCL fibers prior to scanning electron microscopy (SEM) imaging. The samples were carbon-sputtered two

times for 6 seconds at 10-4 mbar. The samples were loaded in a Hitachi S-4800 field emission scanning electron microscope. High magnification images were obtained at 1 kV with an 8 mm working distance. Fiber diameters, torus diameter and overlap distance were measured using Quartz-PCI Image Management Systems® in SEM as shown in Figure 2.

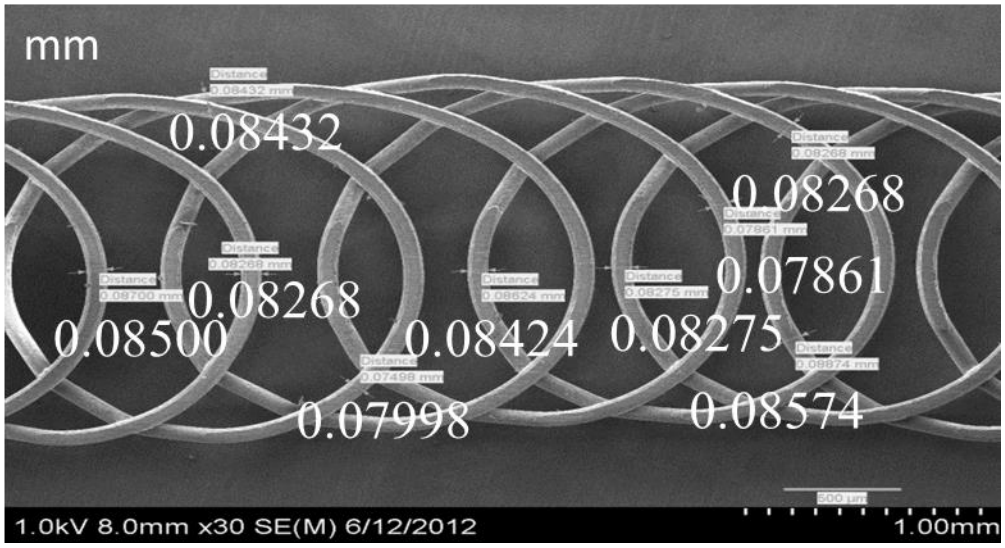

Figure 2. Scanning electron microscopy of PCL scaffolds, measuring fiber diameter using Quartz-PCI Image Management Systems® when using 500 µm nozzle at 5cm collecting distance

2.2.5 Statistical analysis

Quantitative data are presented as mean ± standard deviation (SD). The processing parameter study were screened by one-way analysis of variance (ANOVA) with the assumption of normally distributed data using Microsoft Office Excel 2010, USA; significance was defined as $p<0.05$.

2.2.6 Seeding of cells on PCL microfiber scaffolds

To determine suitability of scaffolds for stem cell culture, R1 (Nagy Lab) mouse embryonic stem cells were utilized. R1 cells were cultured upon mouse embryonic fibroblast feeder layers (Global stem, USA) to maintain pluripotency [58]. R1 cells were subsequently removed from feeder layers and cultured in suspension on agar-coated plates to form embryoid bodies (EBs) for 8 days with 0.5 μM retinoic acid being added for the last 4 days to induce neural differentiation (Sigma-Aldrich) [59]. During this process, the media is changed every 2 days and the resultant EBs contains a high percentage of neural progenitor cells. Mesh electrospun scaffolds were sterilized with ultraviolent light for 30 minutes. Individual R1 EBs were removed from suspension and seeded on sterilized scaffolds. EBs were cultured on these electrospun scaffolds for 14 days before image analysis.

2.2.7 R1 cells viability analysis

The viability of R1 EBs seeded on the scaffolds was analyzed qualitatively after 14 days using a LIVE/DEAD® Viability/Cytotoxicity Kit (Invitrogen). The kit contains a stain for viability, calcein AM, which is enzymatically converted to green fluorescing calcein by the naturally present intracellular esterase activity in live cells, and a stain for dead cells, ethidium homodimer-1, which fluoresces red upon binding to nucleic acids accessed through the ruptured cell membranes of dead cells [49]. Each well was viewed using an IncuteCyte ZOOM Essen BioScience® fluorescent microscope. Images were captured at 515 nm for green fluorescence and 635 nm for red fluorescence. Images were overlaid at layer opacity of 50%.

2.2.8 Immunocytochemistry and nucleus staining

Neuronal differentiation of R1 cells was qualitatively assessed after 14 days by immunocytochemistry targeting the neuron-specific protein β-III-tubulin. Media was removed and each well was washed with 4 mL PBS. Cells were fixed with a 10% formalin (Sigma) solution for 1 hour at room temperature and then permeabilized with 0.1% Triton-X (Sigma) solution for 45 minutes at 2 – 8 ˚C. Wells were then blocked with 5% normal goat serum (NGS, Millipore) at 2 – 8 ˚C for 2 hours. The primary antibody for β-III-tubulin (Millipore) was added to each well and incubated at 2 – 8 ˚C for up to 15 hours. Three washes with PBS were performed and the Alexafluor488-conjugated secondary antibody at a concentration of 10 µg/mL was added and incubated, protected from light exposure, at room temperature for 4 hours. Cells were washed three times with PBS to remove unbound antibody. Hoechst 33342 nucleic acid stain, 1µl in 300µl PBS was added into the last PBS wash after secondary antibody. Images were captured for green and blue fluorescence. Images were overlaid at layer opacity of 50%. Higher magnification fluorescent images were acquired on a LEICA 3000B inverted microscope using an X-cite series 120Q fluorescent light source (Lumen Dynamics) coupled to a Retiga 2000R fast cooled mono 12-bit camera (Q-imaging).

2.3 Simulation and experiment results

2.3.1 Effects of temperature on fiber diameter

The effects of changing the temperature of the melt from 80°C to 120°C were investigated. Figure 3(A) represents analysis of temperature and fiber diameter. Increasing temperature led to a significant increase in the fiber diameter when nozzle size

was held constant. Fiber diameters were varied from 28 ± 1 μm at 80 °C temperature to 40 ± 2 μm for 120 ° C temperature (average ± SD) using 200 μm nozzle and 52 ± 4 μm at 80 °C to 58 ± 6 μm for 120 ° C using 300 μm nozzle in various temperatures.

Additionally, temperature influenced the speed of spinning fibers due to the density changes. This speed played a key role in controlling the morphology of scaffolds. Table 2 showed fiber weights depended on temperature for 600 seconds using 200 μm nozzle. Velocity ($\frac{dl}{dt}$) of polymer extrusion was calculated by the following equation:

$$\frac{dV}{dt} = \pi r^2 \frac{dl}{dt} = \frac{1}{D}\frac{dm}{dt} \quad (1)$$

where V was total volume of electrospun fibers for 600 seconds, m was total weight of electrospun fibers, r was fiber radius, t was time of electrospinning, and density (D) of PCL polymer as a function of temperature calculated by [60]

$$D = 0.9049e^{(6.392*10^{-4}*T)}/V(0,T) \quad (2)$$

where, T was temperature in degrees Celsius, the zero-pressure isobar V(0,T) equaled A0+A1T+A2T2 (A0=9.9868*10-1, A1=8.1076*10-3, A2=7.0243*10-5 were specific constants for a given polymer [61]).

Table 2. PCL fiber properties depended on temperatures (spinning time: 10minutes using 200 μm nozzle) (n=3)

Temperature(°C)	80	90	100	110
Weight(g)	0.11±0.03	0.32±0.05	0.72±0.04	1.18±0.06
Fiber diameter(μm)	28±1	31±1	33±1	37±1
Density(g/cm^3)[60]	0.4542	0.4172	0.3840	0.3543

As shown in Figure 3(B), the velocities increased when temperatures increased because of low density and viscosity. The velocity was varied from 16.7 ± 6.2 to 119.5 ±

7.1mm/s ($p<0.05$) using 200 μm nozzle in various temperatures. Based on these results, morphology of scaffolds was able to be controlled variously through x and y axis speed controls.

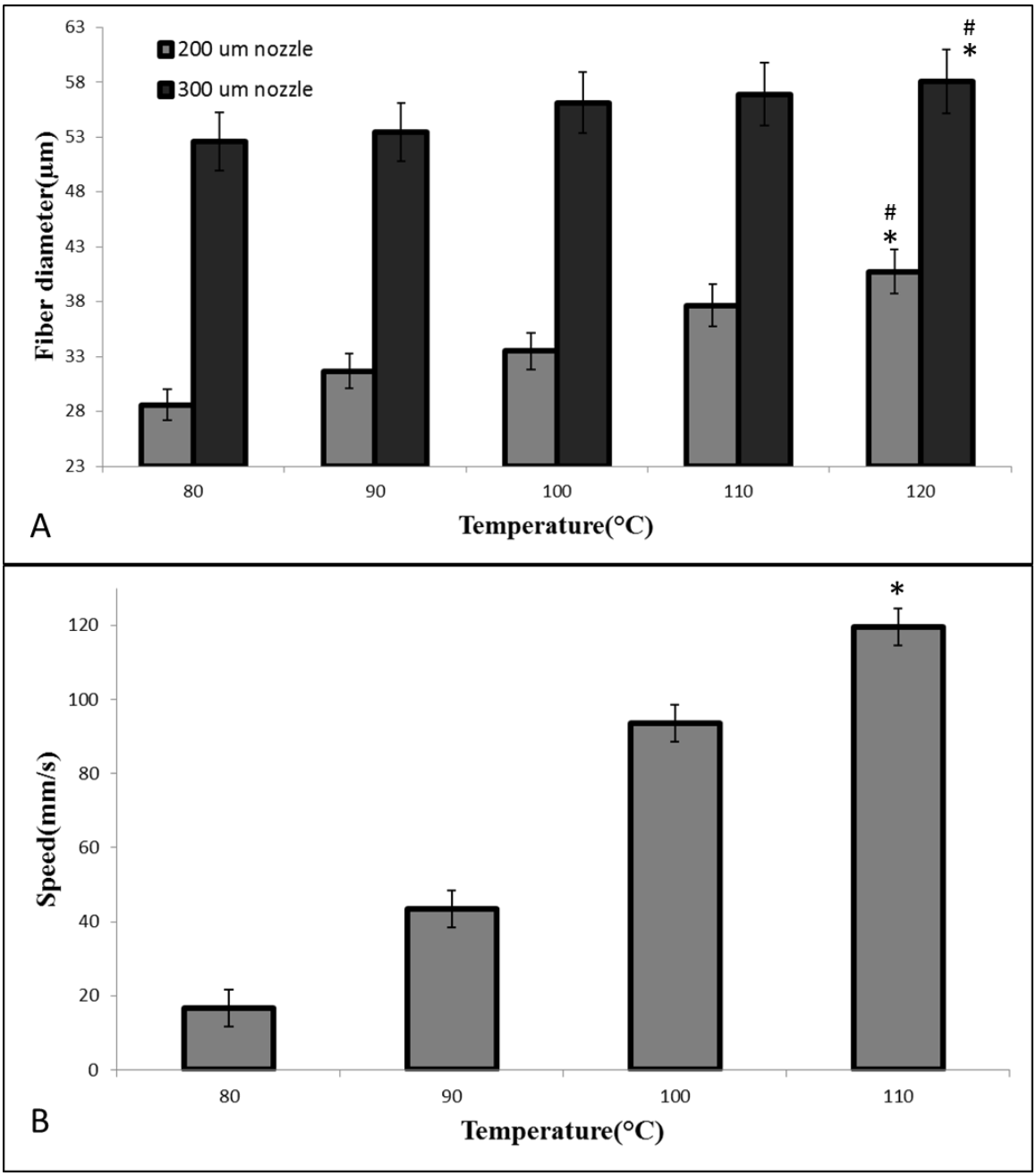

Figure 3. A) The effect of temperature on the resulting fiber diameter and (B) The effect of temperature on speed of polymer extrusion under various temperatures using 200 μm

nozzle. (n=3 for both studies) * indicates p<0.05 versus all other temperatures. # indicates p<0.05 versus the other nozzle in each temperatures.

2.3.2 Effects of distance, applied voltage and chamber temperature on fiber diameter

Figure 4 showed the effect of distance between nozzle, counter electrode and applied voltage and chamber temperature on fiber diameter. According to Coulomb's law, magnitude of the electrical force was directly proportional to applied voltage and inversely proportional to the distance. Fiber diameter showed 49 ± 5 μm at 10kV and 28 ± 4 μm at 20kV in 5cm and 80°C. When distance was increased from 5cm to 10cm at 20kV and 80°C, fiber diameter demonstrated 49 ± 5 μm at 5cm and 93 ± 12 μm at 10cm Moreover, the diameters were changed from 49 ± 5 μm to 58 ± 3 μm when the chamber temperature was increased from 80 degree to 90 degree at 10kV applied voltage and 5cm distance. Fiber diameters increased in size by approximately 1.6 times when the collecting distance was doubled and also were increased from approximately 6% to 13% when chamber temperature was changed from 80 degree to 90 degree at different voltage and distance. However, when applied voltage was doubled, the fiber diameters decreased to half their original size.

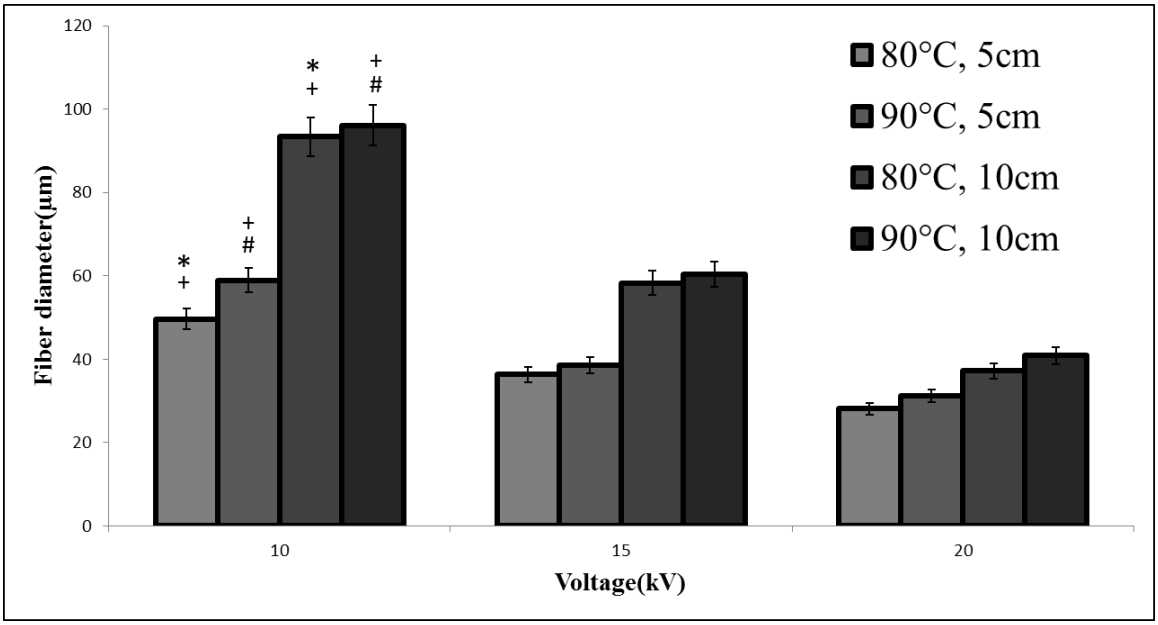

Figure 4. The effects of collection distance, temperature and applied voltage on the resulting fiber diameter using 200 μm nozzle (n =3), * indicates p<0.05 versus other distance at 80°C. # indicates p<0.05 versus other distance at 90°C. + indicates p<0.05 versus all other voltages.

2.3.3 Effects of nozzle diameter

The nozzle diameter controlled initial diameter of fibers when using direct deposition melt electrospinning. The fiber diameter then shrunk due to the electrical force and gravity after the spinning process. Figure 5 showed the relationship between nozzle diameter and fiber diameter in experiments. The fiber diameter increased from 12 ± 1 μm to 220 ± 9 μm as the nozzle diameter increased from 150 μm to 1,700 μm. The distance between nozzle and colleting plate and the voltage were respectively fixed at 5cm and 20kV in order to restrict parameters related to fiber diameter.

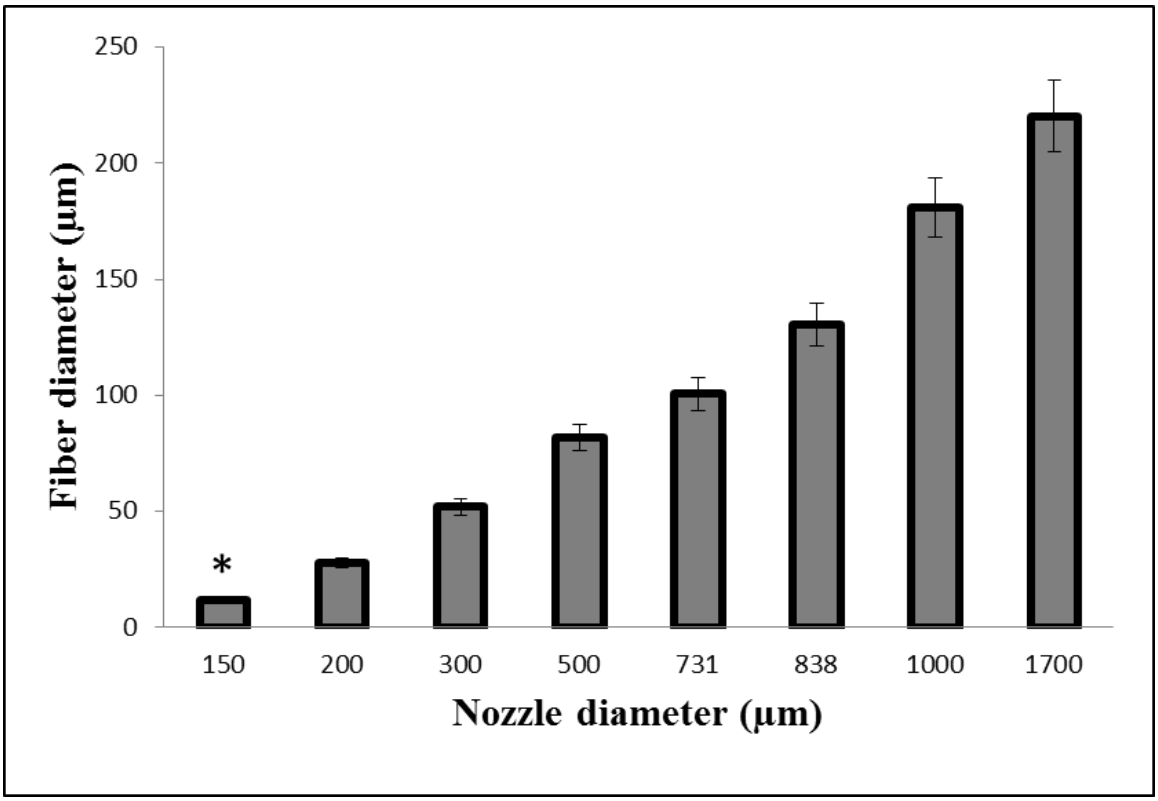

Figure 5. The effect of nozzle diameter on fiber diameter when melt electrospinning process occurs at 5cm distance, 20kV voltage, and 80°C. (n=3) * indicates p<0.05 versus all other nozzles

2 mm thick scaffolds were fabricated for testing of mechanical properties using various diameter nozzles from 150 to 1,700 µm. Depending on the fiber diameter, the resulting scaffolds contained a different number of layers. 100 x 100 mm rectangular scaffolds were fabricated using CNC machine stage and then cut them with a sharp blade as 30 x30 mm sample. The speed of vertical and horizontal movement in CNC machine was 8.5 mm/s in the 3-axis machine. Figure 6 shows the overlapping topography depended on nozzle diameter. The overlap percentage varied from 78 ± 8 % to 20 ± 10 % as the nozzle diameter changed from 150 µm to 1,700 µm. Smaller nozzle diameter resulted in a larger overlap percentage.

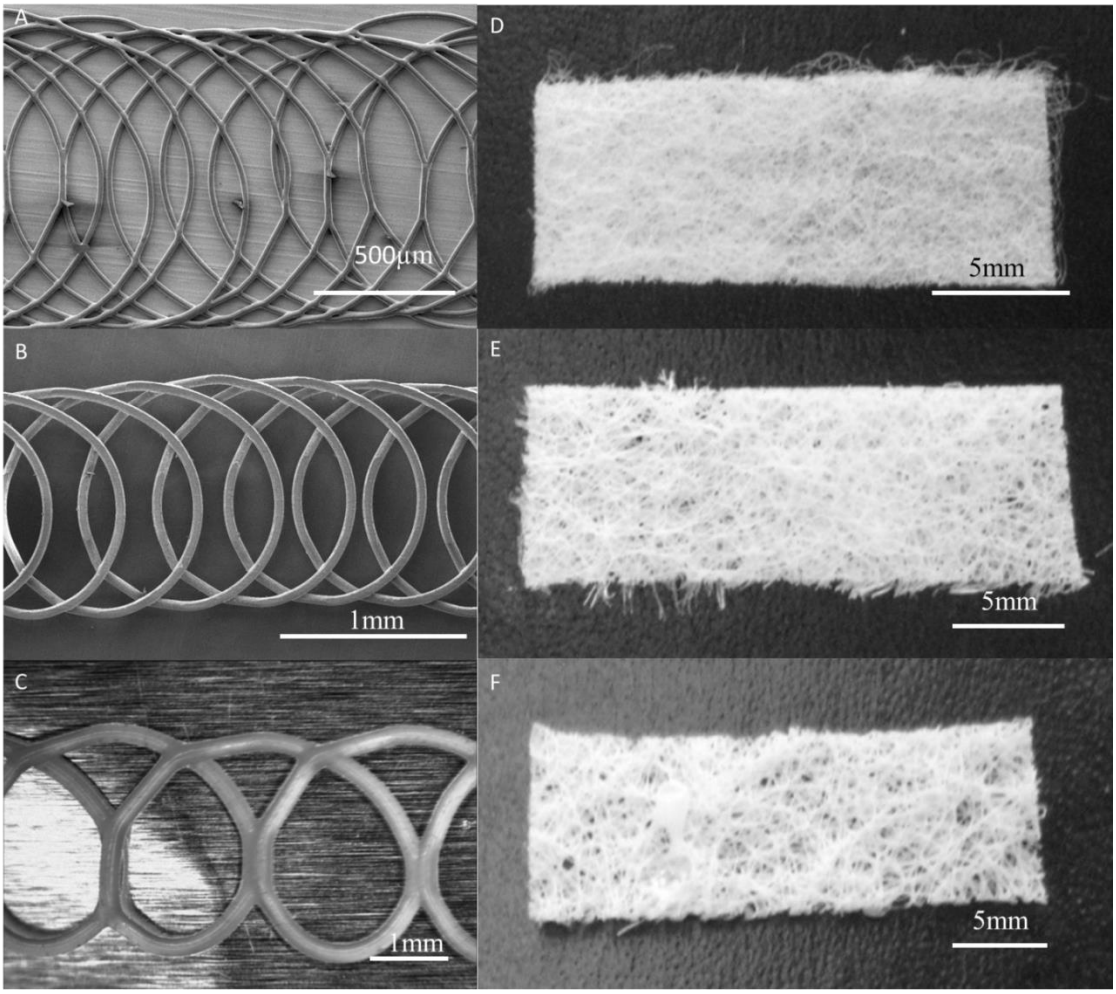

Figure 6. SEM images, optical microscope image and digital camera images of coiled loop microfiber depended on nozzle diameters at 80°C, 5cm, and 20kV; (A)-(D) 12μm diameter using 150 μm nozzle, (B)-(E) 82 μm diameter using 500 μm nozzle, and (C)-(F) 220 μm using 1,700 μm nozzle. (n=3)

2.3.4 Scaffold porosity

Due to an inability to collect data on the scaffold porosity directly, we combined experimental data with the following equations to determine a theoretical porosity for the scaffolds fabricated using different nozzle sizes. The theoretical porosity was calculated based on estimation of fiber diameter, overlap area, and total volume of PCL microfibers. Figure 7(A) showed schematic mesh morphology and overlap calculation. They were

assumed that the scaffold was cube-shaped, composed of perfect circular cylindrical microfibers called torus. Table 1 contained the experimental data determining the torus overlap for each scaffold based on SEM images.

The porosity of scaffold was defined by [45]

$$\emptyset_{\mathrm{mesh}} = \left(1 - \frac{\mathrm{NV_t}}{\mathrm{V_s}}\right) \times 100\% \tag{3}$$

where, $\emptyset_{\mathrm{mesh}}$, $\mathrm{V_t}$, $\mathrm{V_s}$, N were respectively porosity of mesh, volume of torus, volume of whole scaffold, and number of torus. The torus volume was calculated by

$$\mathrm{V_t} = 2\pi^2 \mathrm{R r^2} \tag{4}$$

where, R was distance from the center of the tube to the center of the torus and r was the radius of the fiber. The volume of whole scaffold was determined by

$$\mathrm{V_s} = \mathrm{w_1 w_2 H} \tag{5}$$

where, $\mathrm{w_1}$, $\mathrm{w_2}$, H were respectively scaffold width, scaffold length, and scaffold height. The number of torus and overlap percentage was able to be calculated by

$$\mathrm{N} = \left\{\frac{\mathrm{w_1}}{2(\mathrm{R+r})}\left(1 + \mathrm{O_p}\right)\right\}\left\{\frac{\mathrm{w_2}}{2(\mathrm{R+r})}\left(1 + \mathrm{O_p}\right)\right\}\left\{\frac{\mathrm{H}}{4\mathrm{r}}\right\}, \mathrm{O_p} = \frac{\mathrm{A_2}}{\mathrm{A_1}} \times 100(\%) \tag{6}$$

where, $\mathrm{O_p}$ was overlap percentage. As shown in Figure 7(A), circle area ($\mathrm{A_1}$) and overlap area ($\mathrm{A_2}$) were defined by

$$\mathrm{A_1} = \theta \mathrm{R_1^2}, \mathrm{A_2} = \mathrm{R_1^2}\left(\theta - \frac{1}{2}\sin(2\theta)\right) + \mathrm{R_2^2}\left(\alpha - \frac{1}{2}\sin(2\alpha)\right) \tag{7}$$

where, $\theta = \cos^{-1}\left(\frac{\mathrm{R_1^2 - R_2^2 + d^2}}{2\mathrm{R_1 d}}\right), \alpha = \cos^{-1}\left(\frac{\mathrm{R_2^2 - R_1^2 + d^2}}{2\mathrm{R_2 d}}\right)$, α and θ were radian. d was a distance between two centers of circles. According to the assumption which was regular perfect circles, the radius of circles (R = R1 = R2) and the angles were same as well (θ = α) in Figure 7(A).

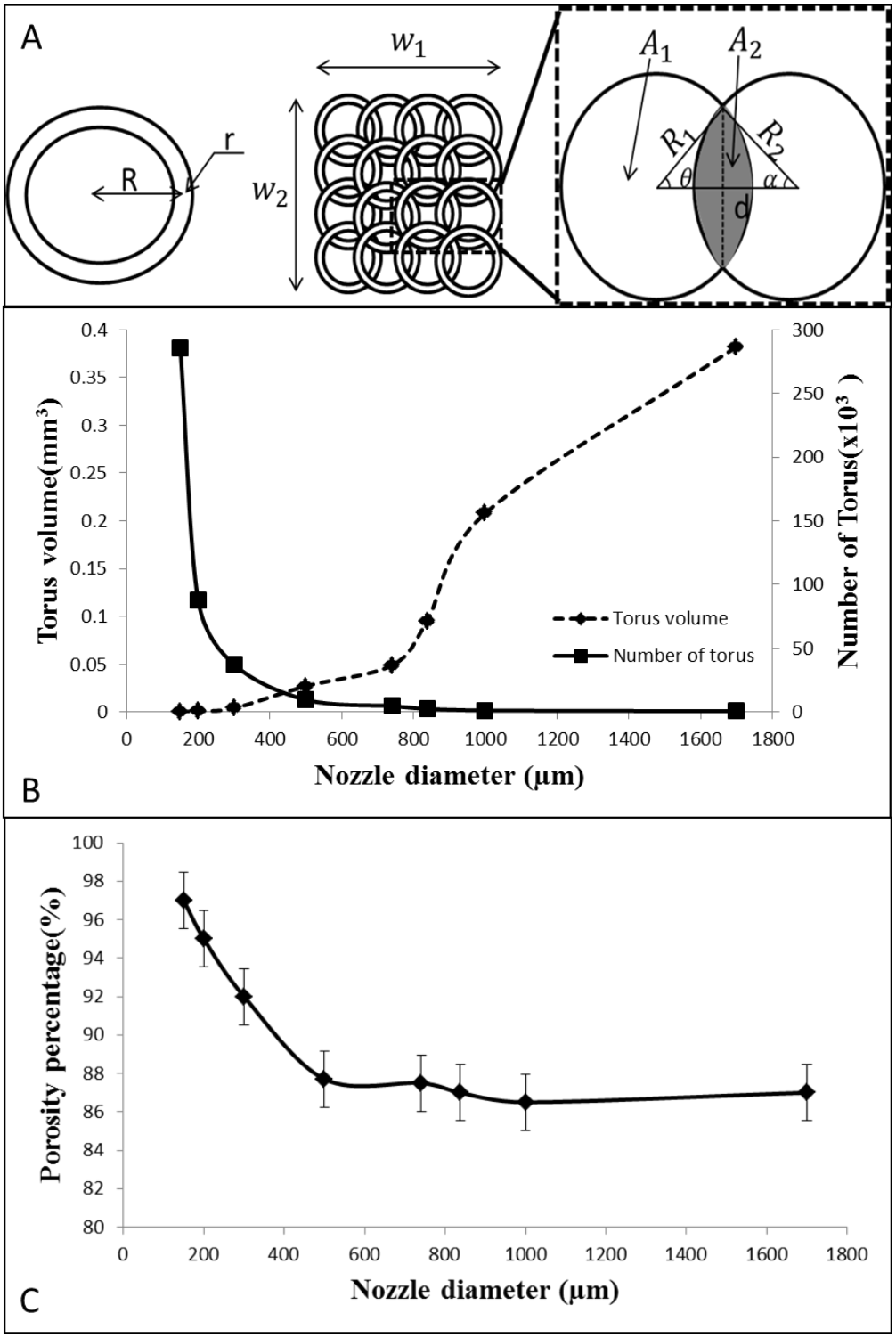

Figure 7. (A) A schematic showing the mesh morphology produced by melt electrospinning and how the degree of overlap was calculated, (B) Torus volume and Number of Torus in various nozzle diameter, (C) Theoretical porosity of scaffolds.(n=3)

By using the parameters mentioned above, the resulting diameters of the microfibers were shown in table 1 demonstrates the result of torus parameters from SEM images. Thus, the theoretical porosity from Eq. (1) was shown in Figure 7(B) and (C). The significant factors to determine porosity were torus volume (V_t) and number of torus (N). The increment of number of torus and the decrement of torus volume were very similar from 1,700 μm to 500 μm so the Figure 7(C) showed flat in the section. However, the decrease in torus volume occurred more rapidly than the increase in the number of torus from 300 μm to 150 μm so the porosity increased.

2.3.5 Macro-tensile measurements

The mechanical properties including elastic modulus and strain at break were influenced by the fiber diameter. The elastic modulus decreased as the fiber diameter decreases. Nevertheless, the mechanical properties change considerably due to the wide range of fiber diameters produced (12 to 220 μm).

As fiber diameter decreased, strain at break increased as shown in Figure 8. This dependency of mechanical properties of microfibers on fiber diameter resulted from differences in breaking mechanisms. When we applied a displacement on the electrospun mesh scaffolds, the scaffold elongated in the direction of displacement as they were stretched uniaxially. The scaffold composed of thicker fibers had property of higher Young's modulus and lower strain at break while the scaffold composed of thinner fibers had a lower Young's modulus and higher strain at break. For instance, an 18% decrease in fiber diameter from 220 μm to 180 μm led to an increase of almost 7% of in the strain at break and 9% of decreased in Young's modulus of fiber.

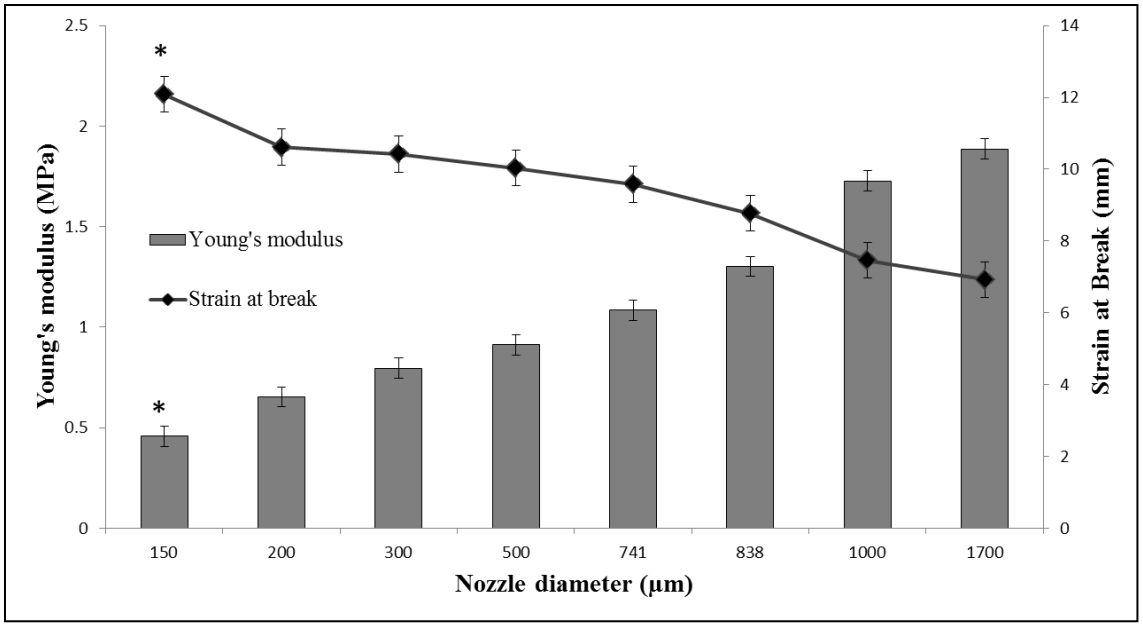

Figure 8. Mechanical properties of microfiber scaffolds using various nozzles (n=3), * indicates p<0.05 versus other nozzle diameters

2.3.6 Seeding embryoid bodies on microfiber scaffolds

The ability of these microfiber scaffolds to serve as a stem cell culture substrate was examined through cell seeding experiments. ESC-derived neural progenitors adhered to these scaffolds and neuronal differentiation from seeded EBs can be observed after 14 days of culture. Figure 9 shows the results of the cell viability analysis and differentiation of neural progenitors into neurons when seeded upon melt electrospun scaffolds. Figure 9A shows a bright field image of the individual EB. Figure 9B shows the superimposed image of live and dead cells. Live cells are present in whole EBs on the scaffold. Migration of live cells along the microfibers that make up the scaffold topography was shown. Figure 9C is the same image without the phase contrast. These images verify that cells migrated from the EB along the direction of scaffold topography.

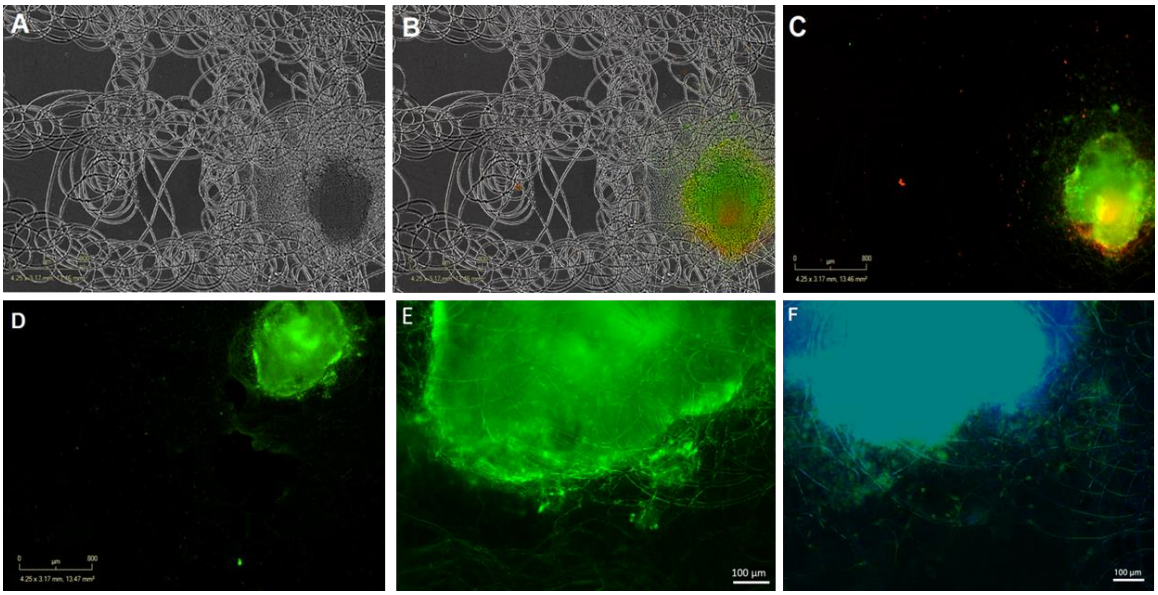

Figure 9. Live/dead analysis and differentiation of neural progenitors into neurons when seeded upon melt electrospun scaffolds after 14 days of culture. A) Bright field image. B) Superimposed image of live and dead cells over the phase contrast image. C) Superimposed image of live and dead cells without the phase contrast image superimposed. Scale bars represent 800µm. D and E) Immunohistochemistry performed on R1 EBs after 14 days of culture on mature cell marker Tuj1 expressed by neurons. F) Superimposed image of Tuj-1 and Hoechst 33342 nuclear marker. A 0.200 mm nozzle was used for fabricating a mesh scaffold at 80°C, 5cm, and 20kV.

Immunostaining against the neuronal marker Tuj1 and staining using the nuclear marker Hoechst 33342 were performed after 14 days. Figures 9D and 9E show the neuronal differentiation of R1 cells with different magnification. The higher magnification image was taken using a LEICA DMI 3000B fluorescent microscope. Figure 9F shows the cell bodies based the presence of nucleus maker co-localized with the microfiber scaffold. Neurite outgrowth can be clearly seen. These images display a clear neuronal phenotype differentiated from the R1 EBs seeded on PCL microfiber scaffolds. Melt electrospinning microfibers support and direct R1 cell adhesion and can thus be seen as a suitable tool for tissue engineering.

2.4 Discussion

Electrospinning of polymeric fibers can be accomplished either using a polymer solution or melt to fabricate fibers in the range of few nanometer over few hundreds micrometer [40]. Although fabrication of microfibers through the use of solution electrospinning is possible, controlling the uniform distribution of fiber's diameter and also the architecture of scaffolds remains challenging [42]. The diameter of fibers can be manipulated by controlling the parameters of polymer solution and spinning operation. For instance, it has been shown that by changing the concentration of Polyethersulfone (PES) solution, PES fibers can be produced in the range of 283 ± 45 nm to 1452 ± 312 nm [53]. Similar to other studies of solution electrospinning [43], these results showed a poor uniform distribution of fiber diameter [53]. Yoshimoto et al. reported a broad fiber diameter distribution for PCL nanofibers (400nm ±200 nm) [37]. This variation in diameter may be due to the fast phase separation of PCL and the uncontrollable evaporation of volatile solvent during electrospinning. Using melt electrospinning, we could produce fibers with the average diameter of 12 ± 1μm at 80°C when using the 150 μm nozzle. A very fine fiber size distribution has been achieved for all of microfiber scaffolds produced by different nozzles. Fibers were fabricated with diameter in the range of 12 ± 1 μm to 220 ± 9 μm at 80°C. Therefore, this excellent degree of reproducibility would lead us to engineer polymeric microfibers according to the desired fiber diameter and its uniform distribution. However, it is limited to fabricate smaller fibers using melt electrospinning since flow resistance becomes dramatically high when nozzle diameter is smaller than 150 μm.

In addition to controlling fiber diameter and fiber size distribution, the other prominent property of scaffolds is controlling the architecture of scaffolds and their consequent porosity. Although there have been many studies on controlling the topography of fibers fabricated by solution electrospining, challenges remain in terms of being able to control and predict the topography of solution electrospun fibers [62]. On way to control the topography of nanofibers is using a rotating drum to collect aligned nanofibers [39, 42]. The technique has shown limitations since the higher speed of drum would lead to induce a tensile force which could break the nanofibers and eventually disturbed fine control of fibers orientation [39]. Therefore, by using melt electrospinning one can control all topographical properties in a perfectly controlled way. By means of computer aided design (CAD), different structures can be fabricated [16]. Preventing fiber breakup, and bead forming, which are really tough to achieve in the case of solution electrospining, can be easily controlled by tuning melt electrospinning parameters including processing temperature, collection distance, applied voltage and nozzle size. Our on-going research is the fabrication of uniaxial and biaxial aligned microfiber scaffolds with very fine fiber size distribution.

Generally, the mechanical properties of electrospun fibers can be influenced by different parameters including the fiber diameter, topography and porosity, physical and chemical properties of the processed polymer such as polymer molecular weight and its distribution [47, 63]. Here, we have mainly focused on the control of fiber diameter over mechanical properties of PCL microfibers scaffolds. Our results showed that varying the porosity range from 75% to 92% lead to significant change in yield strength from 0.457 MPa to 1.886 MPa depended on nozzle diameter used to fabricate the scaffold. As

expected when the fiber diameter decreased, porosity of scaffold increased and which consequently would lead to decrease in Young's modulus. Croisier et al. performed the macro-tensile measurements on PCL fiber scaffolds fabricated by solution electrospinning using a higher molecular weight of PCL compared to our study [63]. Their results showed a Young′s modulus of 3.8 ± 0.8 MPa for nanofibers which is higher compared to 0.457 ± 0.042 MPa. This suggests that in addition to the fiber diameters, other parameters such as polymer molecular weight play a key role in controlling mechanical properties. According to our results, Young's modulus was varied from 0.457 MPa to 1.886 MPa, 75.77% increase, but strain at break was alternated from 12.08 mm to 6.92 mm, 42.72% decrease, when nozzle diameter was increased from 150 μm and 1,700 μm.

However, the mechanical properties are affected by a combination of many factors: porosity of fiber mat, fiber diameter, friction between fibers, thickness of fiber mat, and geometry [64]. We are able to fabricate scaffolds which have various mechanical properties in Young's modulus and strain at break.

Pluripotent stem cell lines can be differentiated into any of the specific cell lineages found in an organism, including those found in neural tissue [29, 50, 65]. One major type of pluripotent stem cells is ESCs isolated from the inner cell mass of blastocysts. One of the major challenges when differentiating pluripotent stem cells is how to control this process to produce the desired cell phenotypes. For example, when developing pluripotent stem cell therapies for the treatment of spinal cord injuries, it is desirable to produce neurons [65]. Neuronal differentiation of pluripotent stem cells can be achieved through the presentation of physical cues such as scaffold elasticity and topography [36-

39, 66]. For example, aligned nanoscale topography can significantly enhance the neuronal differentiation of ESCs [37, 39]. Electrospun scaffolds fabricated by solution electrospinning have been extensively evaluated for their use in neural tissue engineering applications [39]. Our versatile technique to fabricate biocompatible microfibers via melt electrospinning provided a good degree of reproducibility to control the fiber diameter with the aim of supporting stem cell growth, adhesion, viability and neuronal differentiation. PCL electrospun microfibers have recently shown their potential for the adhesion and proliferation of human dermal fibroblasts [67]. Also it has been reported that periodontal ligament fibroblast cell can be adhered to a sheet of hybrid biomodal PCL melt and solution electrospun fibers sheet [67]. Our work combining stem cells and melt electrospun fibers demonstrates an alternative method of producing biomimetic scaffolds for neural tissue engineering applications without the need for toxic solvents. In this thesis, we showed proof-of concept data that such scaffolds can be combined with ESC-derived embryoid bodies (EBs) containing neural progenitors to support stem cell culture and their neuronal differentiation. Our on-going studies will focus on quantifying the effect of topographical properties on the neuronal differentiation of ESC-derived embryoid bodies. Here, neuronal differentiation and outgrowth from EBs were observed, suggesting the influence of topography serves as a physical cue for stem cell-based tissue engineering strategies. We demonstrated, for the first time, that electrospun PCL microfibers could support the neuronal differentiation of ESC-derived neural progenitors.

2.5 Conclusion

While melt electrospinning, using different sized nozzles for extrusion enable fabrication of scaffolds with different fiber diameters. We can control the PCL fiber

diameter by varying the processing temperature, the collecting distance and applied high voltage between nozzle and counter electrode, and nozzle diameters. This work characterizes PCL scaffolds fabricated using melt electrospinning both in terms of topography and mechanically. These scaffolds possess an open porous network with porosity ranging from 75% to 92% and yield strength from 0.457 MPa to 1.886 MPA depended on nozzle diameter used to fabricate the scaffold. As expected when the fiber diameter decreases, porosity of scaffold increases. The yield strength decreases when fiber diameter decreases, while strain at break increases when fiber diameter decreases because of flexibility. Finally these scaffolds are clearly able to support murine embryonic stem cell adhesion and differentiation, making them a useful tool for tissue engineering applications.

Chapter 3. Using Mathematical Modeling to Control Topographical Properties of Poly (ε-caprolactone) melt electrospun scaffolds[2]

3.1 Introduction

As one of the most commonly used polymer processing techniques, electrospinning is currently used to fabricate nano to micro scale fibers as scaffolds for biomedical applications [16, 68, 69]. In the 1980s, the first melt electrospinning setup was built [21, 70, 71] and since then more than 50 polymers have been successfully spun into fibers through this technique [45, 72-74]. In the melt electrospinning process, electric charges are applied to the polymer melt while providing a strong tensile force to stretch out fibers from the viscoelastic flow of polymer melt. Consequently, a jet of polymer melt is pulled from a meniscus formed at nozzle tip. The polymer chain entanglements within the melt prevent the electrospinning jet from breaking up. The molten polymer cools and solidifies to yield fibers on a collector plate. To date, there have been a number of papers and experiments dedicated to produce fibers ranging in diameter from a few nanometers to several micrometers using this technique [16, 18-20, 57, 69, 75-77]. These nonwoven collected random fibrous structures can potentially be used in a variety of biomedical applications such as wound dressings, vascular grafts and tissue scaffolds [78, 79]. Compared to the other techniques of scaffold fabrication such as solution electrospinning, particulate leaching and solvent casting, virtues of melt electrospinning include an excellent degree of reproducibility for controlling topography and consequently tailoring the mechanical properties of electrospun scaffolds [16, 68, 69]. Further, melt

[2] The following chapter is from: **Controlling Topographical Properties of Poly (ε-caprolactone) Melt Electrospun Scaffolds through Mathematical Modeling**. Junghyuk Ko, et al. Accepted for publication by the Journal of Micromechanics and Microengineering in 2014. Copyright Permission Pending.

electrospinning does not require the use of toxic solvents to produce biocompatible scaffolds. More interestingly, a variety of topographies can be implemented through melt electrospinning based on the desired application. For instance, Dalton et al. fabricated different structures to serve scaffolds and they could control the topographical properties in a reproducible and controlled way [16, 44, 68].

Recent studies have explored the effect of the nozzle diameter, nozzle temperature and spinning temperature on controlling topographical properties such as fiber diameter and porosity [16, 44, 68]. The parameters affecting electrospinning and the fibers are the rheological properties of polymer melt flow and processing conditions such as applied voltage, temperature and counter electrode distance, and ambient conditions. With the understanding of these parameters, it is possible to come out with setups to yield fibrous structures of various forms and arrangements and to create microfiber with different morphology by varying the parameters.

Melt electrospinning is an important polymer processing technique but a poorly understood one in terms of modelling. Most studies investigate phenomenological models of polymer behaviour through the process of melt electrospinning [18-20, 41, 80, 81]. Although brilliant results have been achieved in terms of microstructure physical properties such as crystallinity, there is a need to design more practical models to control the desired microstructure topographical properties of electrospun fibers. For instance, Zhmayev and Joo have a model which analyzes the polymer melt behaviour of nylon through its flow induced crystallization properties [80, 81]. In another work by Zhmayev, the stable jet region in melt electrospinning has been reported [80]. The results showed a

good similarity when the comparison between the final jet diameter and the average thickness of collected fibers have been studied.

Here, we present our geometrical model based on, key parameters of melt electrospinning to predict the topographical features of such scaffolds, including fiber diameter and porosity. To our knowledge, there is a lack of research for linking the prominent parameters of melt electrospinning, such as applied voltage and counter electrode distance to topographical properties. In our previous study, we could successfully control the poly (ϵ-caprolactone) (PCL) fiber diameter by varying the processing conditions such as temperature, the collecting distance, and applied high voltage between nozzle and counter electrode, and nozzle diameters [69]. PCL is tailorable in its rate of surface and bulk biodegradation, crystallinity, structure topography and mechanical properties [82]. In this study we will present a justification of our novel geometrical model to predict topographical features of electrospun melt fibers altered by temperature, collecting distance, applied voltage and nozzle diameter. For each set of controlling parameters, numerical results are discussed in detail and compared to the experimental data. Finally, the results of fiber diameter and scaffolds porosity under random conditions without any experiments can be predicted.

3.2 Modeling procedure

As our objective is to develop a microfiber model to describe the melt electrospinning parameters that influence fiber diameter and scaffold porosity, including nozzle size, counter electrode distance and applied voltage. First we briefly discuss on melt electrospining process and the next section describes relevant geometrical modeling.

3.2.1 Geometrical modeling

In melt electrospinning process after the introduction of the electric field the shape of the jet continuously changes hence droplet is stretched into a Taylor cone and a straight jet as illustrated in Figure 10 then stretched into a helix movement jet. Initially, the extruded polymer melt at the tip of the nozzle is like a truncated spherical droplet which changes its shape after the introduction of the electric field. Though there are geometrical models for electrospinning process such as Taylor cone as a frustum and straight jet as a cylinder are discussed in literature [41, 71, 73, 80, 83]. In our modeling, the jet pulled out from droplet is geometrically defined as a funnel as shown in Figure 10 which consists of a cone whose tip is removed surmounted on a narrow cylinder is discussed. Also, our interest is to develop a geometrical modeling to optimize nozzle diameter through derivation of the relation between the nozzle diameter and fiber diameter.

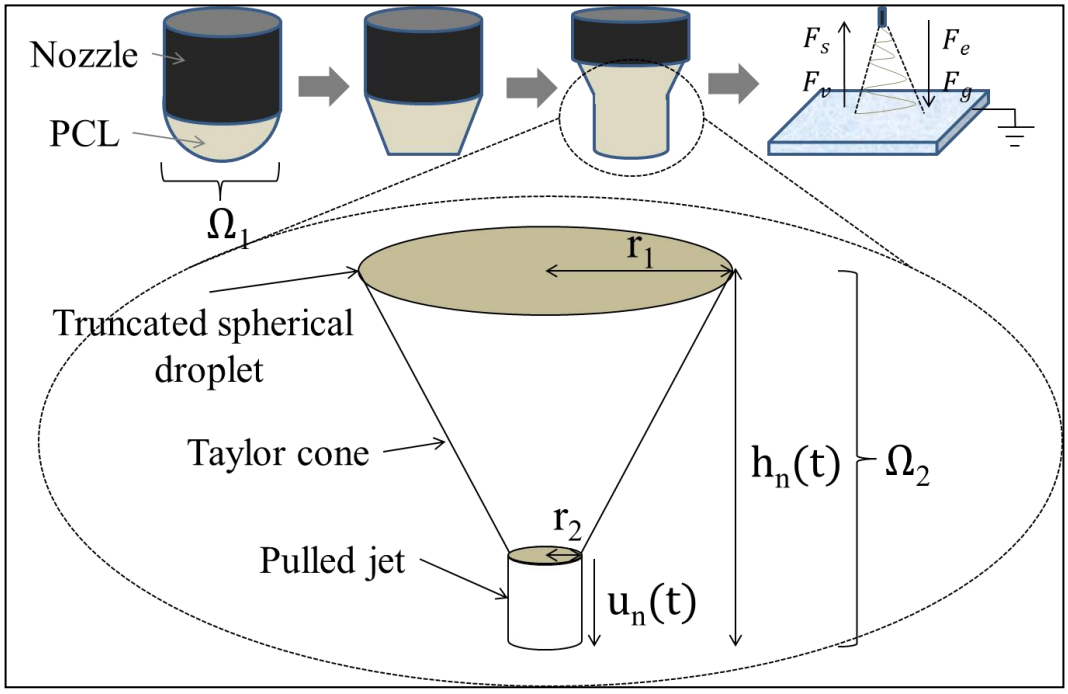

Figure 10. Geometry of different stages of electrospun fiber and the straight jet surmounted by a truncated cone

First, we consider a droplet of melt polymer as a truncated spherical shape at the tip of the nozzle of a radius r_1, height $h_0 = r_1$ having volume as:

$$V_0 = \frac{2\pi {r_1}^3}{3} \tag{8}$$

On exiting the nozzle, the tip droplet becomes exposed to all the forces acting on it and it is pulled it into a Taylor cone with, the top radius r_1 (constant), bottom radius r_2 and height h_1 where both (r_2, h_1) are function of time. The following are the initial conditions assumed in further development of the modeling:

$$t = \begin{cases} t = t_0, & r(t = t_0) \\ t = t_f, & r(t = t_f) \end{cases} \tag{9}$$

where, t_0 is the initial time and t_f is total time of electrospinning. Next, the volume of Taylor cone V_1 is given by:

$$V_1 = \frac{\pi h_1(t)}{3}[r_1^2 + r_1 r_2(t) + r_2^2(t)] \tag{10}$$

Further upon using the flow rate of the polymer melt the volume of the system at any time t, can be calculated [73]. Therefore, the volume of the melt polymer in the truncated cone Ω_1 is:

$$\Omega_1(t) = V_0 + Qt \tag{11}$$

where, Q, t and V_1 are the flow rate, time and volume of truncated cone given in Eq. (8). The whole system (jet or fiber) before it becomes unstable geometrically is assumed as funnel which means a cylinder surmounted by a truncated cone as illustrated in Figure 10.

Therefore, the radius of the top and bottom of the funnel are r_1 and $r_2$respectively as illustrated in Figure 10. Further, the radius of straight jet $r_2$is considered as a good approximation to estimate the fiber diameter. Also, $r_2$is assumed as a constant in the

further process of electrospinning. Now, the volume of cylinder V_2 and volume of polymer melt in cylinder Ω_2 , at time t are:

$$V_2 = \pi[r_2^2 h_2(t)] \tag{12}$$

$$\Omega_2(t) = V_1 + Qt \tag{13}$$

Furthermore, from our geometrical model shown in Figure 10 and upon using Eq. (9), (12) and (13), we have derived the relation between nozzle radius r_1 and straight jet radius r_2, which is same everywhere within the straight jet as:

$$r_2(t) = \frac{-h_1(t)\pi r_1 \pm \sqrt{3\pi}\sqrt{-4(h_1(t)-3h_2(t))Qt - h_1(t)(h_1(t)-4h_2(t))\pi r_1^2}}{2(h_1(t)-3h_2(t)\pi)} \tag{14}$$

In the beginning the height of droplet $h_0 = r_2$, the radius of the nozzle which is constant. After the introduction of electrical force polymer melt move toward collector the height of the jet changes with time. Therefore height of Taylor cone h_1 and straight jet h_2 can be can be calculated as:

$$h_n(t) = h_{n-1} + \int_0^t u_n(t)dt \tag{15}$$

where, $n = 1,2$, and $u(t)$, the electrospinning velocity at any time t is:

$$u_n(t) = u_{n-1} + \int_0^t \frac{\sum F}{m} dt \tag{16}$$

where, $n = 1,2$ represent Taylor cone and straight jet respectively, $\sum F$ is the sum of forces – surface tension F_s, viscoelastic F_v, gravity F_g and electrostatic F_e, and m the mass of polymer melt which are discussed in next sections.

3.2.2 The forces acting on the straight jet

The forces acting on the straight jet are surface tension, viscoelastic, gravity and electrostatic. The surface tension on the droplet and the viscoelasticity within the droplet

will be opposing the formation of an extended jet and will therefore result in a negative force. The surface tension force is given in [73] as:

$$F_s = \frac{-\gamma\left(a_{s_{n+1}}(t) - a_{s_n}\right)}{h_n(t)} \tag{17}$$

where, surface tension γ, which is by definition work per change in surface area is given as:

$$\gamma = \int \frac{2\,F_s r\,h_n(t)}{a_{s_n}} \tag{18}$$

and $a_{s_1}(t) = \pi\big(r_1 + r(t)\big)\sqrt{\big(r_1 - r(t)\big)^2 + (h(t))^2}$, $a_{s_2}(t) = 2\pi r(t)(r(t) + h(t)$ are surface area of Taylor cone and straight jet respectively at $n = 1,2$. The viscoelastic force F_v which opposes the flow of the stream is:

$$F_v = -\sigma(t) \times A \tag{19}$$

where, A is the area of the jet top and the corresponding stress $\sigma(t)$ can be expressed through the relationship:

$$\sigma = Y\varepsilon + \eta_d\dot{\varepsilon} \tag{20}$$

where, Young's modulus Y, dynamic viscosity η_d [84], strain ε and strain rate $\dot{\varepsilon}$ are given by:

$$Y = \frac{\eta_d}{t_r} \tag{21}$$

$$\eta_d = e^{-\frac{E_n}{R\,T}} \tag{22}$$

$$\varepsilon = \frac{\text{Stretched length } (L_s)}{\text{Flow length of the melt polmer } (L_f)} \tag{23}$$

Flow length and stretch length are given by the relation

$$L_f = \frac{4\,t\,Q}{2\pi\left(\frac{1}{3}r + \frac{2}{3}r_1\right)} \tag{24}$$

$$L_s = h + \int_0^t u_n dt - L_f \tag{25}$$

and

$$\dot{\varepsilon} = \frac{d\varepsilon}{dt} \tag{26}$$

where, u is the velocity of fiber and T, t_r E_η, R are constant temperature, relaxation time, activation energy and gas constant are constants given in Table 3. In our model of straight jet polymer volume changes from a truncated cone to a straight jet having both elastic and viscous characteristics in hence some of the energy is returned to the system and some of the energy is converted into heat due to unloading. Further, the forces that act in the same direction of the flow of the jet gravity and electrostatic forces are:

$$F_g(t) = m\rho g = (V_1 + Qt_f)\rho g \tag{27}$$

$$F_e(t) = \frac{e(t)\psi}{z} \tag{28}$$

where, the density ρ of the material(PCL)[69], the jet mass m at time t , and the charge on the jet e(t) [85] are given as :

$$\rho = \frac{0{\cdot}9046\, e^{0.0006392T}}{0.99868+0.0081076T+0.000070243\, T^2} \tag{29}$$

$$m_n = (V_{n-1} + Q\, t_f)\rho \tag{30}$$

$$e(t) = 8\pi\sqrt{r_2^2(t)\, \gamma\varepsilon_o C} \tag{31}$$

where, γ is surface tension given in Eq. (18) and ε_o, C, ψ is, z are permittivity of veccum feasibility factor of material, applied voltage and the collection plate distance from the tip of the jet, respectively given in Table 3.

Table 3. Parameters used for numerical simulations

Parameters	Experimental data	Literature & Standard data
Distance between nozzle and fiber collector, z	5 cm, 10cm	
Flow rate, Q	2mL/h	
Temperature, T	80^0 C	
Ambient temperature, T_a	20^0C	
Activation energy, E_η		10.1 kcal/mol
Gas constant, R		1.9872 k^{-1} cal/ mol
Relaxation time , t_r	0.0001s	
Permittivity of vacuum, ε_o		8.854 187 817 x 10^{-12}($F \cdot m^{-1}$)
Feasibility factor of material, C	1	[21]

Next, as we know from literature, both the voltage supplied and the resultant electric field have an influence in the stretching and the acceleration of the jet hence they will have an influence on the morphology of the fibers obtained. In most cases, a higher voltage will lead to greater stretching of the melt due to the stronger electric field thus the effect of reducing the diameter of the fibers [72, 74]. Therefore, we have derived results for the effect of voltage and distance on electrospun fiber of polymer PCL based on Eq. (28) which are discussed in section of numerical and experimental results.

3.2.3 Scaffold modeling

The topology of scaffold is estimated using fiber diameter (r_2) and fiber velocity (u) calculated from the previous sections. Figure 11A shows loop pattern in melt electrospinning and Figure 11B represents schematic of position trajectory on a flat surface.

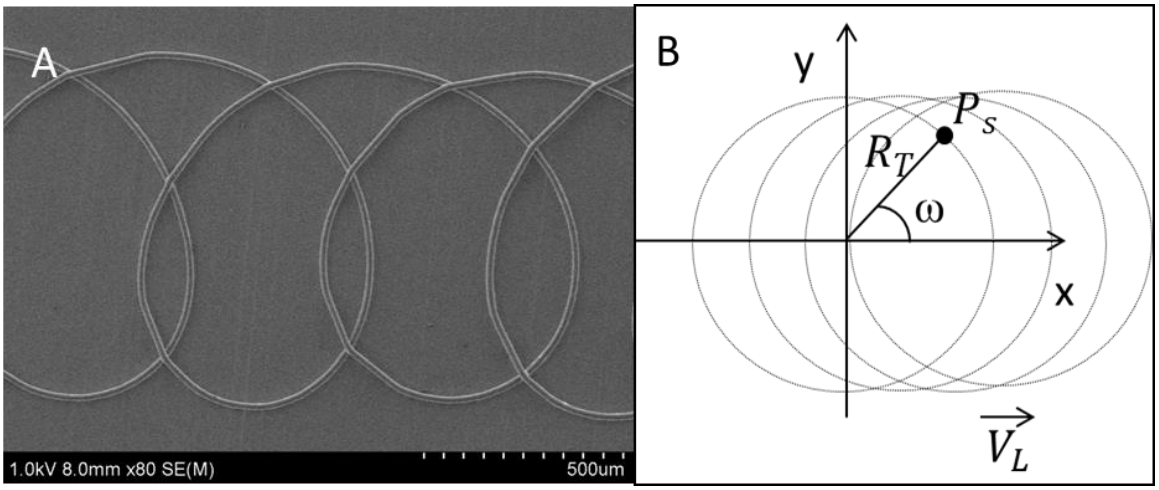

Figure 11. (A) Loop pattern in SEM image, (B) schematic of position trajectory

The position P_s, the center of fiber, in 2D domain is defined by:

$$P_s(x,y) = \int V_A + \int V_L = \begin{bmatrix} r\cos(\omega t) \\ r\sin(\omega t) \end{bmatrix} + \begin{bmatrix} V_L t \\ 0 \end{bmatrix} \tag{32}$$

where, V_A is total angular velocity, V_L is linear velocity, R_T is experimental radius of torus and $\omega = u/R_T$ is angular velocity. If the extension is 3D domain, the position $P_s(x,y,z)$ can be obtained by following relation in zigzag movement:

$$P_s = \begin{bmatrix} x_1 \\ y_1 \\ z_1 \end{bmatrix} + \begin{bmatrix} V_L t \\ 0 \\ 0 \end{bmatrix} = \begin{bmatrix} R_T\cos(\omega t) + V_L t \\ R_T\sin(\omega t) \\ 2r_2(1-\cos\omega t) \end{bmatrix} \quad 0 \le t \le t_1, 0 \le z_1 \le 2\text{mm}$$

$$P_s = \begin{bmatrix} x_1 \\ y_1 \\ z_1 \end{bmatrix} + \begin{bmatrix} 0 \\ V_L t \\ 0 \end{bmatrix} = \begin{bmatrix} R_T\cos(\omega t) \\ R_T\sin(\omega t) + V_L t \\ 2r_2(1-\cos(\omega t)) \end{bmatrix} \quad t_1 \le t \le t_2, 0 \le z_1 \le 2\text{mm}$$

$$P_s = \begin{bmatrix} x_1 \\ y_1 \\ z_1 \end{bmatrix} + \begin{bmatrix} -V_L t \\ 0 \\ 0 \end{bmatrix} = \begin{bmatrix} R_T\cos(\omega t) - V_L t \\ R_T\sin(\omega t) \\ 2r_2(1-\cos(\omega t)) \end{bmatrix} \quad t_2 \le t \le t_3, 0 \le z_1 \le 2\text{mm}$$

$$P_s = \begin{bmatrix} x_1 \\ y_1 \\ z_1 \end{bmatrix} + \begin{bmatrix} 0 \\ V_L t \\ 0 \end{bmatrix} = \begin{bmatrix} R_T\cos(\omega t) \\ R_T\sin(\omega t) + V_L t \\ 2r_2(1-\cos(\omega t)) \end{bmatrix} \quad t_3 \le t \le t_4, 0 \le z_1 \le 2\text{mm} \tag{33}$$

where, t_1, t_2, t_3, and t_4 are arbitrary time to change directions.

The position P_d on a drum surface is defined by:

$$P_d = \begin{bmatrix} x_1 \\ y_1 \sin(\alpha t) \\ z_1 \cos(\alpha t) \end{bmatrix} + \begin{bmatrix} V_L t \\ d_r \cos(\alpha t) \\ d_r \sin(\alpha t) \end{bmatrix} = \begin{bmatrix} R_T \cos(\omega t) + V_L t \\ d_r \cos(\alpha t) + r \sin(\omega t) \sin(\alpha t) \\ d_r \sin(\alpha t) + 2r_2(1 - \cos(\omega t)) \cos(\alpha t) \end{bmatrix} \quad (34)$$

where, α is drum angular velocity, d_r is drum radius.

3.2.4 Porosity

The theoretical porosity was calculated based on estimation of fiber diameter, overlap area, and total volume of PCL microfibers. We have previously reported that we assumed the scaffolds were cuboid shaped, composed of perfect circular cylindrical microfibers called torus [69]. In addition, scaffold porosities on flat and drum surface are calculated in the same way.

The porosity of scaffold is defined by [45]

$$\emptyset_{mesh} = \left(1 - \frac{NV_t}{V_s}\right) \times 100\% \quad (35)$$

where, $\emptyset_{mesh}$, V_t, V_s, N are respectively porosity of mesh, volume of torus, volume of whole scaffold, and number of torus. The torus volume is calculated by

$$V_t = 2\pi^2 R_T r_2^2 \quad (36)$$

where, R_T is distance from the center of the tube to the center of the torus and r_2 is the radius of the fiber. The volume of whole scaffold is determined by

$$V_s = w_1 w_2 H,\ w_1 = V_{tr} t_1,\ w_2 = V_{tr} t_2 \quad (37)$$

where, w_1, w_2, H, V_{tr} are respectively scaffold width, scaffold length, scaffold height, and transitional speed. t_1 and t_2 are arbitrary time. The number of torus and overlap percentage can be calculated by

$$N = \left\{\frac{w_1}{2(R_T + r_2)}\left(1 + O_p\right)\right\}\left\{\frac{w_2}{2(R_T + r_2)}\left(1 + O_p\right)\right\}\left\{\frac{H}{4r_2}\right\},\ O_p = \frac{A_2}{A_1} \times 100(\%) \quad (38)$$

where, O_p is overlap percentage [69].

3.3 Experimental procedure

3.3.1 Fabrication of microfibers

Poly (ε-caprolactone) (PCL) (Mn ~45,000) was purchased from (Sigma Aldrich, USA) with a melting point of 60°C. The detail of our custom-made melt electrospinning setup has been already published [86]. Previously, we reported that for the collection of randomly aligned scaffolds, a wood plate covered with aluminum foil has been used as the counter electrode [69]. Briefly, in order to fabricate microfibers, we have applied 10, 15 and 20kV to the molten PCL at 80˚C using a high voltage power supply (Gamma High Voltage Research Inc., USA) with the working distance between the nozzle and aluminum foil collector ranging from 5 and 10cm. The PCL granules were dispensed into melting chamber with the nozzle attached and then heated to the desired temperature. The rheological properties of our PCL have been reported as well [69, 86]. To our knowledge, parameters related to fiber diameter and morphology of scaffold when melt electrospinning include nozzle diameter, processing temperature, collection distance, applied voltage, flow rate of syringe pump and linear velocity of x and y axis in CNC machine [16, 18-21, 57]. As we previously reported, a syringe pump was used to inject the flow of PCL melt at a flow rate of 2 mL per hour [69]. To investigate the influence of electrical force, nozzle diameter and linear velocity were respectively fixed at 200 μm and 8.5 mm/sec. Based on our parameter analysis, the melt temperature was set at 80°C with an applied voltage of 20 kV and a collection distance of 5 cm. These conditions ensured proper fiber formation during the electrospinning process. Figure 12 shows two

types of scaffold morphology on flat and drum surface. (A, B) and (C, D) respectively presents biaxial loop mesh on flat surface and uniaxial loop mesh on drum surface.

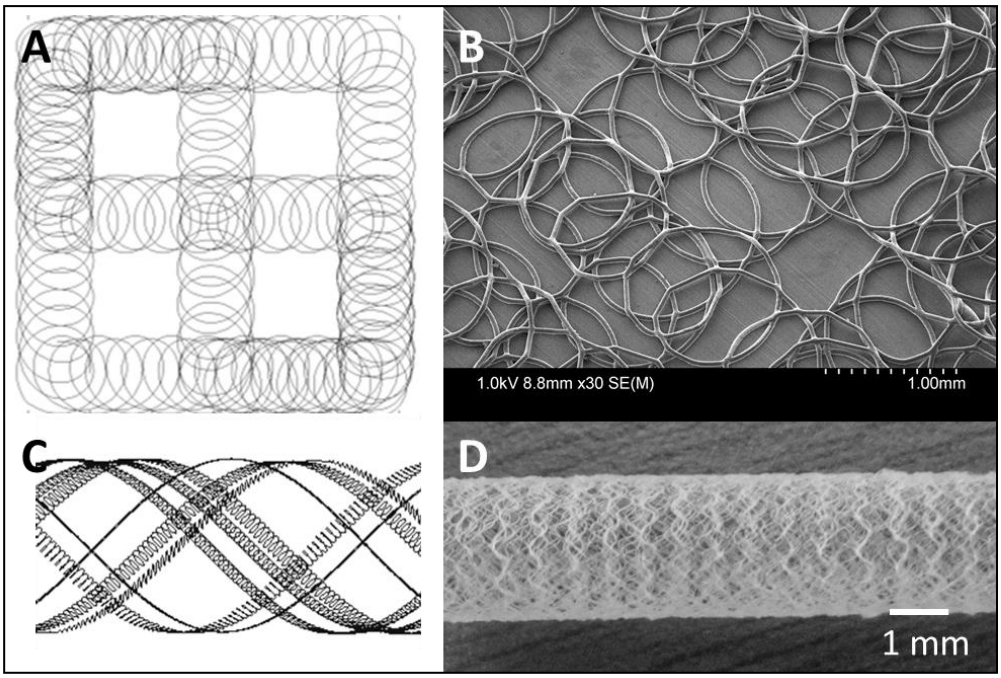

Figure 12. Morphology of Scaffolds on (A, B) flat surface and (C, D) drum surface

3.3.2 Analysis of microfiber topography

Prior to scanning electron microscopy (SEM) imaging, all PCL microfibers were coated using Cressington 208 carbon coater two times for 6 seconds at 10-4 mbar and consequently samples were transferred to loading stubs for Hitachi S-4800 field emission scanning electron microscope. High magnification images were captured at 1 kV with an 8 mm working distance. Using Quartz-PCI Image Management Systems® fibers were characterized in terms of fiber diameters, torus diameter and overlap measurements.

3.3.3 Image processing for porosity measurement

Due to an inability to collect data on the scaffold porosity directly, we used two software programs which are Adobe Photoshop CS5 and Matlab R2013a to determine

porosity from SEM image. The Photoshop was used to clarify the boundaries between background and microfibers and change white microfibers as shown in Figure 13. Then the Matlab was used to count white pixels on microfibers and measure porosity of various scaffolds.

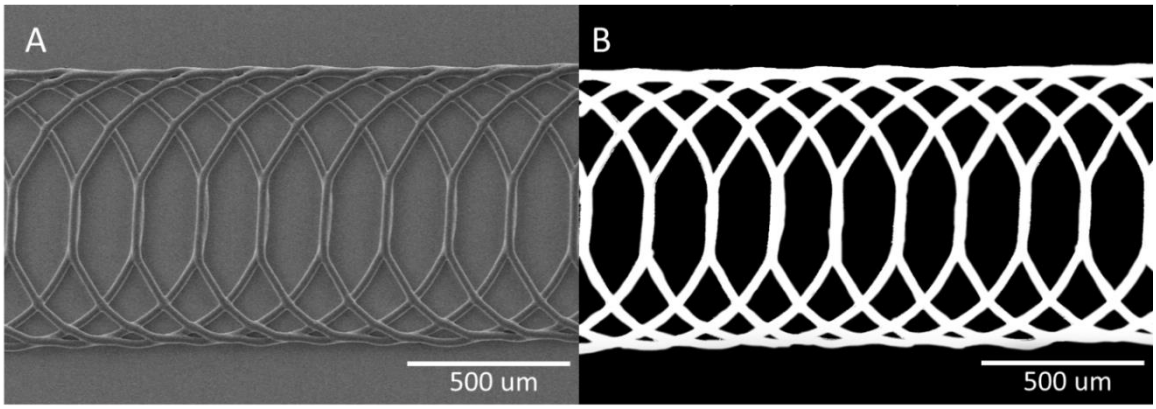

Figure 13. (A) Original SEM image of microfibers using 150μm nozzle (Transitional speed: 8.5mm/s), (B) Image processing from SEM image

3.3.4 Spinning speed analysis

Speed of spinning fibers played a key role in controlling the morphology of scaffolds but directly measuring speed is one of challenging parts so two indirect methods are used:

1. Angular velocity analogy is that measuring angular velocity (ω) and distance from center of tube to the center of torus (R_T) from SEM images and then spinning velocity (V_{s1}) is calculated by .

$$V_{s1} = \omega R_T \tag{39}$$

2. Mass production analogy is that measuring accumulated weight (m_{t_s}) of fibers during a certain time (t_s) and then spinning velocity (V_{s2}) is defined by [69].

$$V_{s2} = \frac{m_{t_s}}{\pi r_2 D t_s} \tag{40}$$

where, D is density of PCL polymer.

3.3.5 Statistical analysis

Quantitative data are presented as mean ± standard deviation (SD). The processing parameter study were screened by one-way analysis of variance (ANOVA) with the assumption of normally distributed data using Microsoft Office Excel 2010, USA; significance was defined as $p<0.05$.

3.4 Numerical and experimental results

3.4.1 Effects of nozzle diameter

The effect of nozzle diameter on the fiber diameter is studied in simulation and experiment. All distance between nozzle and counter electrode, flow rate, voltage, and temperature are respectively fixed at 5cm, 2mL/h, 20kV and 80°C in order to restrict parameters related to fiber diameter. Nozzle diameter decides initial diameter of fibers by direct deposition and diameter of fibers is shrunk by electrical force and gravity force after spinning. Figure 14A and B present comparison of numerical and experimental fiber diameter and electrospinning velocity in various nozzle diameters. Numerically, when nozzle diameter changes, the Taylor cone V1 will be changed accordingly. Therefore, the increase in nozzle diameter would eventually affect the gravity force applied to the Taylor cone to stretch out fibers according to the equations (9) and (27). That eventually would lead to Experimentally the fiber diameter increased from 12 ± 1μm to 220 ± 9μm as the nozzle diameter increased from 150μm to 1,700μm. Similarly, in simulation the fiber diameter increased from 18μm to 212 μm as the nozzle diameter increased from 150 μm to 1,700 μm. However, the velocity is decrease from 236.5 mm/s to 1.84 mm/s in simulation. Experimental velocity-1 and velocity-2 in Figure 14B

respectively indicates angular velocity analogy and mass production analogy. Velocity-1 and Velocity-2 respectively are varied from 206.3 ± 14.4 mm/s to 4.2 ± 0.3 and from 210.4 ± 14.7 mm/s to 7.2 ± 0.5mm/s when nozzle diameter increased from 150μm to 1,700μm.

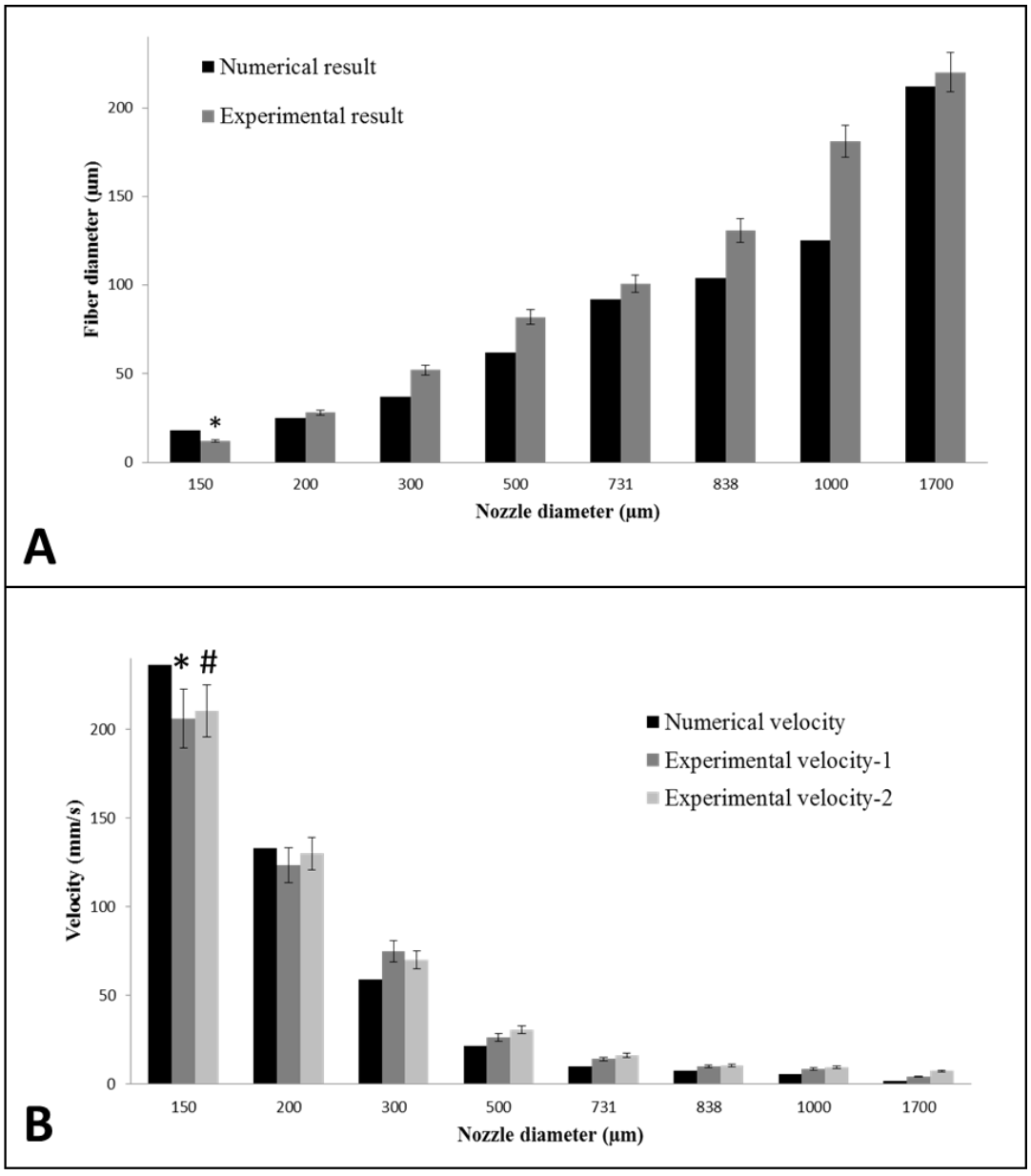

Figure 14. Effects of nozzle diameter in simulation and experiment at 20kV and 80°C, (A) fiber diameter depended on nozzle diameter, (B) velocity depended on nozzle diameter. (n=3), * and # indicates $p<0.05$ versus all other nozzles

3.4.2 Effects of distance and voltage on fiber diameter

Figure 15 shows the effects of collecting distance and voltage power on the resulting fiber diameter at 200 μm nozzle, 80°C temperature, and 2mL/h flow rate. According to Coulomb's law, magnitude of the electrical force was directly proportional to applied voltage and inversely proportional to the distance. Theoretically, the electrostatic force in melt electrospinning is a function of the net charge of fibers according to the equation (28). Since, e(t) depends on the r2, any variation in the net charge coming from the electrostatic force would be affecting the fiber diameter as well. In experimental results, fiber diameter showed 49 ± 5 μm at 10kV and 28 ± 4 μm at 5cm and 20kV. Similarly, fiber diameter represented 44.44 μm at 10kV and 28 μm at 5cm and 20kV in numerical results. When distance was increased from 5cm to 10cm at 20kV, fiber diameter demonstrated 28 ± 5 μm at 5cm and 37 ± 7 μm at 10cm in experimental results. In numerical results, the fiber diameter showed 28 μm at 5cm to 44.44 μm at 10cm. Fiber diameters increased in size by approximately 1.4 times when the collecting distance was doubled at 20kV. Moreover, when applied voltage was doubled, the fiber diameters decreased to 1.6 times from their original size at 5cm.

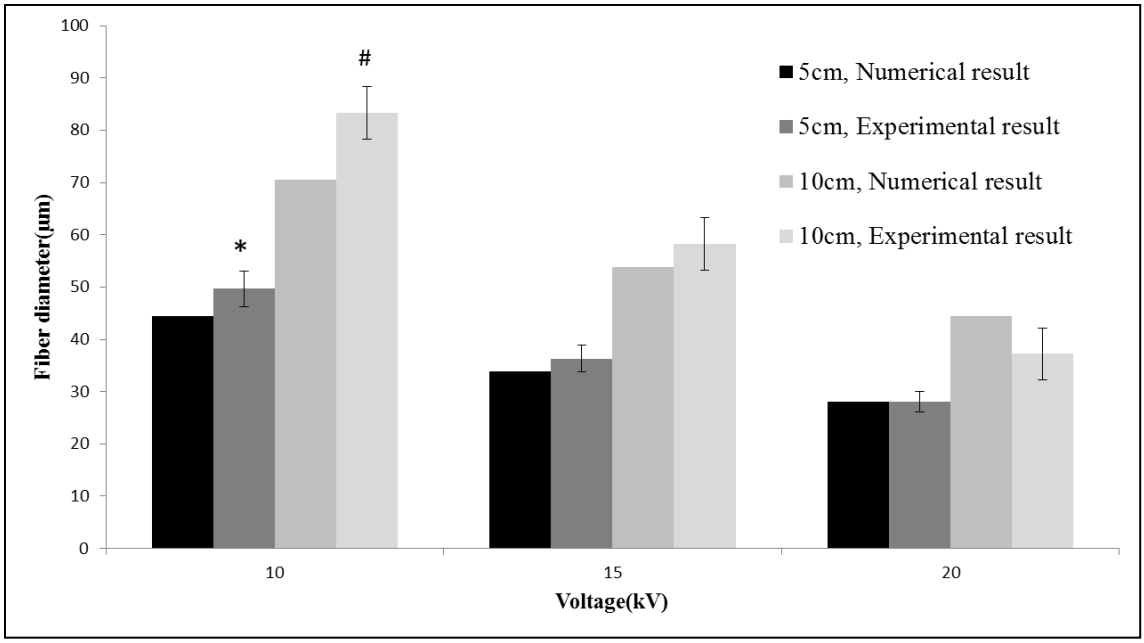

Figure 15. Effects of collection distance and applied voltage on the resulting fiber diameter using 200 μm nozzle at 80˚C (n=3). * indicates p<0.05 versus all other voltage at 5cm distance. # indicates p<0.05 versus all other voltage at 10cm distance

3.4.3 Topology controlled by transitional speed

The fiber diameter (r_2) and electrospinning velocity (u) come from geometrical modeling becomes input parameters for scaffold modeling. The transitional speed (V_{tr}) in scaffold modeling is a significant parameter to determine topology of controlled scaffolds. Figure 16 shows (11mm x 11mm) numerical and experimental topology depended on various transitional speed at 200μm nozzle, 20kV applied voltage, 5cm distance, 80˚C temperature. (A, B), (C, D), and (E, F) in Figure 16 respectively represent 17mm/s, 8.5mm/s, and 7mm/s transitional speed. If V_{tr} is decreased, intervals between tori become more dense.

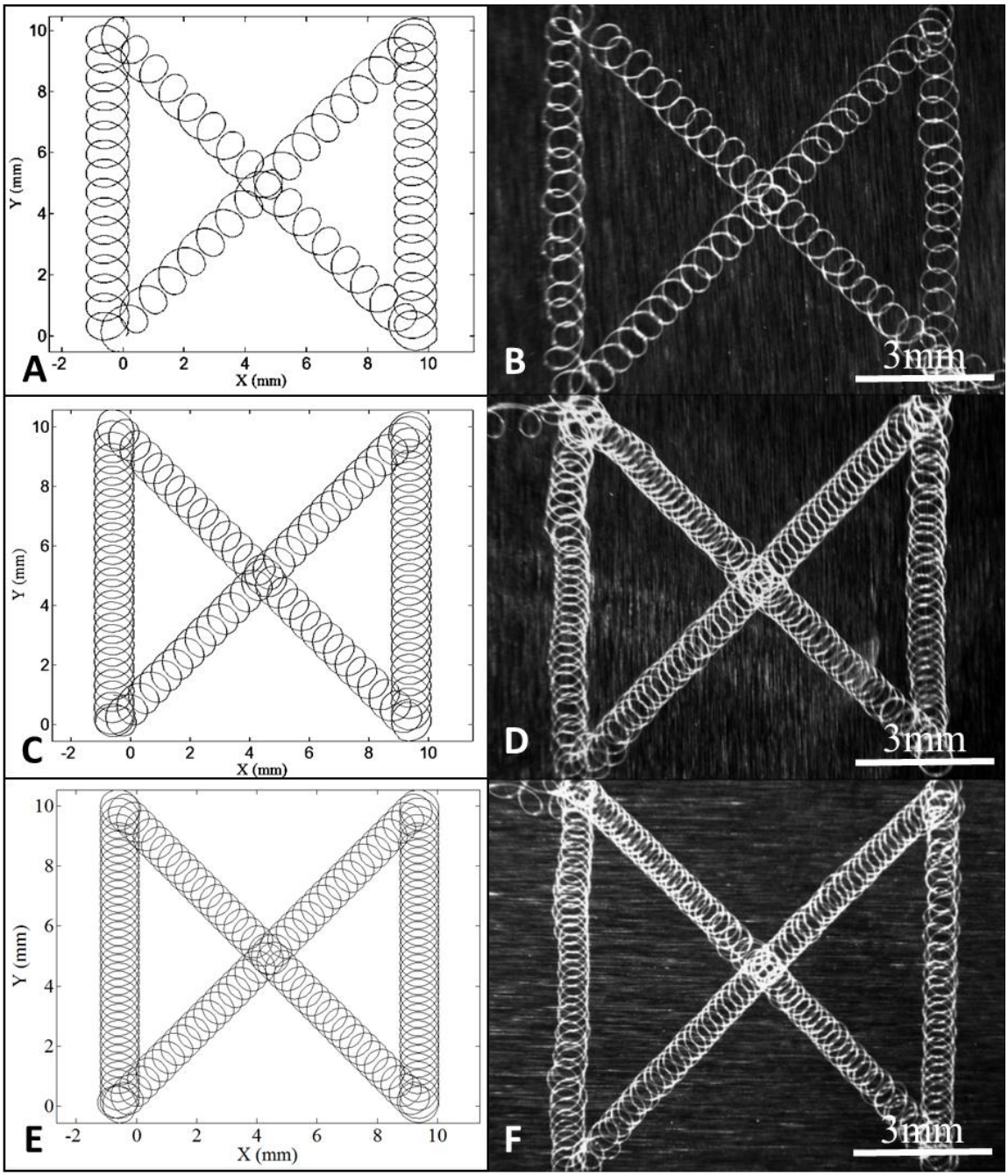

Figure 16. Topology affected by transitional speed at 200μm nozzle, 20kV applied voltage, 5cm distance, 80˚C temperature. A,C,E: Matlab image, B,D,F: microscope images. A-B: 17mm/s, C-D: 8.5mm/s, E-F: 7mm/s

3.4.4 Porosity of controlled scaffolds

The porosity of scaffolds can be controlled by fiber diameter and transitional speed. Figure 17 shows results of numerical and experimental porosity depended on various nozzles at 20kV applied voltage, 5cm distance, 80˚C temperature, and 8.5mm/s transitional speed. In numerical result, the porosity is varied from 95% to 85% when nozzle diameter is changed from 150 μm to 1,700 μm. Similarly in experimental result, the porosity is varied from 88% to 82% when nozzle diameter is changed from 150 μm to 1,700 μm. The significant factors to determine porosity in detail were torus volume (V_t) and number of torus (N). The increment of number of torus and the decrement of torus volume were very similar from 500 μm to 1,700 μm so Figure 17 shows flat in the section. Conversely, the decrease in torus volume occurred more rapidly than the increase in the number of torus from 150 μm to 500 μm so the porosity becomes increased.

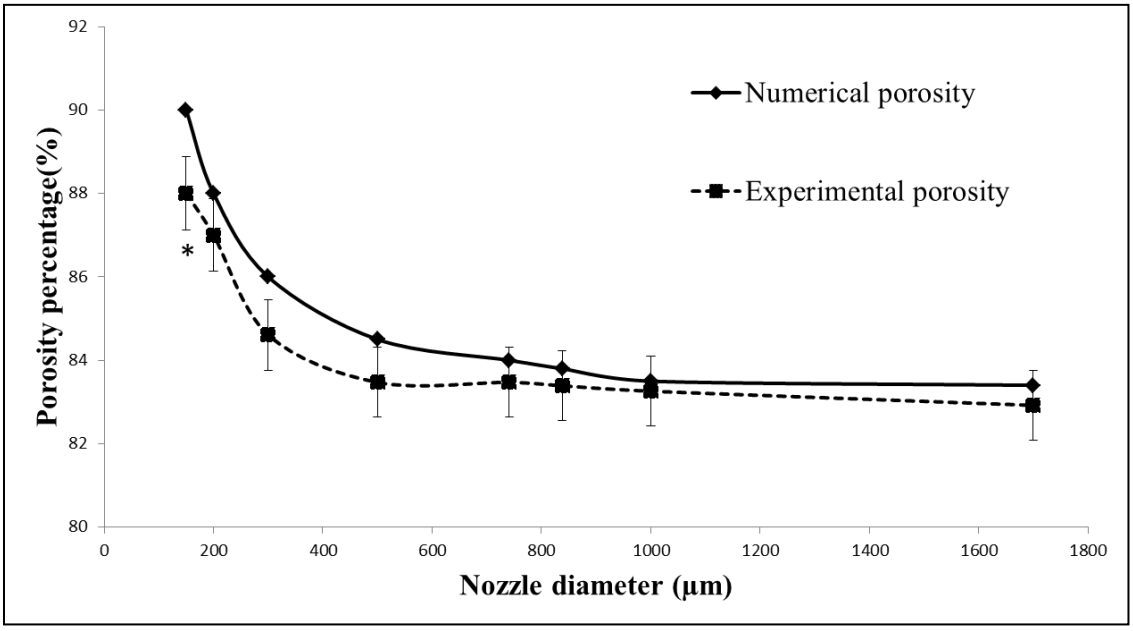

Figure 17. Numerical and experimental porosity in various nozzle diameters at 20kV. (n=3)
*** indicates p<0.05 versus all other nozzles**

Figure 18 shows the porosity controlled by transitional speed at 200μm nozzle, 20kV applied voltage, 5cm distance, and 80˚C temperature. The transitional direction is left to right on the figure and the speed is calculated by Eq. (35). The speeds of 7.2, 4.4, and 2.1mm/s represent respectively 80, 60 and 40% porosity. Figure 19 shows the result of porosity controlled by transitional speed. When aiming for 80, 60, and 40% porosity, the experimental porosity is respectively 74.8 ± 3.7, 53.5 ± 2.7, and 35.7 ± 1.8%.

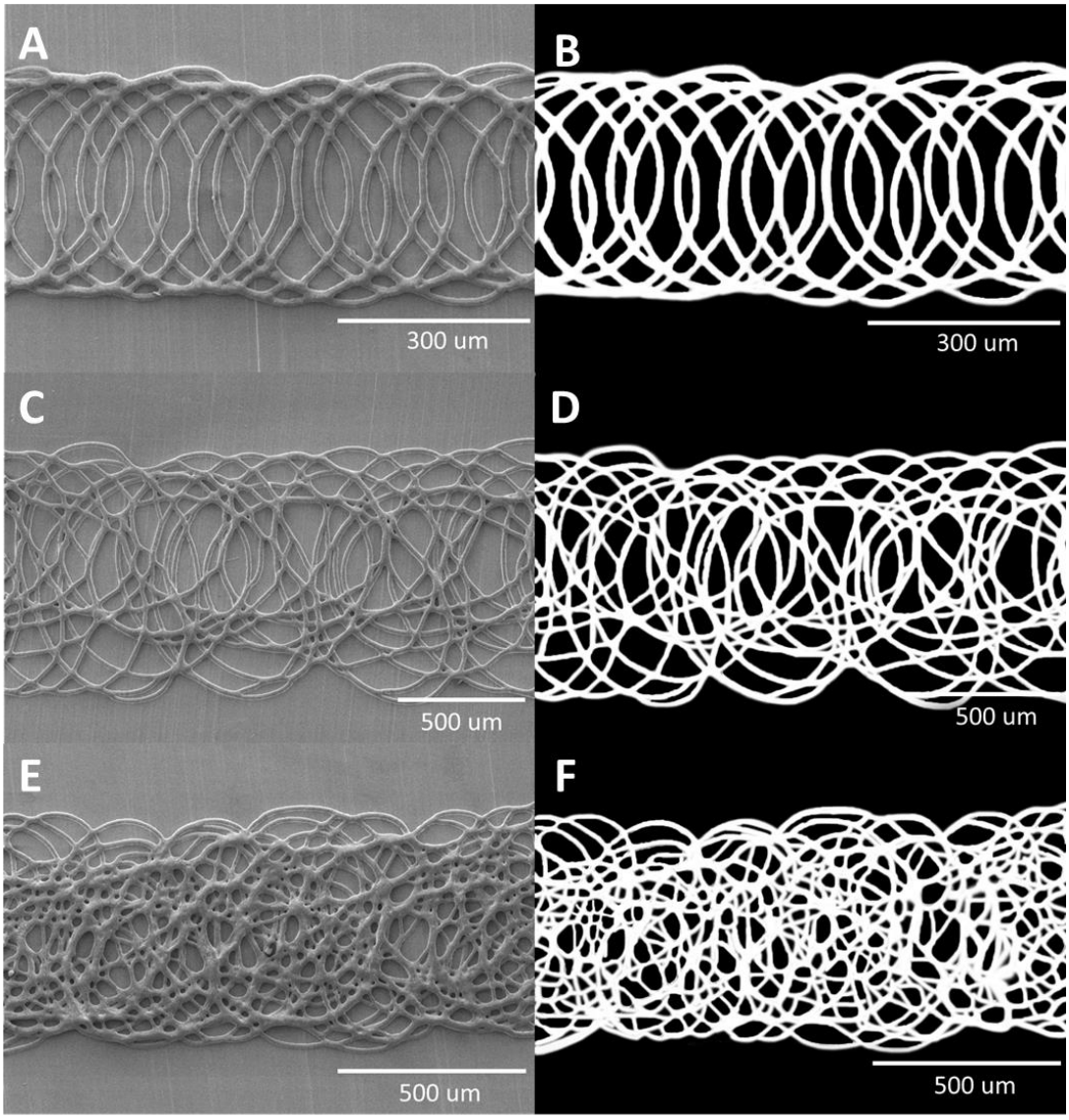

Figure 18. The porosity controlled by transitional speed at 20kV: (A-B) 80%-7.2mm/s, (C-D) 60%-4.4mm/s, and (E-F) 40%-2.1mm/s

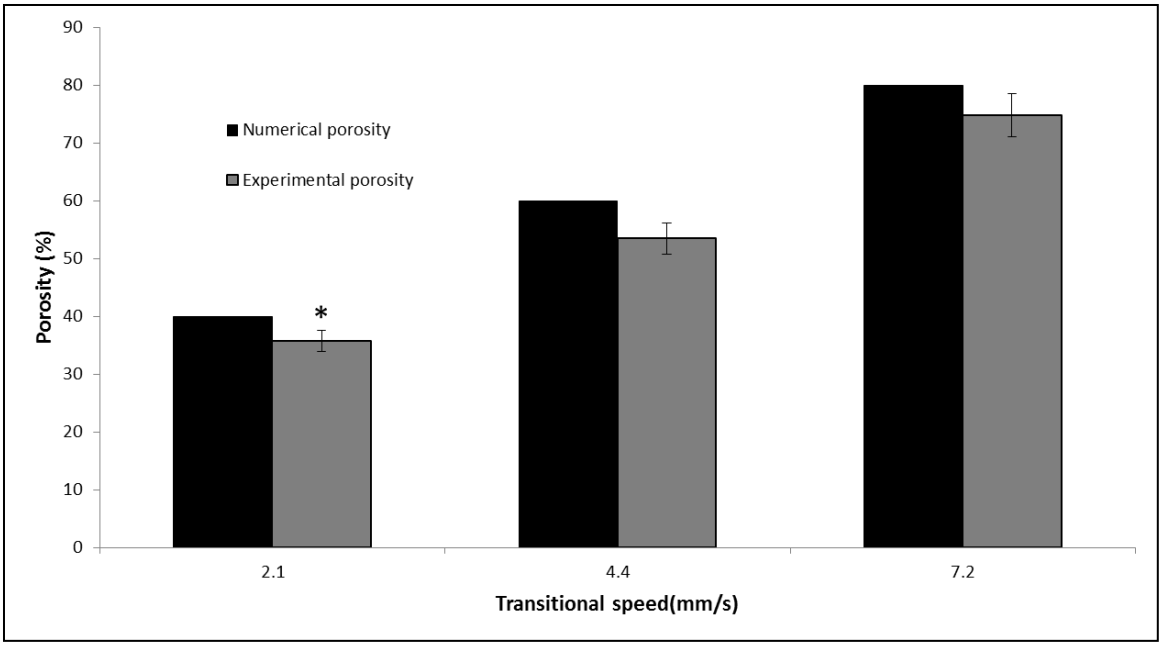

Figure 19. Result of porosity controlled by transitional speed at 200μm nozzle. (n=3), * indicates p<0.05 versus all other transitional speed

3.4.5 Predictions

In section 3.4.1 through 3.4.4, we compared numerical and experimental results and confirmed our modeling to be reliable. As the ultimate goal, the predictions of fiber diameter and porosity under ambiguous parameters are shown in Figure 20. The fiber diameter depended on diameter of nozzle can be predicted that move along the linear curve as shown in Figure 20A, with conditions (20kV applied voltage, 5cm distance, and 80˚C temperature). We can anticipate that applied voltage and distance are inverse relationship and influences on fiber diameter inversely as well as shown in Figure 20B and C, with conditions (200μm nozzle, (20kV applied voltage or 5cm distance), and 80˚C temperature). Finally, porosity of scaffold can be predicted as shown in Figure 20D, with conditions (200μm nozzle, 20kV applied voltage, 5cm distance, and 80˚C temperature).

The porosity is increased when transitional speed is increased but the porosity does not increase well after 10mm/s transitional speed.

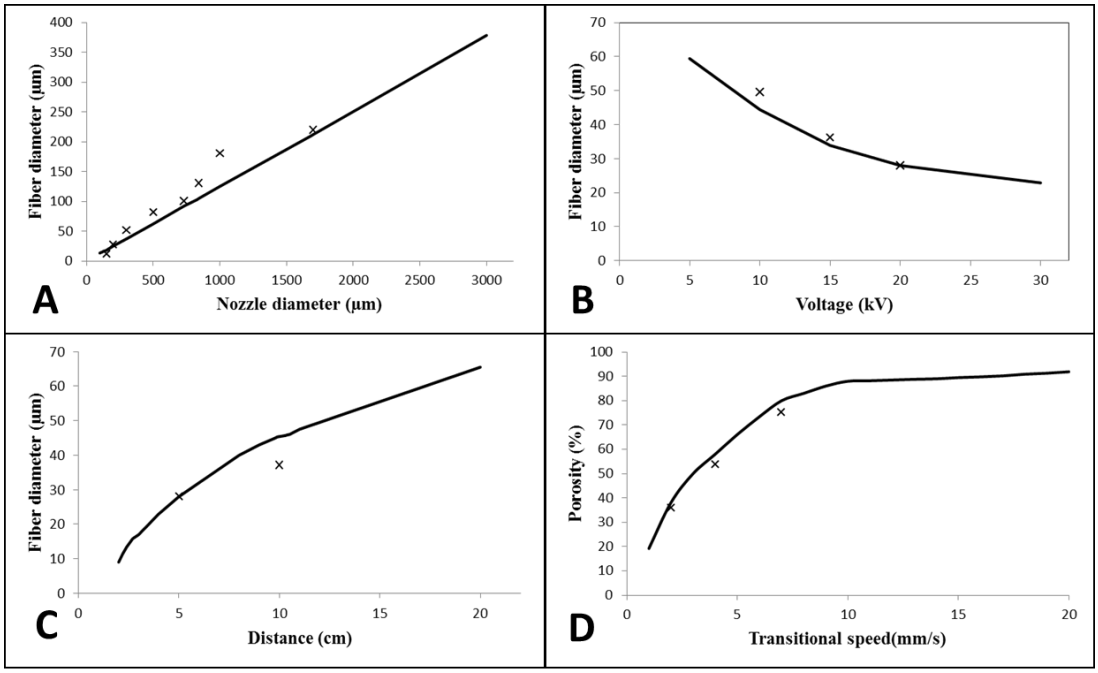

Figure 20. Predictions of fiber diameter and porosity under various conditions. (Marker X indicates experimental data)

3.5 Discussion

Fabrication of electrospun fibers can be accomplished either using solution or melt electrospinning. Even though there are numerous studies on the fabrication of fibers through the use of solution electrospinning, few studies focus on controlling topographical properties of melt electrospun fibers including the uniform distribution of fiber's diameter and also the architecture of scaffolds. Hohman et al. have worked on the modeling of electrospun polymeric fibers [69, 87, 88]. They have reported that the electrospinning jet is actually pulled along by surface stresses, electrical and elastic forces. Since in their modeling there has been no use of used conservation of energy or momentum, here we have worked on calculation all forces in the process. In our work a

mathematical modeling has been developed to obtain fine fibers through various nozzle diameter through the derivation of the relation between the nozzle diameter and fiber diameter. It has been observed that there was reduction in fiber diameter with small diameter nozzle as illustrated in Figure 14A. Additionally, it can be seen that due to the effect of the velocity as shown in Figure 14(B), the velocity decreased as the nozzle diameter was increased. Moreover, both the applied voltage supplied and the resultant electric field had significant influence on the topography of the fibers obtained. Furthermore, the influenced of the applied voltage and counter electrode distance on electrospun fiber of polymer PCL have been investigated numerically, experimentally and presented graphically in Figure 15. It can be clearly seen that fiber diameter decreased when the applied voltage has been increased.

Topography of scaffolds was also controlled by transitional speed at a fixed nozzle diameter. We took the data of the fiber diameter and electrospinning velocity from the aforementioned mathematical modeling. It can be seen from Figure 16, that the simulation and experiment conditions were kept to be consistent but the number of circles has been changed since CNC machine should follow trapezoidal velocity trajectory. The transitional speed was recognized as a prominent in controlling scaffold topography.

The porosity of scaffolds was highly influenced by nozzle diameter and transitional speed as well. Similar to our numerical data achieved from the mathematical modeling, the porosity of scaffolds have shown the same trend using experimental data controlled by fiber diameter and transitional speed. It can be seen clearly that the results of numerical and experimental porosity depended on various nozzles. For instance, numerical data have shown that when nozzle diameter was changed from 150 μm to

1,700 μm, consequently, the porosity was varied from 95% to 85%. Moreover, our work has shown that torus volume and number of torus are one of the most prominent factors to control and predict the porosity of melt electrospun fibers. Through the use of melt electrospinning, we could obtain fibers with the average diameter of 12 ± 1μm at 80°C when using the 150 μm nozzle. We have been able to predict and control this fine fiber size distribution governed by different nozzles though the use of geometrical, mathematical modeling and image analysis as well. Fibers were fabricated with diameter in the range of 12 ± 1 μm to 220 ± 9 μm at 80°C. Moreover, the scaffolds with a specific porosity can be fabricated by transitional speed at fixed nozzle diameter. The transitional speed followed by trapezoidal velocity trajectory in experiments has influenced to porosity control as shown in Figure 17, 18 and 19. When the porosity aims at 40%, 60%, and 80% porosity in Figure 19, the fabricated scaffold shows approximately 5% differences between numerical and experimental porosity. Thus, this excellent degree of predictability and controllability through the modeling approach would lead us to design and engineer melt electrospun fibers for different kind of tissue engineering application based on the desired topography.

The present model could capture melt electrospun PCL fiber topography and could present some topographical information (fiber diameter, topology and porosity). The model employed key parameters of melt electrospinning including nozzle diameter, counter electrode distance, applied voltage and transitional speed that have particular influences on scaffolds topography. As shown in Figure 20, the main goal of this research was to illustrate the feasibility of predicting fibers topography through the use of mathematical modeling and image analyses

3.6 Conclusion

The aim of this research was to develop a reliable mathematical modeling to predict the effect of nozzle size, counter electrode distance and applied voltage on fiber diameter and consequently the topography of scaffolds. PCL microfiber scaffolds were fabricated using melt electrospinning technique with an excellent degree of reproducibility in terms of topographical properties. The effect of nozzle diameter on the fiber diameter was evaluated and the simulation results were compared with experimental data. For instance, according to our experimental data, the fiber diameter was increased from 12 ± 1μm to 220 ± 9μm as the nozzle diameter was increased from 150μm to 1,700μm. Interestingly, the simulation results also showed that fiber diameter was increased from 18μm to 212 μm as the nozzle diameter was increased from 150 μm to 1,700 μm. Moreover, fiber diameter was increased in size by approximately 1.4 times when the counter electrode distance was doubled at 20kV. Additionally, when the applied voltage was doubled, the fiber diameters decreased to 1.6 times from their original size at 5cm. In terms of porosity characterization of scaffolds, we observed that porosity was varied from 95% to 85% when nozzle diameter was changed from 150 μm to 1,700 μm. Similar to the numerical data, experimental results showed that porosity was varied from 88% to 82% while nozzle diameter was changed from 150 μm to 1,700 μm. Moreover, the porosity of scaffold respectively showed 35.7 ± 2.5%, 53.5 ± 4.7%, and 74.8 ± 5.1% using 200μm nozzle at 20kV and 5cm when the porosity aimed at 40%, 60%, and 80% porosity calculated by mathematical modeling. Overall, the ability of predicting topographical features of microfibrous scaffolds fabricated by melt electrospinning, would hold a great promise in fabrication of scaffolds specifically for tissue engineering applications.

Chapter 4. Mathematical model for predicting topographical properties of poly (ε-caprolactone) melt electrospun scaffolds in various temperature and linear transitional speed

4.1 Introduction

Electrospinning has gained increasing popularity in recent years due to a surge in research investigating micro and nanoscale fabrication technologies [43, 45, 89-92]. Electrospinning is a manufacturing technique that can produce both nano- and microfiber structures. These techniques can involve both solution and melt electrospinning. Solution electrospinning produces fibers on the nanoscale due to a whipping instability when fibers are stretched out from the spinning solution. The process of melt electrospinning involves melting the polymer of choice with the being extruded into fibers. Electrospun scaffolds can be fabricated with similar properties to the extracellular matrix and can thereby support cells adhesion, making it attractive for tissue engineering applications [43, 89, 91, 93-97].. However, control over scaffold topography and porosity is limited because of randomness of the whipping instability. Melt electrospinning gives precise control over scaffold topography and porosity, but the fibers are on the micro scale [16, 21, 44, 90, 95, 98-100] . This is because the whipping instability stage is absent due to the lower conductivity and higher viscosity of the polymer melt.

Using the melt electrospining, a variety of electrospun scaffolds with varied topographies can be produced with a high degree of controllability and reproducibility [45, 90, 95, 96, 101, 102]. Electrospun microfibers present an excellent ability of controlling the topography of scaffolds for several tissue engineering applications in which the effect of physical cues would play a key role in studying cell-scaffold

interactions [93, 95]. The fabrication of such scaffolds requires an excellent degree of topographical controllability. Melt electrospining has been used as a powerful technique to achieve the controllability and also the reproducibility of topographical properties including fiber diameter, scaffold architecture, porosity and eventually mechanical properties such as elastic modulus [96, 97, 99, 103-107].

Melt electrospinning can provide control over the directionality of the forming fiber, leading to its use in creating specific topographies. Melt electrospinning is biocompatible as there is no toxic solvents use, unlike solution electrospinning [45, 91, 93, 94, 96]. Melt electrospinning can control the fiber diameter, which can be altered by adjusting parameters such as computer numerical control (CNC) feed speed, extrusion die nozzle diameter, melt temperature, flow rate, and electric field strength [21, 80, 95, 98, 101, 103-105, 107, 108]. Also, melt electrospinning allows for higher viscous forces than solution electrospinning, which means that the viscous forces can balance with electric field forces[44]. As a result, the fibers can be drawn out to be thicker than in solution electrospinning. Therefore, melt electrospinning is a sound method for the creation of specific topographies using microfibers [16, 95].

To achieve a scaffold that provides specific mechanical and topographical properties, a novel mathematical model had to be produced in order to predict the effect of key operational parameters such as nozzle size, temperature, collecting distance and applied voltage on controlling the fiber size and porosity [21, 80, 81, 108]. Although melt electrospining has shown its promising potential in tissue engineering applications, controlling scaffold topography remains challenging [16, 95, 103, 104]. Experimentally, many research papers have shown the effects of the fiber diameter, nozzle size and

temperature on controlling topographical properties such as fiber diameter and porosity, and there are few mathematical models to promote the understanding of these effects[21, 80, 81, 92, 95, 99, 106-109]. Following our previous work on mathematical modelling of melt electrospining [95, 108], we believe that the understanding of the effects of these parameters on topography is possible and the results would be very helpful for engineers in the field to create microfibers with different morphologies by varying the parameters. In our previous work, this effort was undertaken in order to fulfill this need by developing a mathematical model to predict the effect of such parameters on controlling the scaffold topographical properties [108].

In this study we will present a justification of our novel geometrical model to predict topographical features of electrospun melt fibers altered by nozzle diameter, applied voltage, collecting distance, gravitation force, and various heating temperatures on radius of helix and microfiber topology. Moreover the effect of various linear transition speeds on the microfiber topology will be investigated as well. For each set of controlling parameters, numerical results are discussed in detail and compared to the experimental data.

4.2 Modeling procedure

In the previous paper [108], we modeled the melt electrospinning process by incorporating parameters such as nozzle diameter, distance, applied voltage, and linear transitional speed. However, the radius of helix and effect of temperature on topography are respectively acquired from experimental data. Moreover, tension force and linear transitional force influenced on the electrospun microfiber’s topology were not considered in the previous study. In addition, overlapped force model is added to

demonstrate pulling force each other molten condition's fibers in neighbouring distance. To further understand the effect of operational parameters on the properties of microfiber scaffolds, helix movement and three dimensional scaffold modeling are added in our previous models in this study.

4.2.1 Geometrical modeling

At the beginning, the extruded polymer melt at the tip of the nozzle is like a truncated spherical droplet which changes its shape after the formation of the electric field. The geometrical models for melt electrospinning process such as Taylor cone and straight jet were established in [108]. Furthermore, the microfiber extruded from droplet was geometrically defined as a funnel as shown in Figure 10.

The relation between nozzle radius r_1 and straight jet radius r_2 are calculated by [108]:

$$r_2(t) = \frac{-h_1(t)\pi r_1 \pm \sqrt{3\pi}\sqrt{-4(h_1(t)-3h_2(t))Qt - h_1(t)(h_1(t)-4h_2(t))\pi r_1^2}}{2(h_1(t)-3h_2(t)\pi)} \quad (41)$$

where, Q is flow rate. In the beginning the height of droplet $h_0 = r_1$, the radius of the nozzle which is constant. After the introduction of electrical force polymer melt move toward counter electrode the height of the jet changes with time. Therefore height of Taylor cone h_1 and straight jet h_2 can be can be defined as [108]:

$$h_n(t) = h_{n-1} + \int_0^t u_n(t)dt \quad (42)$$

where, $n = 1,2$, and $u(t)$, the electrospinning velocity at any time t is calculated by [108]:

$$u_n(t) = u_{n-1} + \int_0^t \frac{\sum F}{m} dt \quad (43)$$

where, $n = 1,2$ represent Taylor cone and straight jet respectively, $\sum F$ is the sum of forces; surface tension F_s, viscoelastic F_v, gravity F_g, microfiber tension F_T and electrostatic F_e, and m the mass of polymer melt which are discussed in next sections.

4.2.2 The forces acting on the straight jet

The forces associated with the straight jet are surface tension (F_s), viscoelastic (F_v), gravity (F_g), and electrostatic (F_e). The surface tension force (F_s) is given in [108] as:

$$F_s = \frac{-\gamma\left(a_{s_{n+1}}(t) - a_{s_n}\right)}{h_n(t)} \tag{44}$$

where, surface tension γ, which is by definition work per change in surface area is given as $\gamma = \int \frac{2\,F_s r\,h_n(t)}{a_{s_n}}$ and $a_{s_1}(t) = \pi\left(r_1 + r(t)\right)\sqrt{\left(r_1 - r(t)\right)^2 + (h(t))^2}$, $a_{s_2}(t) = 2\pi r(t)(r(t) + h(t))$ are surface area of Taylor cone and straight jet respectively at $n = 1,2$.

The viscoelastic force F_v is calculated by:

$$F_v = -\sigma(t) \times A \tag{45}$$

where, A is the area of the jet top and the corresponding stress $\sigma(t)$ can be demonstrated through the relationship, $\sigma = Y\varepsilon + \eta_d\dot{\varepsilon}$, where Young's modulus Y, dynamic viscosity $\eta_d = e^{-\frac{E_n}{RT}}$ (E_n:activation energy, R: gas constants), strain ε and strain rate $\dot{\varepsilon}$ [108].

The gravity force and electrical force that act in the same direction of the flow the jet are calculated by:

$$F_g(t) = mDg \tag{46}$$

$$F_e(t) = \frac{e(t)\psi}{z} \tag{47}$$

where, the density D of the material(PCL)[95], the jet mass m at time t , and the charge on the jet $e(t)$ [85] are given as :

$$D = \frac{0{\cdot}9049\, e^{0.0006392T}}{0.99868+0.0081076T+0.000070243T^2} \qquad 80\,^{\circ}C \leq T \leq 150\,^{\circ}C \quad (48)$$

$$e(t) = 8\pi\sqrt{r_2^2(t)\,\gamma\varepsilon_o C} \quad (49)$$

where, ε_o, C, ψ , z are respectively permittivity of vacuum, feasibility factor of material, applied voltage and the counter electrode distance from the tip of nozzle [108].

Energy Equation is defined by Eq. (50)

$$\frac{dT}{dz} = -\frac{2\pi r_2 h_t(T-T_a)}{QC_p} \quad (50)$$

where, C_p is specific heat for polymer which is given in Table 4, h_t heat transfer coefficient, T and T_a the polymer fiber temperature and ambient temperature (˚C).

Further, we have derived the expression for the correlation of temperature and fiber diameter using Eq. (51) as [85]:

$$h_t = \frac{k}{2r_2}\left[0.42\left(\frac{2r_2u}{v}\right)^{0.334}\left(1+\frac{8v}{u}\right)^{0.167}\right] \quad (51)$$

$$v = \frac{4Q}{\pi r_2^2 D C_p} \quad (52)$$

where, k, Q, v and u are respectively conductivity, flow rate, cooling air velocity and fiber velocity.

4.2.3 Helix movement modeling

The extruded microfibers from nozzle are passed through electromagnetic field when high voltage is applied between nozzle and counter electrode. The combination of electric and magnetic forces is Lorentz force on a point charge. Thereby the fibers have helix

movements until reaching counter electrode. Figure 21 shows schematic of Lorentz force (F_L) in melt electrospinning.

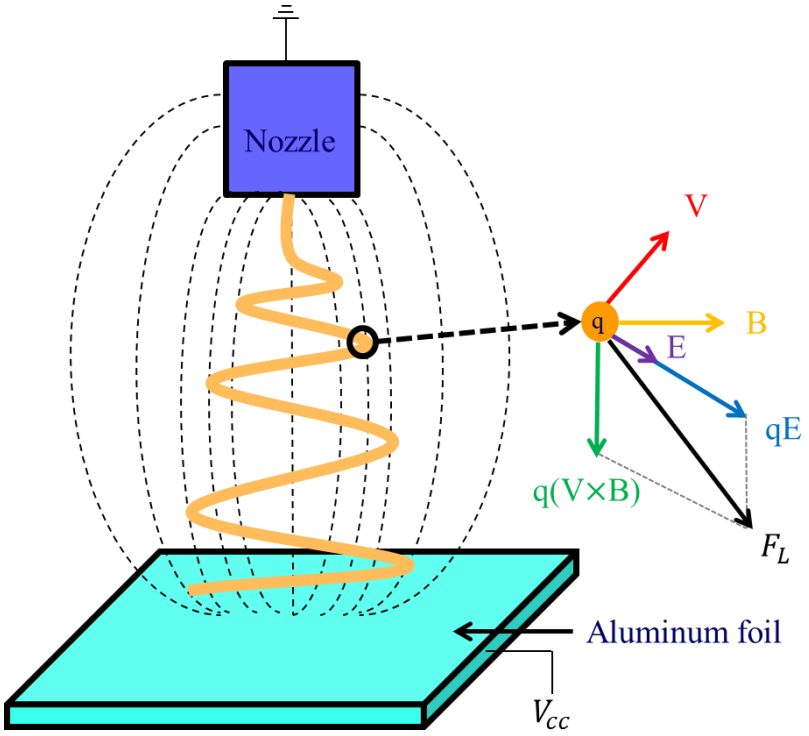

Figure 21. Schematic of Lorentz force in melt electrospinning (E: electric field, V: velocity of electron, B: magnetic field)

The Lorentz force (F_L) calculated by:

$$F_L = q \times (E + V \times B) \tag{53}$$

$$E = \frac{k_e q}{z^2}, V = \frac{P}{Me}, B = \frac{\mu_0 I}{4\pi}\int_0^l \frac{dl \times \hat{r}}{r^2} \tag{54}$$

where, E, q, P, Me, μ_0, I, l, k_e, r are respectively electric field intense, charge, momentum of electron, mass of electron, magnetic constant, current, length of wire, electric field coefficient, and distance from wire, which are given in Table 4.

Table 4. Parameters used for numerical simulations

Parameters	Literature and Standard data
Conductivity (*k*)	0.132
Electric field coefficient (k_e) **[109]**	$9.0 \times 10^9 Nm^2/c^2$
Momentum of Electron (*P*)	1.03434×10^{-11}kgm/s
Mass of electron (*Me*)	$9.10938291 \times 10^{-31}$

Magnetic constant ($\boldsymbol{\mu_0}$) **[109]**	$4\pi \times 10^{-7}\ N/A^2$
Specific heat for PCL polymer ($\boldsymbol{C_p}$) **[108]**	$(0.3 + 6 \times 10^{-4}T) \times 4 \times 182 \times 10^7$
Flow rate (Q)	2ml/h
Activation energy, ($\boldsymbol{E_n}$)	10.1 kcal/mol
Gas constant, (R)	1.9872 cal/K·mol
Friction constant ($\boldsymbol{\mu_1}$) of aluminum foil	0.61
Permittivity of vacuum ($\boldsymbol{\varepsilon_0}$) **[85]**	$8.854187817 \times 10^{-12}F/m$
Melt temperature ($\boldsymbol{T_m}$)	60˚C
Ambient temperature ($\boldsymbol{T_a}$)	20˚C

4.2.4 Three dimensional (3D) scaffold modeling

The topology of scaffold is determined by radius of helix movement (R), linear transitional speed (v_L), and overlapped force (F_o) including fiber radius (r2) and fiber velocity (v) calculated from the previous sections. Figure 22A shows a schematic of helix movement on flat surface as a substrate. The acceleration of the electrospun fibers on the substrate is equal to the sum of the forces on the fibers divided by mass of the microfibers according to Newton's second law and we assume the initial displacement is close to zero.

Therefore, the radius of helix movement (R) is defined by:

$$R(t) = \int_0^{t_e}\int_0^{t_e} \frac{F_L\cos\theta_1 - (F_T + F_o)}{m(t)}\,dt\,dt \tag{55}$$

$$F_T = F_{T1}\sin\theta_2 + F_{T2},\ F_{T1} = F_s + F_v + F_g + F_e,\ F_{T2} = \mu_1 m(t_e)g + m\frac{v_L}{dt} \tag{56}$$

$$m(t) = \pi r_2^2(t) l_L D(t) \tag{57}$$

$$t_e = \frac{z}{u(t)} \tag{58}$$

where, m(t) is mass of microfiber, tension force (F_T) on flat surface has two components which are F_{T1} and F_{T2}, t_e is microfiber's reaching time to counter electrode after straight jet, l_L is fiber length applied Lorentz force, and μ_1 is friction constant of aluminum foil which is given in Table 4.

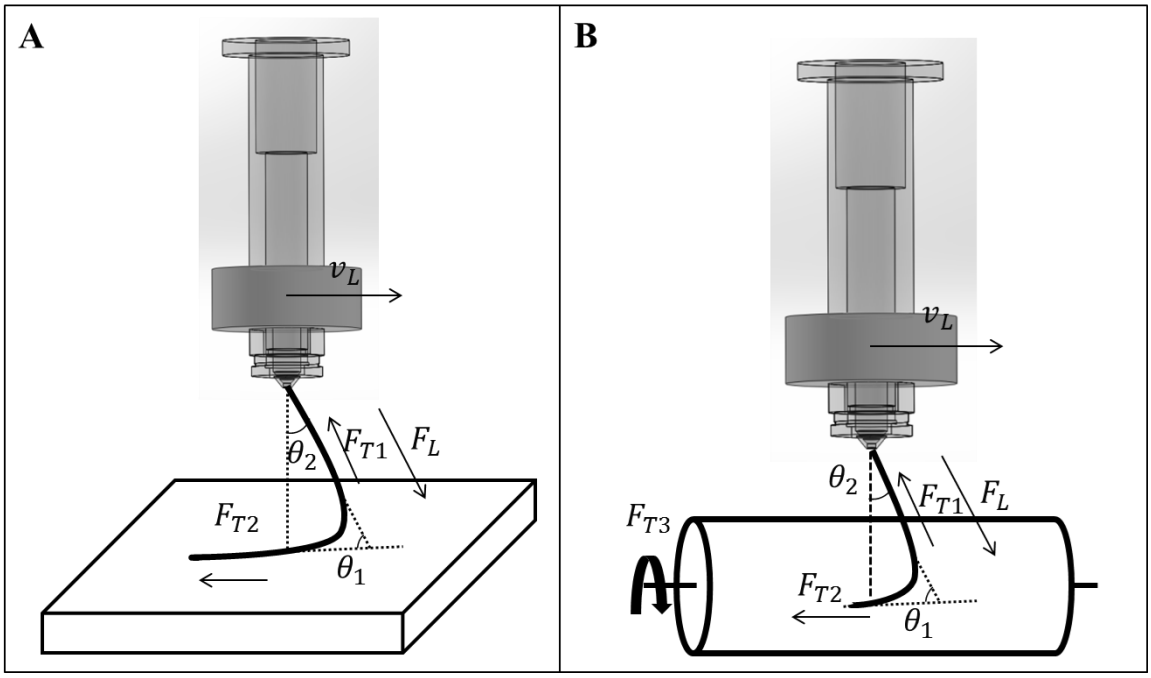

Figure 22. Schematic of helix movement on (A) flat surface and (B) round surface

Figure 23 shows topology of microfibers using 300μm nozzle, 20kV voltage, and 5cm distance in melt electrospinning. The microfibers in Figure 23(A) have loop patterns in melt electrospinning because of Lorentz force. In the meantime, overlapped force (F_o) is happened among fibers, which is a pulling force each other molten condition's fibers in adjacent distance. The overlapped force (F_o) is calculated by [21]:

$$F_o = \frac{1}{4\pi\varepsilon_0}\frac{q}{a(t)^2}, \qquad T \geq T_m \tag{59}$$

where, a(t), T, T_m,ε_0 are respectively the adjacent distance of electrospun microfibers, polymer fiber temperature calculated by Eq. (50), melt temperature, and permittivity of vacuum. Figure 23(B) demonstrates the results of the overlapped force applied (solid line) and non-applied (dash line).

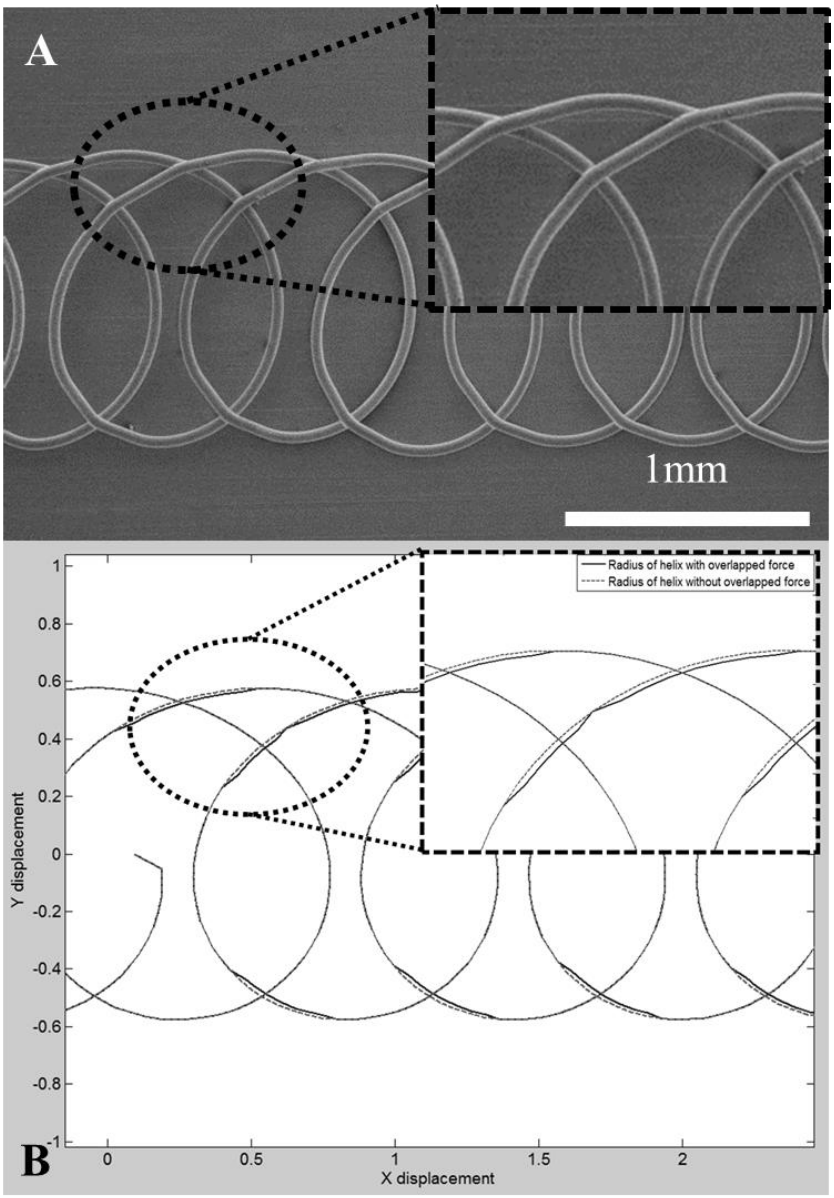

Figure 23. Topology of microfibers using 300 µm nozzle, 20kV voltage, and 5cm distance; (A) Experiment, (B) Simulation

Figure 22B demonstrates a schematic of helix movement on round surface as a substrate.

Tension force (F_T) on round surface is calculated by sum of three components:

$$F_T = F_{T1}\cos\theta_2 + F_{T2} + F_{T3} \tag{60}$$

$$T_1 = F_s + F_v + F_g + F_e,\ T_2 = \mu_1 m(t_e)g + m\frac{v_L}{dt},\ T_3 = \mu_1 m(t_e)g + m\frac{2\pi R_D \alpha}{dt} \tag{61}$$

where, α, and R_D are respectively drum angular velocity and drum radius. The radius of helix movement in case of round surface can be acquired as substituting the tension force to Eq. (55).

The porosity of fabricated scaffold ($\emptyset_{\mathrm{mesh}}$) is defined by[108]:

$$\emptyset_{\mathrm{mesh}} = \left(1 - \frac{\pi r_2^2 \int \mathrm{udt}}{V_s}\right) \times 100\ \% \tag{62}$$

where, V_s is volume of whole scaffold.

4.3 Experimental procedure

4.3.1 Fabrication of microfibers

Poly (ε-caprolactone) (PCL, Mn ~45,000) was acquired from (Sigma Aldrich, USA) with a melting point of approximately 60°C. The details of our custom-made melt electrospinning setup have been already published [9, 25]. In summary, we have applied 10kV to 20kV to the molten PCL at 80˚C using a high voltage power supply (Gamma High Voltage Research Inc., USA) with the working distance between the nozzle and counter electrode ranging from 5cm to 20cm. The PCL granules were heated to the desired temperature after the granules were dispensed into melting chamber with the nozzle attached. To our knowledge, parameters such as nozzle diameter, processing temperature, collection distance, applied voltage, flow rate of syringe pump and linear velocity of x and y axis in CNC machine are related to fiber diameter and morphology of scaffold in melt electrospinning. The influence of electrical force (F_e), nozzle diameter (r_1), counter electrode distance (z), porosity of scaffold ($\emptyset_{mesh}$) and linear velocity (v_L) in morphology of scaffold were investigated in numerical simulation and experiment [108].

4.3.2 Analysis of microfiber topography

To image these scaffolds using scanning electron microscopy (SEM), all electrospun microfibers were coated using Cressington 208 carbon coater two times for 6 seconds at 10-4 mbar and accordingly samples were transported to loading stubs for Hitachi S-4800 field emission scanning electron microscope. Low magnification images were captured at 1 kV with approximately 8 mm working distance. Fiber diameters and radius of helix were characterized by Quartz-PCI Image Management Systems® [108].

4.4 Parameter analysis in numerical simulation

4.4.1 Parameters study depended on various temperatures

The influence of temperature on the other melt electrospinning parameters (density of PCL, viscoelastic force, electrospinning speed, fiber diameter) was examined by simulation. The applied voltage, distance between nozzle and counter electrode, flow rate, linear transitional speed, and nozzle diameter are fixed all respectively at 20kV, 5cm, 2ml/h, 8.5mm/s, and 300μm in order to restrict the parameters effects. Viscosity and density of PCL polymer strongly depends on temperature and it eventually influences to viscoelastic force, electrospinning speed, and fiber diameter as shown in Figure. 24. The density of PCL is changed from 0.7957 (g/cm^3) to 0.3440 (g/cm^3) when the temperature is changed from 80 ˚C to 150 ˚C in Figure 24(A). Figure 24(B) shows increases of viscoelastic force in higher temperature. Electrospinning velocity (u) is increased from approximately 100mm/s to 180 mm/s because of low viscosity resulted from temperature as shown in Figure 24(C). As the results, the fiber diameter is

decreased by approximately 0.020mm when temperature is varied from 80 ˚C to 150 ˚C as shown in Figure 24(D).

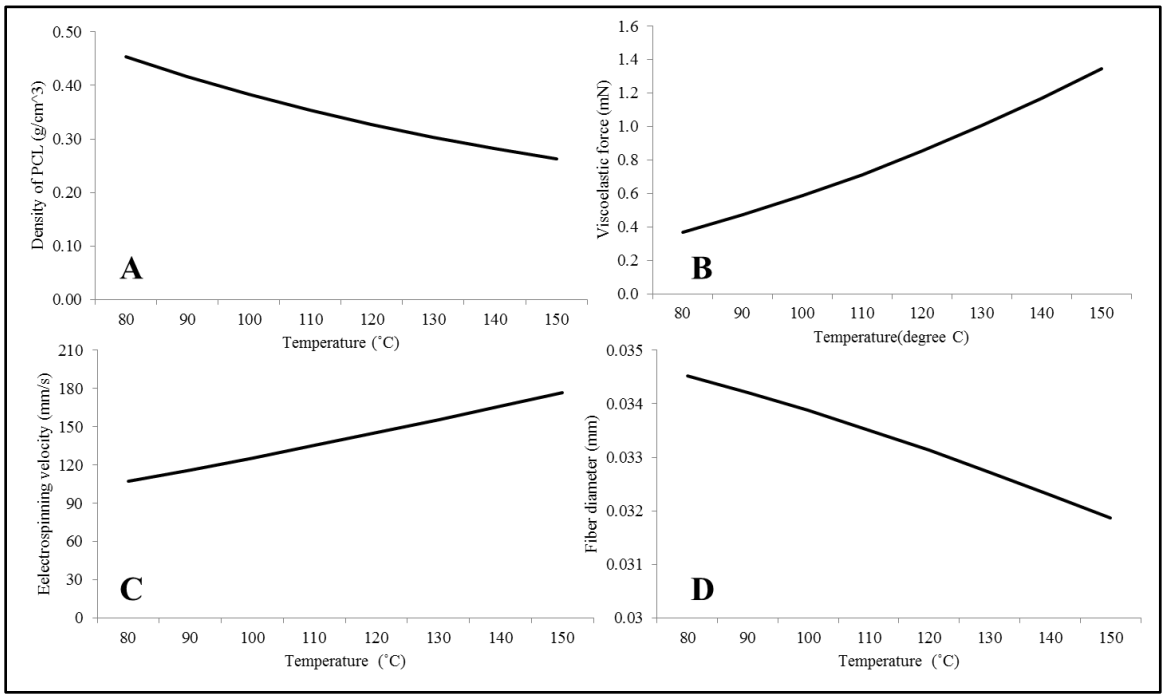

Figure 24. Parameters variation in various temperatures

4.4.2 Parameters study depended on various linear transitional speeds

Figure 25 shows the effects of various linear transitional speeds on the resulting tension force and radius of helix. To limit the other parameters effects, the applied voltage, distance between nozzle and counter electrode, flow rate, temperature and nozzle diameter are fixed all respectively at 20kV, 5cm, 2ml/h, 80 ˚C, and 300μm. Figure 25(A) demonstrates tension force in various transitional speeds on flat surface counter electrode. The tension force influenced on electrospun microfibers is changed from approximately 0.04N to 0.09N when the speed is varied from 8mm/s to 20mm/s. According to Eq. (55), the radius of helix is inversely proportional to the linear transitional speed as shown in Figure 25(B) so it is changed from 0.55mm to 0.31mm when the linear transitional speed

is varied from 8mm/s to 20mm/s.

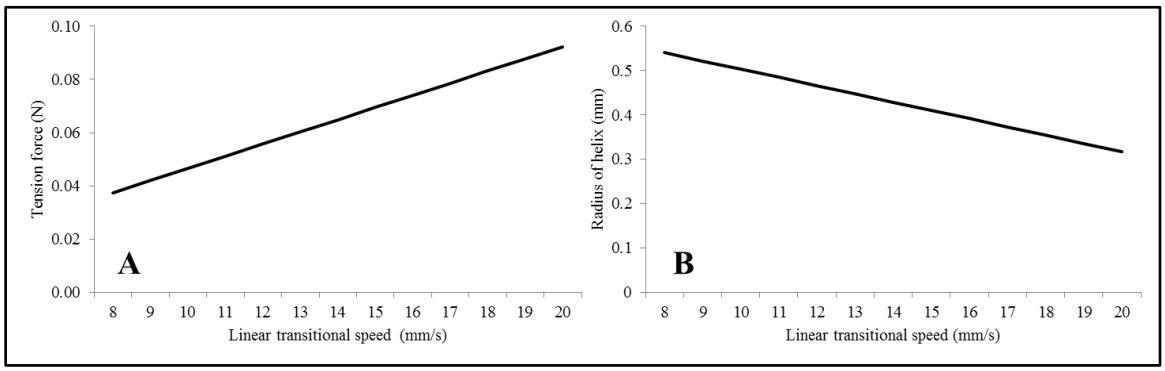

Figure 25. Parameters variation in various feed rate

4.4.3 Parameters study depended on various flow rates

The flow rate of melt PCL affects the volume of the system at any time so the parameter makes changes in electrical force, tension force, gravity force, Lorentz force, electrospinning speed, and radius of helix as shown in Figure 26. The other parameters (the applied voltage, distance between nozzle and counter electrode, temperature, linear transitional speed and nozzle diameter) are respectively fixed at 20kV, 5cm, 80 ˚C, 8.5mm/s and 300μm in order to study effect of the flow rate. Electrical force shows decrement of 2.7% since surface tension is increased, tension force presents decrement of 3.7% because the electrical force is decreased, gravity force demonstrates increment of 11% since the amount of PCL is increased, and Lorentz force displays decrement of 2.9% because the gravity force is increased when flow rate is increased from 2ml/h to 10ml/h as shown in Figure 26(A-D) and initial volume increased by higher flow rate is increasing electrospinning velocity as presented in Figure 26(E) and thereby the radius of helix is decreased by approximately 0.030mm since Lorentz force is decreased when the flow

rate is changed from 2ml/h to 10ml/h as shown in Figure 26(F).

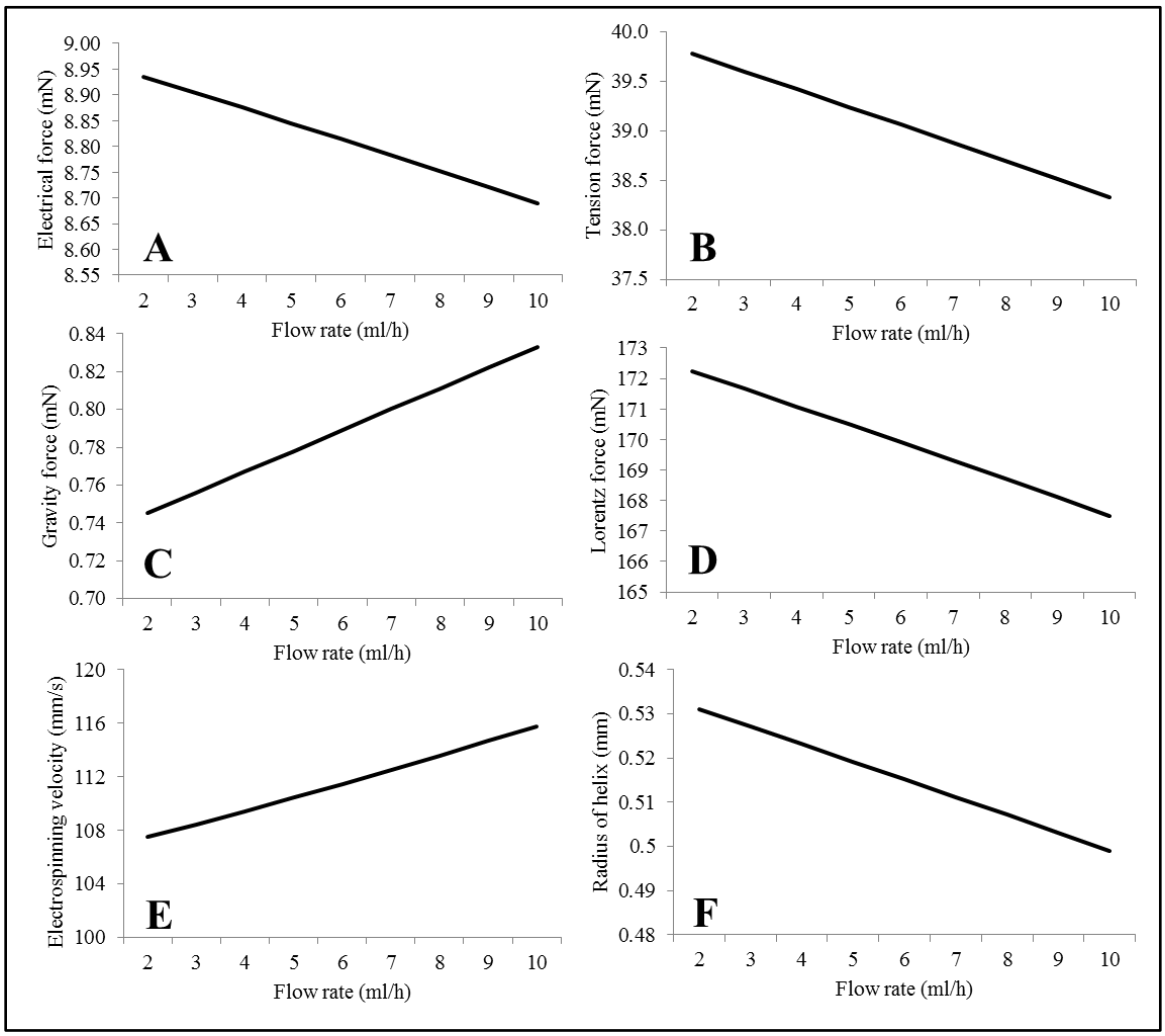

Figure 26. Parameters variation in various flow rate

4.4.4 Effects of nozzle diameter, applied voltage, distance, linear transitional speed in various temperatures

In our previous paper [108], we compared numerical and experimental results and confirmed our modeling to be reliable at 80 ˚C. The predictions of fiber diameter and porosity under ambiguous parameters including various temperatures are shown in Figure 27, with conditions (20kV applied voltage, 5cm distance, and 2ml/h flow rate). The fiber

diameter replied on the diameter of the nozzle and it shows linear proportional to the nozzle diameters and proportional to the diameters in various temperatures as well. However, the proportional ratio is slightly decreased when the temperature is increased from 80 ˚C to 150 ˚C as shown in Figure 27 (A). We can expect that distance and applied voltage have an inverse relationship according to Coulomb's law and influence fiber diameter inversely as well. Moreover, the curves of 100 ˚C to 150 ˚C in temperature have similarity with the curves of 80 ˚C but they are overall shifted down as shown in Figure 27 (B) and (C). Figure 27 (D) shows porosity of scaffolds depended on various temperatures. The porosity of microfibers in 80 ˚C shows 83% when the transitional speed is 8.5mm/s while the porosity in 150 ˚C demonstrates 91% when the speed is 8.5mm/s. The faster convergence to approximately 90 % porosity is at higher temperature.

.

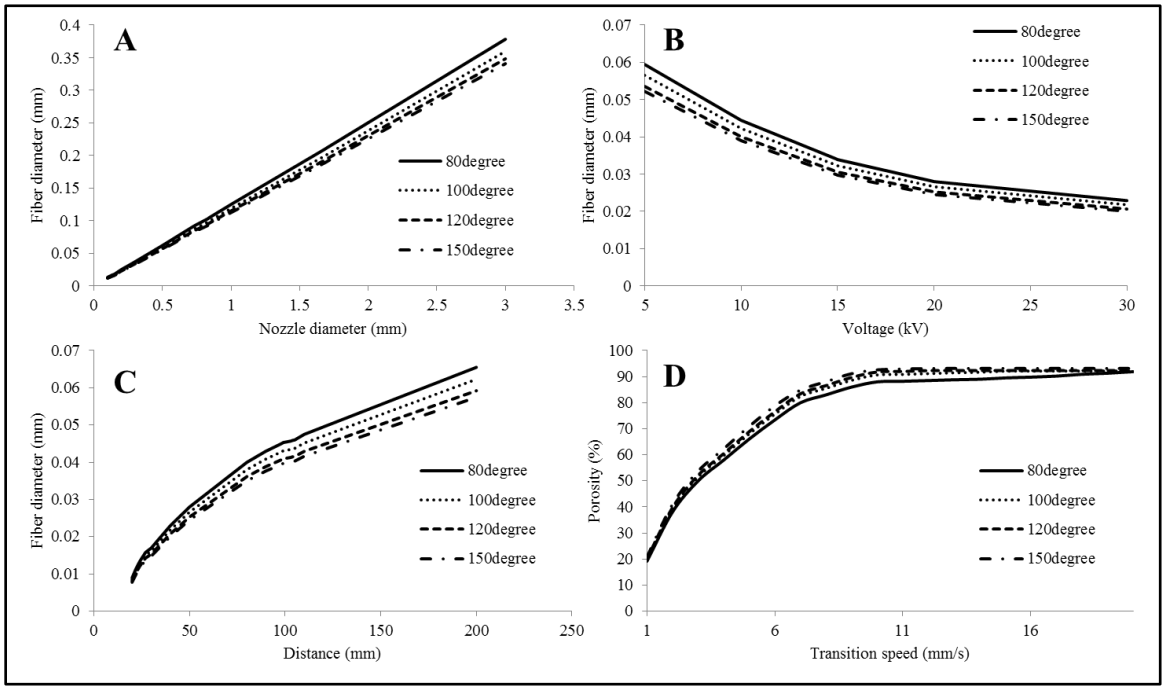

Figure 27. Predictions of fiber diameter and porosity under ambiguous conditions including various temperatures

4.5 Numerical simulation and experimental results

4.5.1 Effects of temperature influenced on fiber diameter and radius of helix

The effect of temperature on the fiber diameter and radius of helix is studied by simulation and experiment. The simulation and experiment are conducted under the same conditions which are 300μm nozzle, 5cm distance, 20kV voltage, 2ml/h flow rate, and 8.5mm/s transitional speed. Figure 28 (A) and (B) present a comparison of numerical and experimental fiber diameter and radius of helix for various temperatures. The increase in temperature would eventually affect viscoelastic force and density to stretch out fibers according to Eq. (45) and (48). Experimentally, that eventually would lead to the fiber diameter decreasing from 0.041 ± 0.008 to 0.028 ± 0.005 mm (n=5) as the temperature increases from 80˚C to 150 ˚C. In simulation, the fiber diameter decreased from 0.034 to 0.030 mm as the temperature increased from 80˚C to 150 ˚C. Moreover, radius of helix decreases from 0.52 to 0.43mm in the simulation. Experimental radius of helix in Figure 28 (B) is varied from 0.64 ± 0.17to 0.42±0.11mm (n=5) when temperature is increased from 80˚C to 150 ˚C.

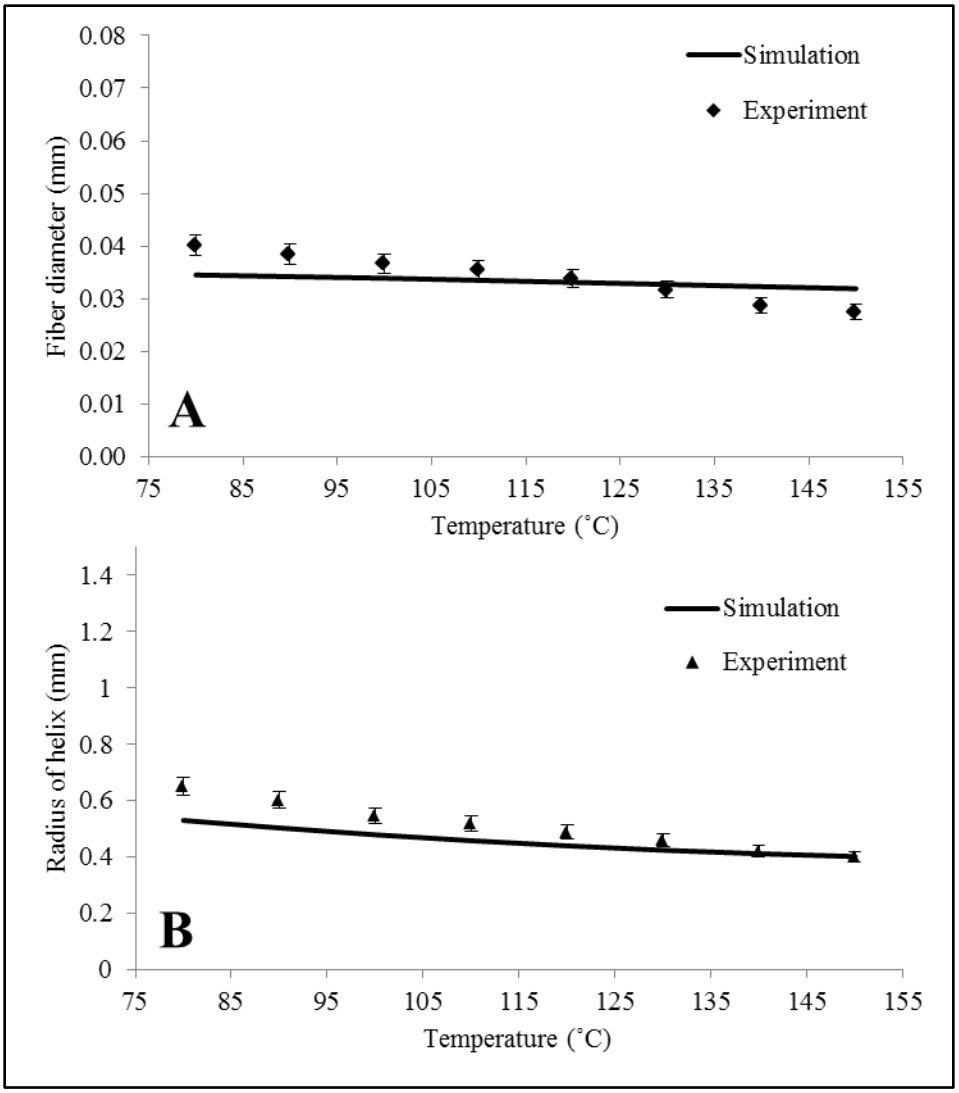

Figure 28. Results of fiber diameter (A) and radius of helix (B) controlled by temperature in simulation and experimental results. (n=5)

4.5.2 3D tubular scaffold topology controlled by linear transitional speed

The transitional speed (v_L) in scaffold modeling is a significant parameter to define the topology of controlled tubular scaffolds. Figure 29 shows that (8 mm × 100mm) (inner diameter × length) numerical and experimental topology depended on various transitional speeds at 300μm (nozzle diameter), 20kV (applied voltage), 5cm (distance), 80˚C (temperature), 1.04 rad/s (angular velocity), and 2ml/h (flow rate). (A), (B), and (C)

in Figure 29 respectively represent 4.25mm/s, 8.50mm/s, and 17.00mm/s transitional speed. The rolling angle of microfibers on round substrate shows respectively 56˚, 42˚, and 23˚ at 4.25mm/s, 8.50mm/s, and 17.00mm/s in experimental data. In numerical simulation, the angle shows respectively 55˚, 42˚, and 22˚ at the same transitional speed. If v_L is increased, the radius of helix (R(t)) is decreased since tension force (F_T) on microfibers is increased. The intervals between tori thereby become sparser when transitional speed is increased.

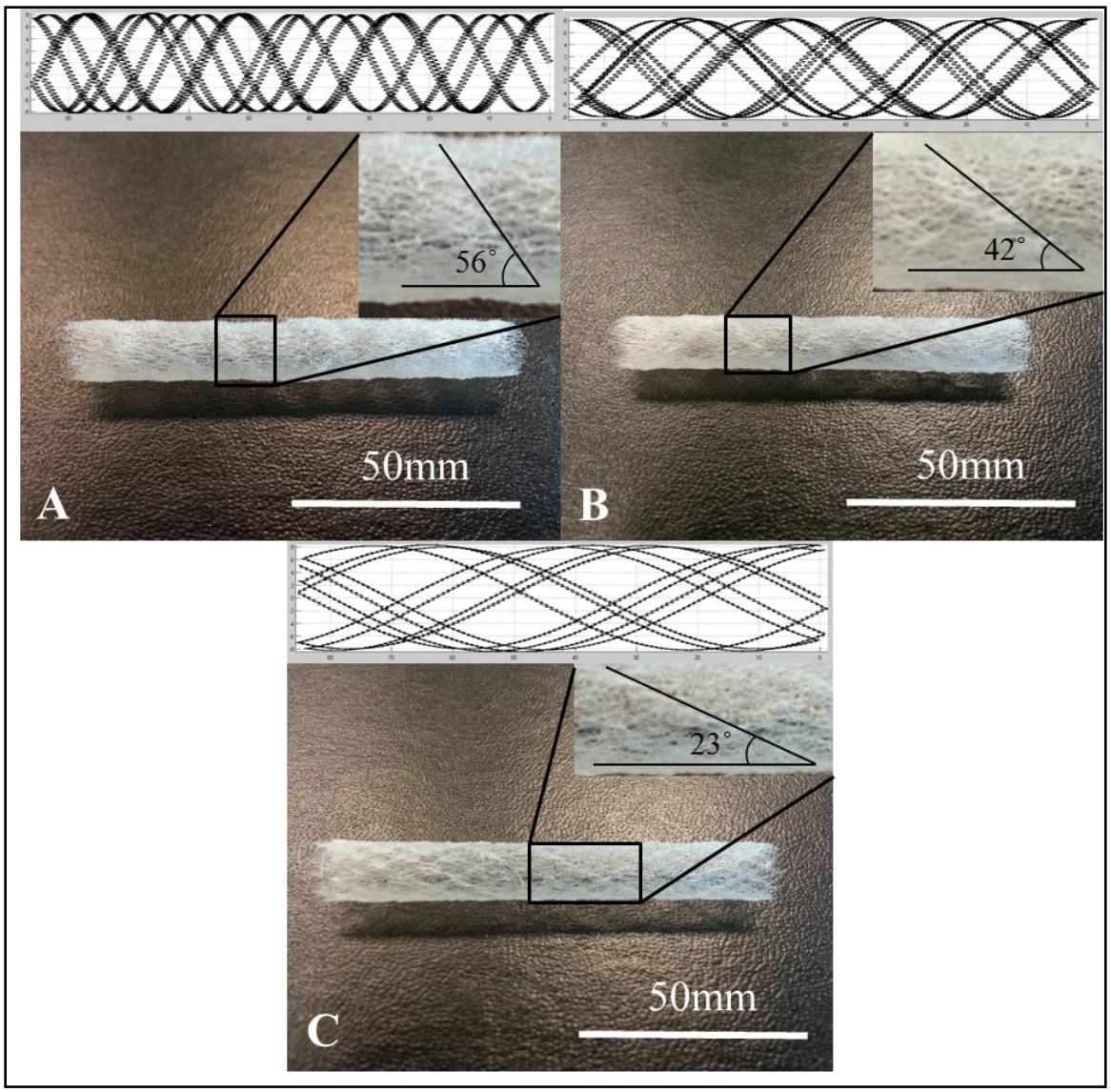

Figure 29. 3D tubular scaffold topology depended on transitional speed. (A) 4.25mm/s, (B) 8.50mm/s, (C) 17.00mm/s

4.5Discussion

Mathematical modelling approaches can be used to predict the topographical dependency of microfiber scaffolds on various operational parameters for better understanding of melt electrospinning technique through the use of numerical studies and comparing the results with experimental data[21, 80, 105, 108]. The main advantage of

melt electrospinning technique is to fabricate a controllable and predictable structure which can provide specific physical and mechanical properties, and more importantly topographical properties for different applications especially in the field of tissue engineering and delivery of cells in a controllable fashion[16, 44, 89, 95, 96, 103]. For instance, the topographical properties of melt eletcrsopun scaffolds can direct stem cell differentiation into neural phenotypes[95]. Thus, a trustworthy approach such as mathematical modelling must be used to control topographical properties [107, 108]. The topographical properties have been previously shown to be drastically affected by several operational parameters[21, 44, 81, 92, 99, 105, 107-109]. However, here we reported the dependency of helix movement on electric and magnetic forces. In addition, 3D modelling was done to study the behaviour of helix movement and linear transitional speed.

Using numerical simulations, the effect of temperature on controlling topographical properties was also studied by investigating the effect of temperature on density, viscoelastic force, electrospinning speed and also fiber diameter. The aim of this study was also to predict the effect of linear transitional speed on most important forces involved in the melt electrospun process. These forces include tension forces, electrical forces, Lorentz force and also gravity forces. The dependency of such forces on linear transitional speed was studied. The effect of flow rate was also considered to further investigate the effect of these forces along the change in radius of helix as one of the most important topographical properties of such scaffolds.

In order to produce an effective model to further predict the key topographical properties such fiber diameter and porosity [21, 80, 105, 107], it was necessary to study

the effect of nozzle diameter and voltage on fiber diameter. We also studied the impression of distance on fiber diameter. Moreover, the porosity of such scaffolds was shown to be strongly affected by linear transitional speed. We could successfully study these effects while varying temperature from 80˚C to 150˚C as well. Among many studies, we believe that our previous and current models could be introduced as one of the most commonly applicable models for controlling topographical properties which are needed in neural tissue engineering applications. The fiber diameter was increased 5 times when nozzle diameter changed from 0.5 mm to 2 mm. The fiber diameter was also reported to be drastically changed by altering the applied voltage, and it was reported to be around 0.045 mm when the applied voltage was 10 kV at 80˚C and it decreased to around 0.03 mm when the applied voltage was increased to 20 kV at the same temperature. Interestingly, porosity of fibrous scaffolds cells showed a strong dependency transition speed. The trend was almost similar when changing the temperature from 80 ˚C to 150 ˚C indicating that the porosity of scaffolds are more likely dependent on transition speed than temperature of spinning. The porosity of scaffolds was significantly higher (~ 90 %) when the transition speed was 16 mm/sec compared to the situation in which the speed was 1 mm/sec (~ 20 % of porosity). These results suggest that the fiber diameter and porosity of microfibers could be influenced the by key operational parameters such as nozzle diameter, voltage and transition speed.

We reported that temperature could significantly change the micro scale topography properties such as fiber diameter and helix radius. Fiber diameter of scaffolds was significantly decreased when the melt electrospinning temperature increased from 80 ˚C to 150˚C. Moreover, the helix radius of fibrous scaffolds was 150 % larger at 80 ˚C when

compare to 150 ˚C. This represents that the topographical properties were significantly controlled by melt electrospinning temperature.

In this study, we successfully developed our previous model to enhance its feature to control the topographical properties of melt electrospun fibrous scaffolds. Our mathematical model can be used to investigate the effects of different key parameters such as temperature, feed rate, flow rate, fiber diameter and porosity. Such flexibility makes this model attractive for tissue engineers and their desired applications. We have chosen PCL, a commonly used biodegradable polymer which is tailorable in its mechanical properties, rate of surface and bulk biodegradation, solubility and crystallinity, and structure topography[95]. We have also evaluated the performance of such model to investigate the topographical properties of tubular scaffolds which can be used for nerve tissue engineering approaches especially for peripheral nerve injures. On-going work is investigating the effects of viscoelastic properties of polymer melt and also its molecular weight on controlling the topographical properties of melt electrospun fibrous scaffolds to further our current mathematical model.

4.6 Conclusion

The aim of this research is to add helix movement modeling and three dimensional scaffold modeling to our previous models to predict radius of helix and topography of scaffold incorporating nozzle size, counter electrode distance, applied voltage, temperature, linear transitional speed, and flow rate. Experimentally elusive variable effects are demonstrated through numerical simulations at the fixed conditions. For instance, density of PCL shows decrement of 57%, viscoelastic force presents increment of 250%, electrospinning velocity demonstrates increment of 80% and fiber diameter

displays decrement of 8% when temperature is increased from 80˚C to 150˚C while fixing all other variables. Tension force presents increment of 125% and radius of helix shows decrement of 36% when linear transitional speed is varied from 8mm/s to 20mm/s. Electrical force shows decrement of 2.7%, tension force presents decrement of 3.7%, gravity force demonstrates increment of 11%, and Lorentz force displays decrement of 2.9% when flow rate is increased from 2ml/h to 10ml/h. The effect of temperature on the fiber diameter was evaluated and the simulation results are compared with experimental data. The fiber diameter presents decrement of 32% when the temperature increases from 80˚C to 150 ˚C. In simulation, the fiber diameter demonstrates decrement of 12% as the temperature increased from 80˚C to 150˚C. Moreover, radius of helix shows decrement of 17% in the simulation. Experimental radius of helix presents decrement of 34% when temperature is increased from 80˚C to 150 ˚C. Finally, morphology of tubular scaffold is controlled by linear transitional speed. The rolling angle of microfiber on the round substrate presents respectively decrement of 60% and 59% and in simulation and experiment when the linear transitional speed is changed from 8.5mm/s to 17mm/s. In addition, the fabricated tubular scaffold becomes sparser in the faster transitional speed in both simulation and experiment. The reliable mathematical modeling enabled to predict and design morphology under various parameters holds great promise for specific scaffold fabrication.

Chapter 5. Combining melt electrospinning and particulate leaching for fabrication of porous microfibers[3]

5.1 Introduction

The electrospinning process is an attractive method of producing polymer fibers and is gaining more attention for scaffold fabrication in the field of tissue engineering. There are two types of electrospinning techniques: solution and melt electrospinning, where nanoscale and microscale fibers are produced, respectively. Solution electrospinning requires a solvent to dissolve a given polymer type, whereas melt electrospinning involves the heating of the polymer to melting temperature, in each case producing a viscous fluid that can be drawn into fibers. Melt electrospinning holds some advantages over solution electrospinning in tissue engineering applications because toxic solvents need not be used. Also, microfibers from melt electrospinning provide structural rigidity and integrity for a scaffold and allow for better control over scaffolds' structural geometry and shape [110]. Thus, melt-electrospun fibers are frequently finding their place in many diverse applications, such as in tissue engineering, implant material, and drug delivery [111]. However, due to relatively large fiber diameter at the microscale, porosity of the melt-electrospun scaffold is limited and difficult to control.

Porosity control of scaffolds for tissue engineering is important, as when fiber scaffolds are used in cell transplantation, porosity directly impacts the cell growth and nutrient transportation [112]. Thus, generating porous fibers in scaffolds increases cell attachment,

[3] The following chapter is from: **Combining melt electrospinning and particulate leaching for fabrication of porous microfibers**. Junghyuk Ko, et al. Accepted for publication by the Journal of Manufacturing letter in 2015. Copyright Permission Approved.

drug loading, and free nutrient transportation [111]. Efforts have been made to fabricate fiber sheets or mats with some level of control over porosity via melt electrospinning [110, 113-115]. However, as melt electrospinning is a relatively new technique for fiber generation, porosity control studies utilizing particulate leaching for melt-electrospun fibers has not been conducted.

In this thesis, the technique of particulate leaching is combined with melt electrospinning to produce porous polymeric fiber structures. Particulate leaching has been used in past studies to generate porous structures [116, 117], but it has not been combined with melt electrospinning to generate porous fibers. Particulate leaching is a process where porogen is added to the molten polymer before molding and extracting it afterwards, creating porous structures due to its extraction. In this thesis, water soluble sugar particles are used as porogen. Poly (ε-caprolactone) (PCL) is chosen as the polymer for electrospinning due to its low melting point, low cost, and longer-term biodegradability and biocompatibility [86, 118]. These two compounds are mixed at the molten state, and fibers are produced from the mixture via melt electrospinning. Electrospun fibers are then placed in water, allowing the sugar to leach from the fibers. As the sugar leaches, it leaves pores in the fibers, which increases the porosity of the fibrous structure and also increases roughness of the fiber surfaces. Research was conducted to control the fiber porosity by utilizing particulate leaching in melt electrospinning. As the level of porosity depends on the pores' size, shape, and distribution [119], the effect of different concentrations of sugar in the mixture and process conditions on porosity is also investigated.

5.2 Material and methods

5.2.1 Melt electrospinning setup

PCL with a melting point of 60°C was purchased from Sigma Aldrich, USA (Mn ~45,000). A custom-made melt electrospinning apparatus was used [110]. Two nozzle diameters were used: 500µm and 1000µm. During the melt electrospinning process, 20kV was applied to the molten, sugar-containing PCL using a high voltage supply. A wooden plate covered in aluminum foil was used as the counter electrode and to collected electrospun fibers.

5.2.2 Particulate leaching process

Table sugar with a melting point of 186°C was first melted on an aluminum foil using a hot plate. When the sugar became fully melted, PCL – having a lower melting point than sugar – was added into the melted sugar. Using a metal spatula, the PCL was evenly mixed into the sugar as it melted. After uniform mixing of PCL and sugar, the mixture was left at room temperature for solidification. The solidified mixture was then used in the melt electrospinning process. Sugar concentrations of 10, 20, and 30% by weight were added to PCL polymer prior to melt electrospinning.

5.2.3 Analysis of microfiber topology

Scanning electron microscopy (SEM) was used in order to observe the surfaces of the electrospun PCL fibers. The Cressington 208 carbon coater was used to coat PCL fibers prior to SEM imaging. The coated samples were loaded in a Hitachi S-4800 field

emission scanning electron microscope. High magnifications images with 1kV and 8mm working distance was used to observe the fiber surface.

5.2.4 Image processing

Adobe Photoshop CS5 and Matlab R2013a have been used for SEM image processing in order to compute porosity on the fiber surface. The pores on the fiber surfaces as shown in Figure 30A were picked out by clarifying the boundaries between microfibers and pores and using monochrome conversion in Photoshop. The pores were converted to white and the rest was converted to black as shown in Figure 30B. The surface porosity was calculated as the ratio of white and black areas, with the areas obtained by counting the white pixels in Matlab relative to the scale.

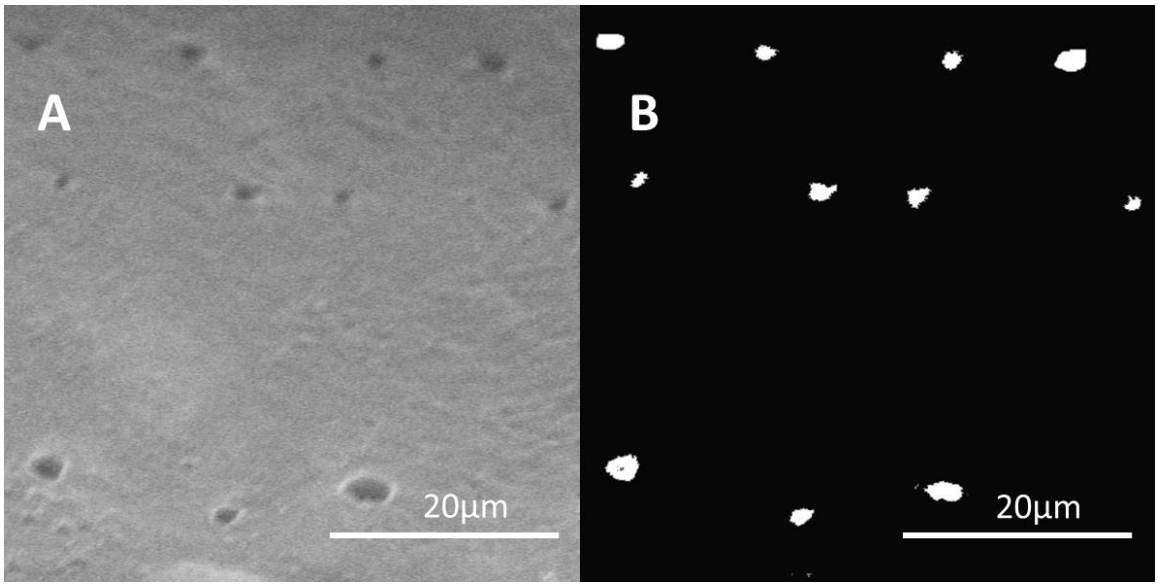

Figure 30. (A) Original SEM image and (B) processed SEM image

5.3 Results and discussion

Figure 31 shows SEM images of (A) PCL fibers before particulate leaching and (B) PCL fibers afterwards when 1 mm diameter nozzle and sugar concentration of 30% were

used. The differences between sugar leached and non-leached fibers indicates that sugar leached fibers exhibit higher porosity on the fiber surface than non-leached fibers. Figure 32 shows the surfaces of PCL microfibers with varied sugar concentrations: (A) pure PCL microfiber (0%), (B) 10% sugar concentration, (C) 20% sugar concentration, and (D) 30% concentration. As the sugar concentration added to the PCL polymer increased, the porosity of the fiber increased. A correlation between the increase in porosity and the increase in sugar concentration is displayed in Figure 33. As shown, with an increase in sugar concentration, porosity was also increased. The results of this experiment suggest a potential method to increase fiber porosity.

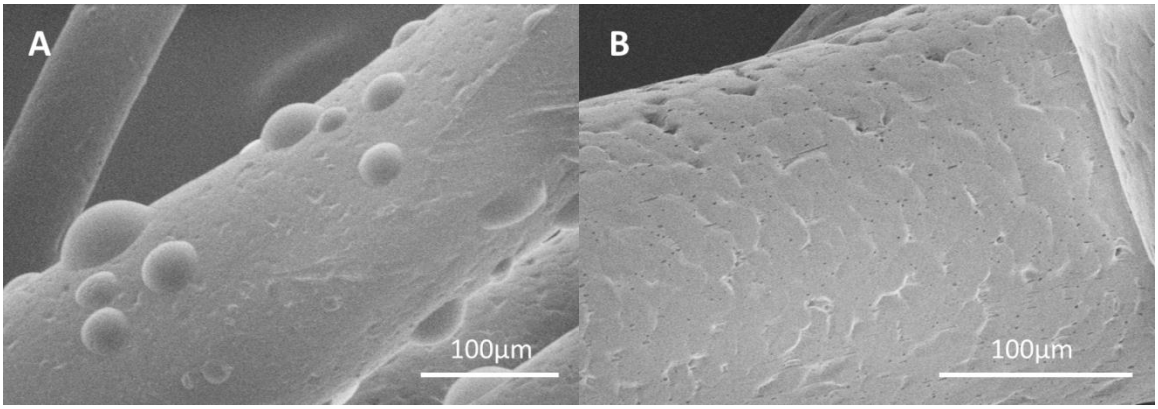

Figure 31. SEM images of melt electrospun PCL fiber surface with 30% sugar concentration with nozzle diameter of 1000µm; (A) PCL fiber containing sugar particles prior to leaching, (B) PCL fiber with sugar leached

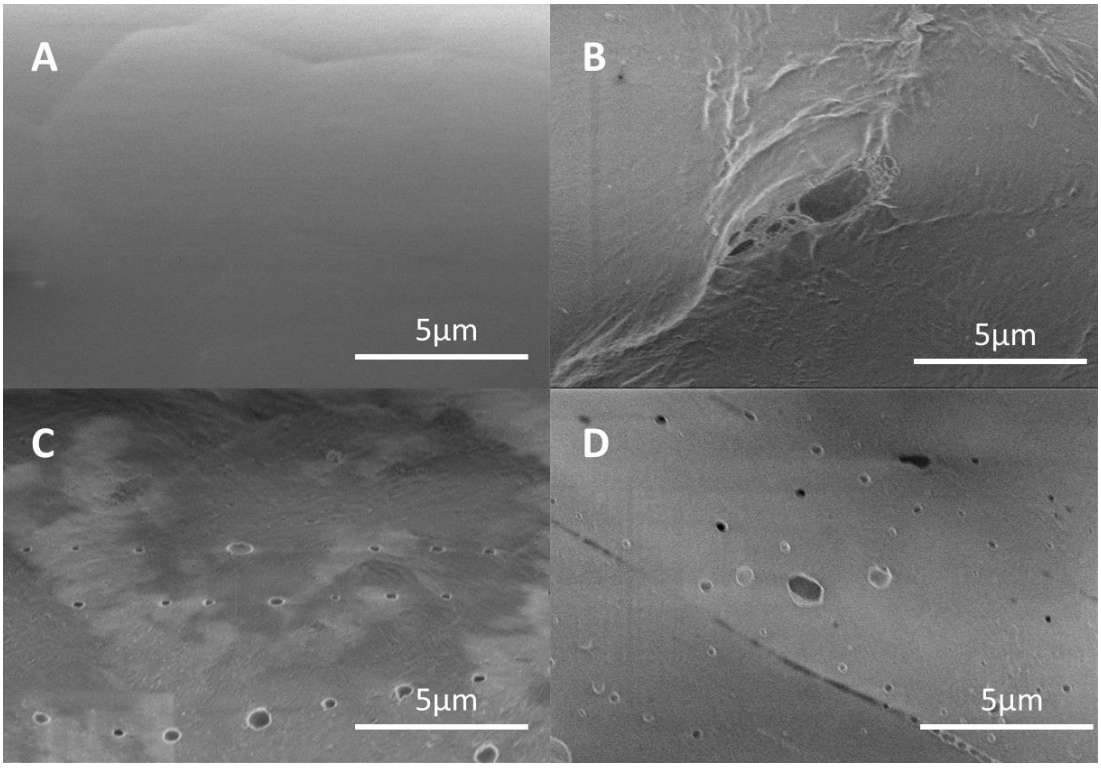

Figure 32. SEM images of Melt electrospun PCL fiber with different sugar concentration leached with nozzle diameter of 1000µm; (A) Pure PCL microfiber, (B) 10% sugar concentration, (C) 20% sugar concentration, (D) 30% sugar concentration

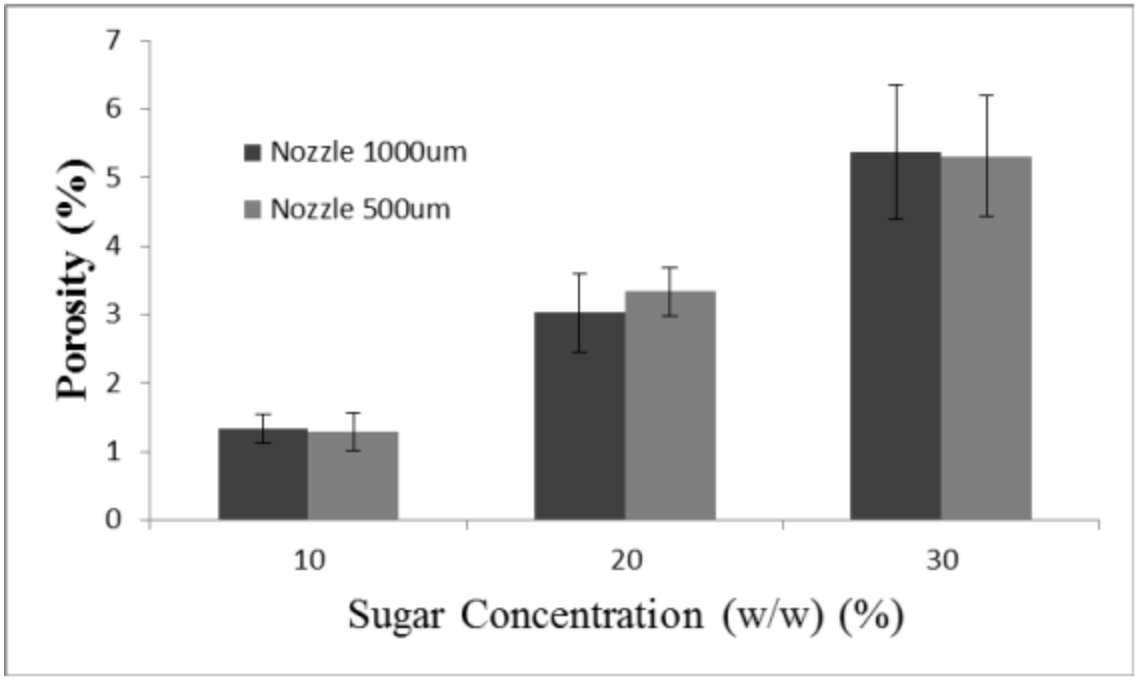

Figure 33. Effect of sugar concentration and nozzle diameter on porosity

Sugar concentrations of less than 10% were not experimentally performed due to low porosity value at 10% sugar concentration. Higher sugar concentrations of greater than 30% were also performed; however, concentrations of sugar higher than 30% resulted in discontinuous fiber generation. Thus, experimental results at higher sugar concentrations are not reported here.

Two different nozzle diameters of 500µm and 1000µm were used. Varying the nozzle diameter resulted in varied fiber diameter: the 500 µm and 1000 µm nozzles resulted in fiber diameters of an average 82 µm and 180 µm, respectively. As seen in Figure 33, the porosity values at different diameter nozzles are similar. This indicates that when particulate leaching is used, porosity is independent of the nozzle diameter.

5.4 Conclusion

Melt electrospinning of poly (ε-caprolactone) in combination with sugar particulate leaching were used to generate porous microfibers. The effects of increasing the concentration of sugar particles and varying nozzle diameters on the electrospun fiber porosity were analyzed. As the sugar concentration increases in the electrospun fibers, the porosity of the fiber increases. Fibers with two different nozzle diameters resulted in similar porosities, indicating that fiber porosity is independent of nozzle diameters. The results of this thesis suggest that sugar particulate leaching is a potential method to control porosity in melt-electrospun microfibers.

Chapter 6. Design and Fabrication of Auxetic Stretchable Force Sensor for Hand Rehabilitation[4]

6.1 Introduction

Rehabilitative instruments can considerably improve hand functionality in people with various hand injuries. Rehabilitation robotics is a special division in robotic research that targets the constructing of robotic devices as a way to assist people who are impaired, either by accident, or as required due to age or infirmity [120-122]. A typical rehabilitative robotic device consists of an actuator system to power designed prosthetic hands, a control mechanism to mimic human tendon-driven actuation system, and a sensor system to detect the position of substrate [120-122].

A sensor system is used to monitor the surrounding environment via sensors such as sonar, force, and various others. The selection of a sensor for rehabilitation requires careful consideration of the following factors: light weight, portable size, high position sensing accuracy, and the ability to be attached to human skin [120]. A force sensor is one of the primary candidates for this application, which suitably meets these goals [123]. The stretchable sensor investigated in this research can be firmly attached on the human skin and can measure force and displacement accurately and successfully.

Most researchers have studied Micro Electromechanical Systems (MEMS) to fabricate force sensors [124-126]; however, designers of these sensors have experienced difficulties when attempts have been made to attach them onto the skin due to a lack of

[4] Junghyuk Ko has a biosafety license issued by University of Victoria and the experiment of resistance test on human skin was approved.

shear flexibility. Thus, a melt electrospinning technique is proposed as a way to fabricate a skin attachable and stretchable sensor. A melt electrospinning process has received remarkable attention as it provides the ability to fabricate polymer fibers ranging in sizes from tens of nanometers to hundreds of micrometers [127]. Melt electrospinning is one polymer processing technique for producing polymeric fibers, and its advantages involve the ability to control the resulting physical, mechanical and topographical properties of the product [21, 44, 104, 110]. Moreover, electrospun microfibers are easily tunable in their mechanical properties as the diameter of the electrospun fiber is adjusted by controlling parameters such as the nozzle diameter, the applied voltage, the distance between nozzle and counter electrode, among others [110]. PCL has a low melting point (approximately 60˚C) and is a hydrophobic and biocompatible polymer. It is one of the most commonly used synthetic polymers for biomedical engineering applications, such as its use in tissue engineering. Melt electrospinning can provide high fabrication capability at a low cost for the production of force sensors using a PCL resin.

Here we demonstrate that PCL based force sensors were successfully produced and used to measure force with respect to displacement. Advantages include a high elasticity, large displacement, low hysteresis and ease of fabrication. These force sensors were also easily mountable and have an excellent degree of reproducibility [128, 129]. Moreover, materials exhibiting an auxetic effect are shown to have a negative Poisson’s ratio, as their patterned geometrical structures become thicker perpendicular to the applied force and then automatically return to their original form after the dissipation of stress as shown in Figure 34A. Microfiber and solid sheets were machined into an angled solid square geometry. Each unit cell contains four squares, each square contains four vertices,

and two vertices correspond to one hinge by use of laser machining as shown in Figure 34B.

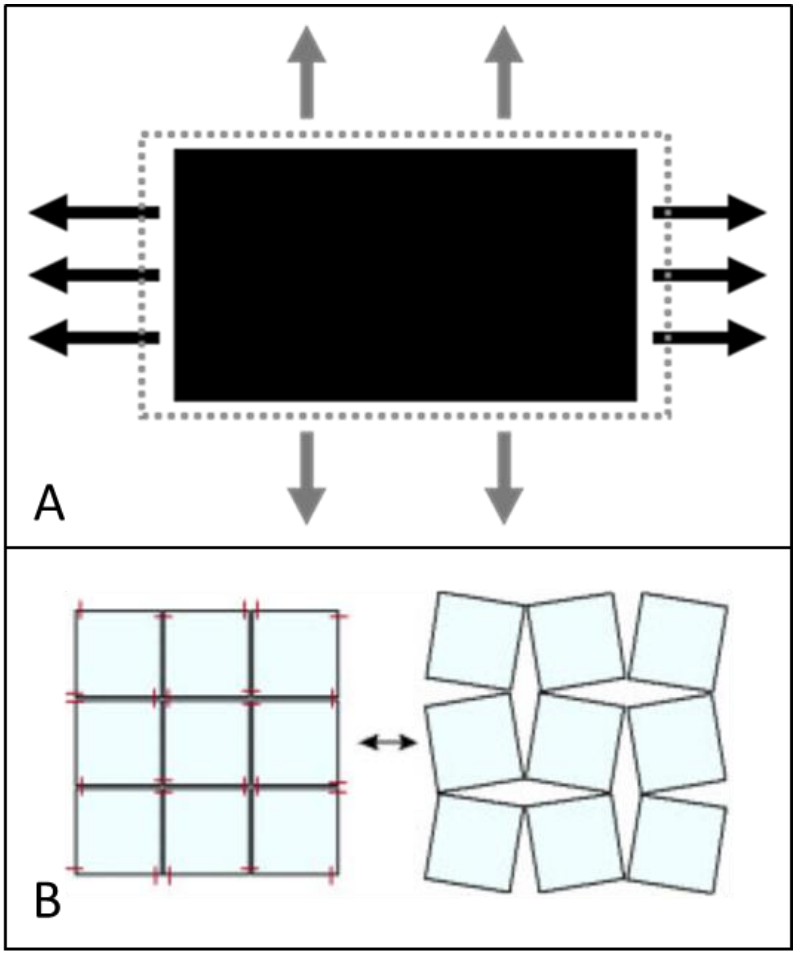

Figure 34. (A) Auxetic behavior of materials, (B) Geometrical design deformation mechanism of an auxetic design

Our stretchable sensor can be attached to the desired substrate and could potentially measure applied extensional force or displacement. We have developed four sets of samples, including a solid sheet (SS), a microfiber sheet (MS), an auxetic solid sheet (ASS), and an auxetic microfiber sheet (AMS). All samples were gold coated to fabricate electrically conductive sheets. The samples were experimentally characterized in order to measure their electrical conductivity. Finally, we demonstrate that the sensors can be used to measure fine variations of resistance on human skin.

6.2 Fabrication methods and sensor sheet

6.2.1 Melt electrospinning

PCL (Mn ~45,000) was supplied from Sigma Aldrich, USA. Its melting point is around 60 ˚C. A custom-made melt electrospinning apparatus (Figure 35A) contains a computer numerical controlled (CNC) machine (K2 CNC Inc., USA), a custom-made chamber press, a syringe pump (New Era Pump Systems Inc., USA), a heater (Heterwerks Inc., USA), a custom-made machined melting chamber, and a set of custom-made interchangable nozzles. The flat tipped nozzles were produced from aluminum 6061 with an internal diameter of 200 μm (~10 μm). Figure 35B shows a PCL microfiber sheet manufactured by a melt electrospinning process.

The applied voltage was 20kV using a high applied voltage supply (Gamma High Voltage Research Inc., USA) during the melt electrospinning process with a 5 cm working distance between the nozzle and the aluminum foil collector. The PCL granules were fed into melting chamber and then heated to a desired temperature (80 ˚C). The zero shear rate viscosity (291.5 Pa.s) of PCL was measured using an ARES-G2 rheometer (TA Instruments, USA) at 80°C using 25mm parallel plate geometry. A wood plate covered with aluminum foil was served as the counter electrode for the collection of the mesh looped microfibers.

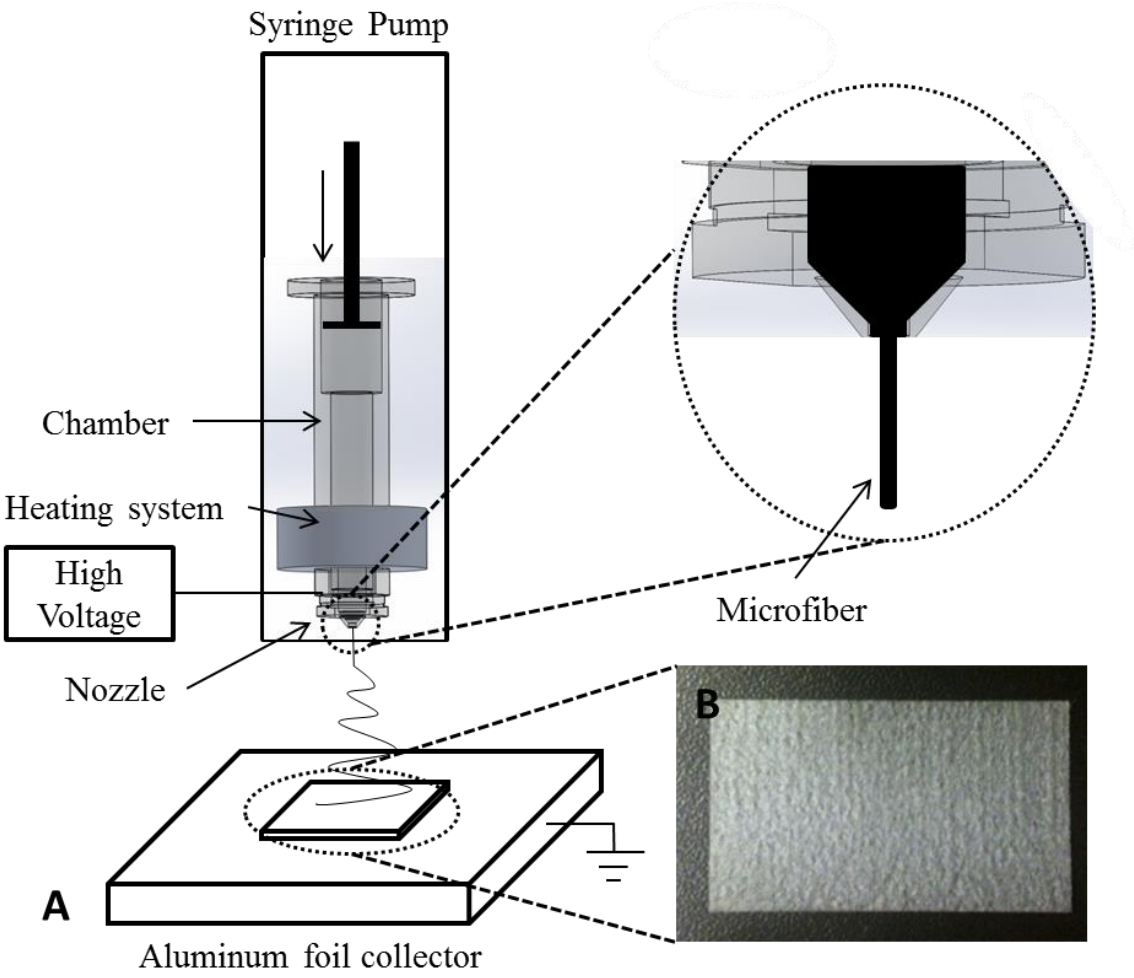

Figure 35. (A) Schematic of custom-built melt electrospinning device and (B) PCL microfiber sheet

6.2.2 Compression moulding

Custom-made aluminum 6061 moulds were machined to fabricate a solid PCL sheet as shown in Figure 36A. The thickness of the gap was set at 0.3 mm. PCL pellets were placed on lower plate. The upper plate and lower plate were then heated to 80˚C. The upper plate was subsequently pressed down onto the lower plate in order to form PCL sheets. The compressed, solid PCL sheets were detached from the mold after cooling down, as shown in Figure 36B.

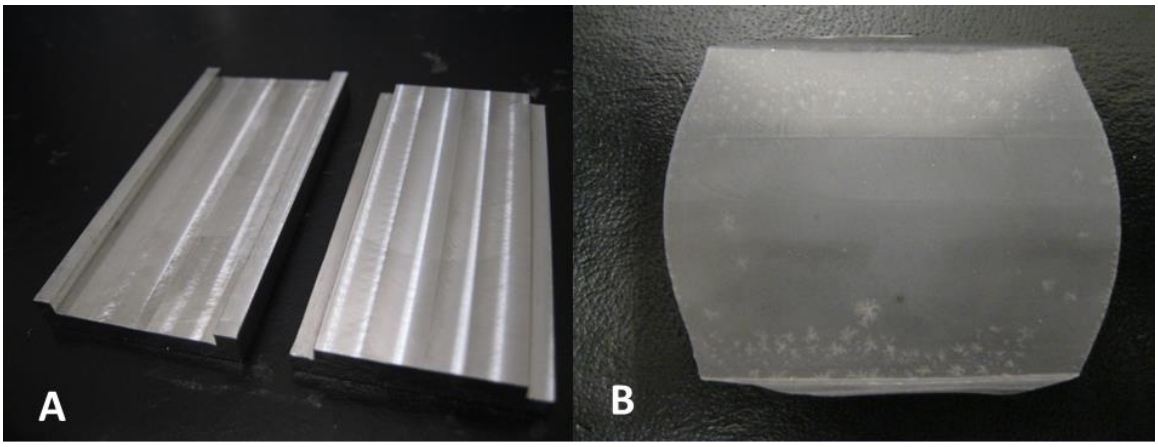

Figure 36. (A) A custom-made mold and (B) PCL sheet

6.2.3 Laser machining

A femtosecond laser-machining system was used to create auxetic materials on microfiber sheets and solid sheets as shown in Figure 37. The amplified Ti: Sapphire femtosecond laser system emitted 120fs pulse at a central wavelength of 800nm. The output power was 0.35 W as measured by a power meter, and the repetition rate was 1 kHz. The laser beam was reflected by several mirrors, and was then focused by a 20X objective lenses (Mitutoyo Co., Japan) with 0.42 numerical apertures. An electronic shutter, controlled by computer, was used to suitably turn on/off the laser beam at the desired location on the PCL solid and microfiber sheets. Figure 38 respectively demonstrates machined and non-machined surfaces in the microfiber sheets and solid sheets.

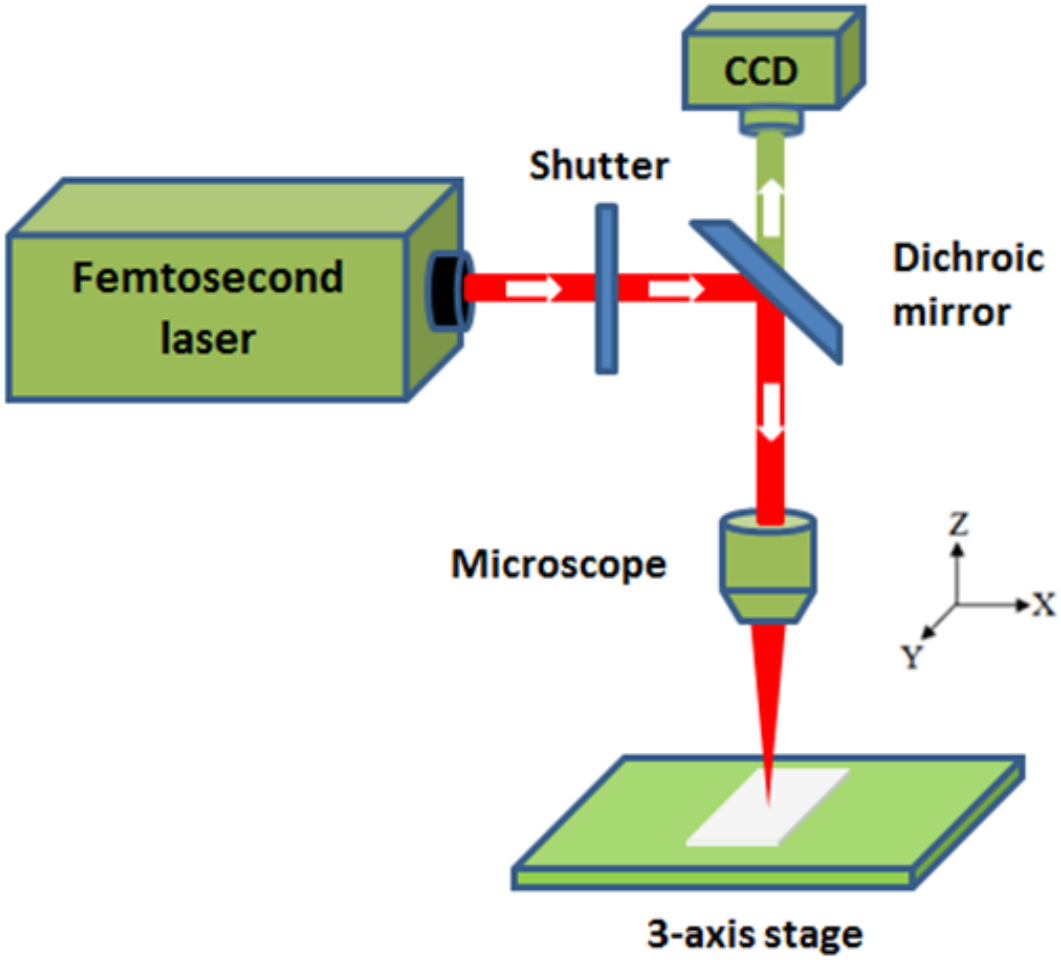

Figure 37. Schematic of femtosecond laser machining

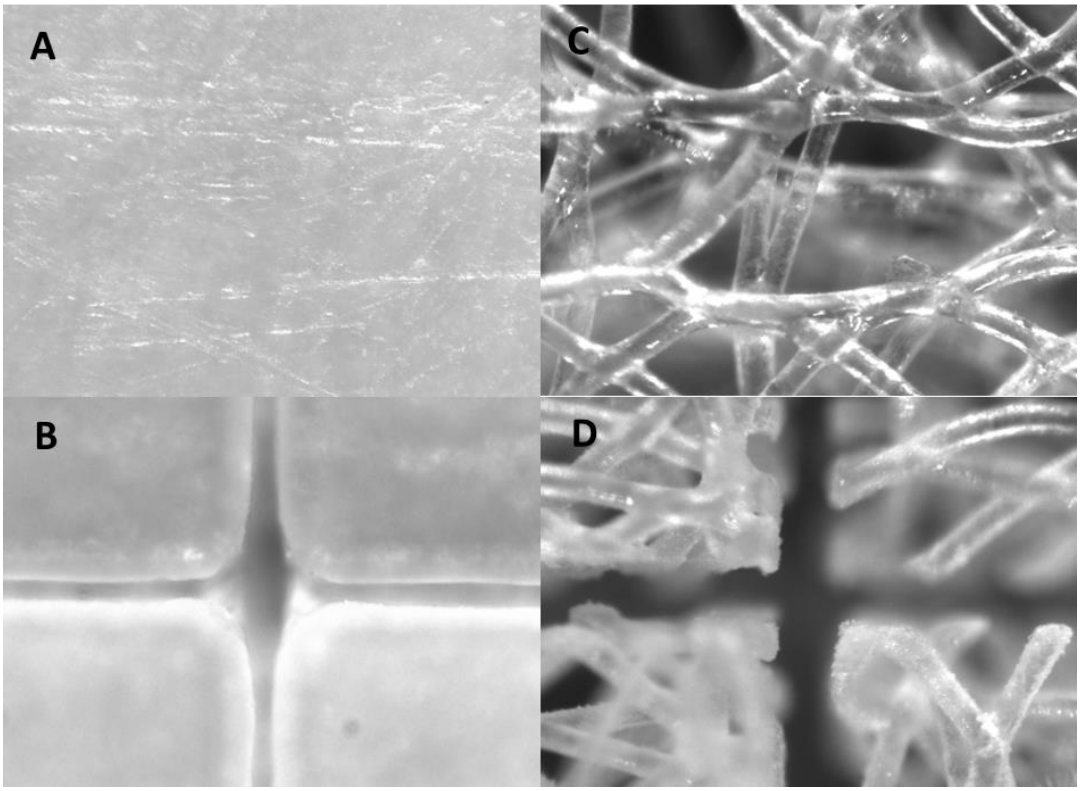

Figure 38. Microscope images: (A) Original PCL sheet, (B) Machined PCL sheet, (C) Original microfiber sheet, (D) Machined microfiber sheet

6.2.4 Gold coating

A metal sputter coater (Anatech Hummer VI) coated the PCL and PCL microfiber samples with a Gold Palladium target. The running parameters were 75 mTorr Argon and 10 mA current at 2 minutes of run time. The samples were coated with gold particles (coating thickness: 15nm, as measured by scanning electron microscopy (SEM)) to exhibit an electrical conductivity.

6.2.5 Tensile and Resistance test setup

An ALIO Vertical micro milling machine stage was used to stretch the samples at 500μm/s, as shown in Figure 39. Kistler table dynamometer (MiniDyn 9256C1) and the milling machine stage, respectively, measured tensile forces and the stretching distance

simultaneously. Resistance data was recorded by an Agilent multimeter (Agilent 34411A) in real time. Custom-made clamps held the samples on center of dynamometer. Force and resistance data were simultaneously acquired using the setup. Samples were deemed to be broken when the resistance data became unreasonably high (i.e. greater than 100MΩ).

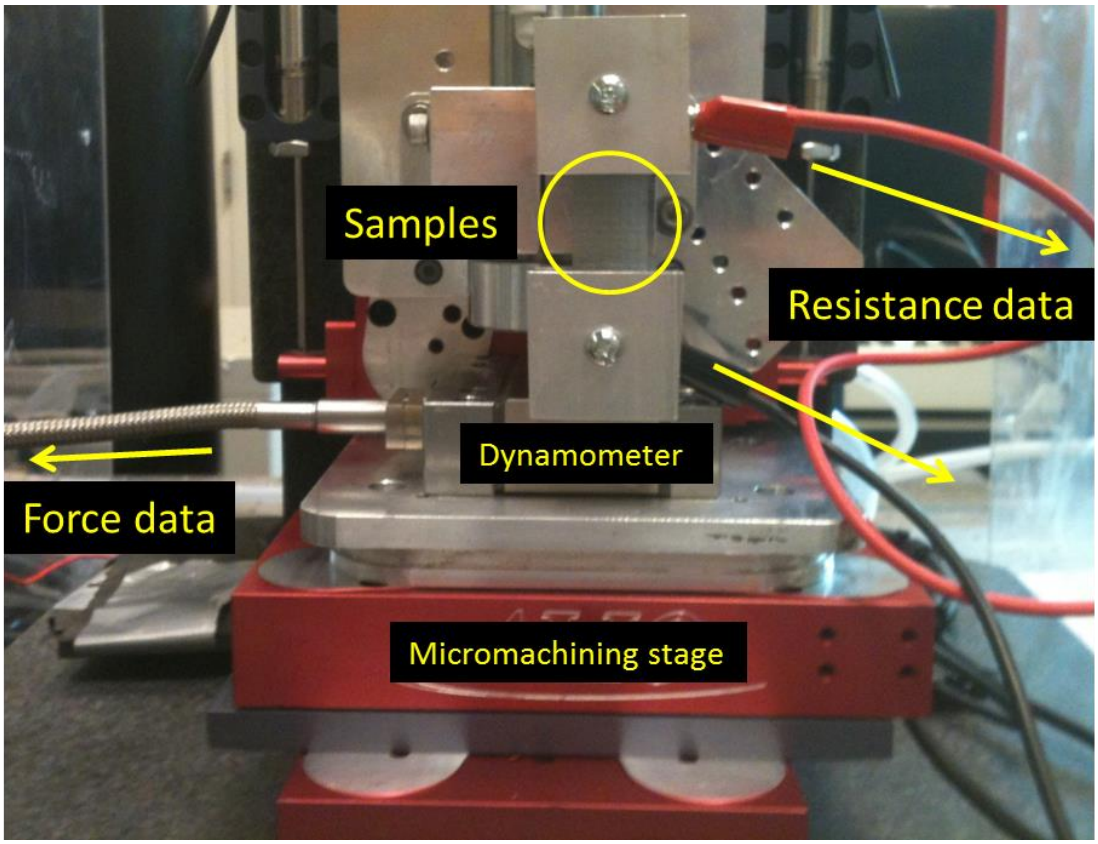

Figure 39. Setup for tensile and resistance test

6.2.6 Fabrication of auxetic sensor sheets

Auxetic materials become wider when stretched and thinner when compressed due to the stretching and rotating of their inherent square deformation mechanism, occurring when forces act on the fabricated sensors. It has been demonstrated that the same equipartition of mechanical stresses and the property of auxetic materials lead it to resume its original shape or position after being bent, stretched, or compressed.

In the process of fabrication, the samples of SS and MS (17.92 mm (width) by 32.64 mm (length) by 0.3 mm (thickness)) were fixed onto glass slides by double sided tape on a CNC 3-axis stage for machining. The machine's feed rate was fixed at 0.3 mm/s to prevent the polymer from collapsing and was repeated 3 times with a 0.1 mm depth increment with each pass. Thus, four kinds of sensor sheets (AMS, ASS, MS, and SS) were fabricated as shown in Figure 40.

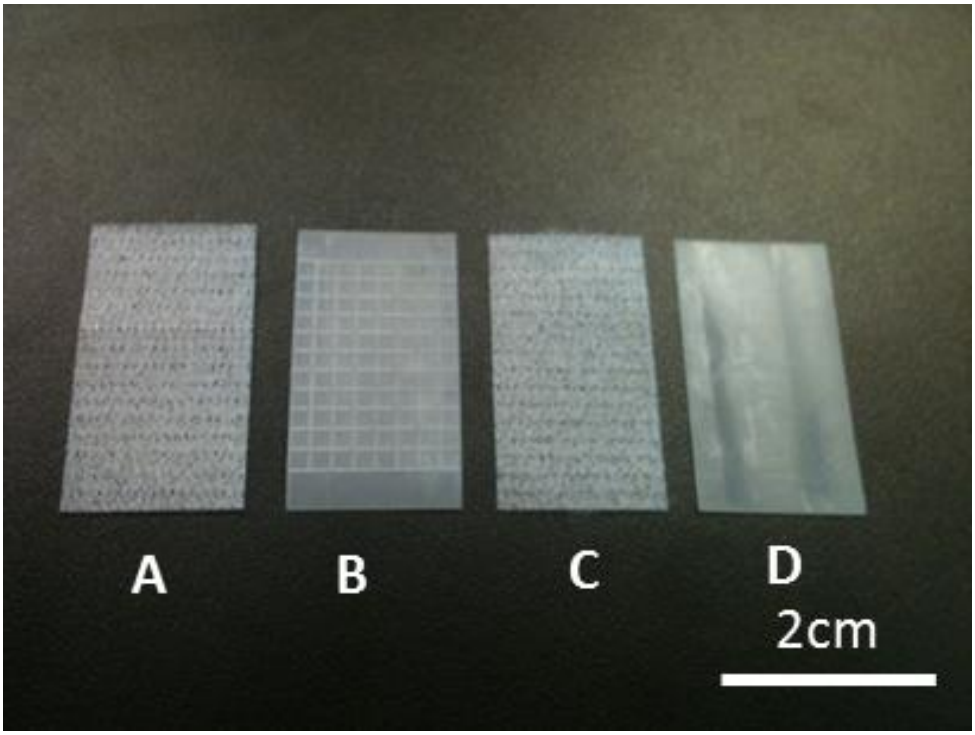

Figure 40. Machined and coated samples: (A) Auxetic Microfiber Sheet (AMS), (B) Auxetic Solid Sheet (ASS), (C) Microfiber Sheet (MS) and (D) Solid Sheet (SS)

6.3 Experimental results

6.3.1 Tensile test on the stage

All four sensors- including auxetic microfiber sheet (AMS), auxetic solid sheet (ASS), microfibers sheet (MS), and solid sheet (SS) samples- were characterized mechanically.

The force was measured with respect to the displacement and force-displacement curves, which are shown in Figure 41. The maximum displacements of AMS and MS were shown to be 3.71 mm and 0.99 mm, respectively, while ASS and SS demonstrated 1.7mm and 0.57mm, respectively. The maximum breaking force of AMS and MS respectively showed 0.25N and 5N while ASS and SS respectively demonstrated 3N and 10N. Figure 42 shows the averaged force test (auxetic samples n=6, non-auxetic samples n=3) (where n is number of test samples). The slopes of force and displacement in average terms are respectively 0.13 N/mm, 1.52 N/mm, 5.82 N/mm, and 15.39 N/mm for AMS, ASS, MS and SS. Therefore, AMS and SS have the lowest and highest tensile strength in four samples, respectively.

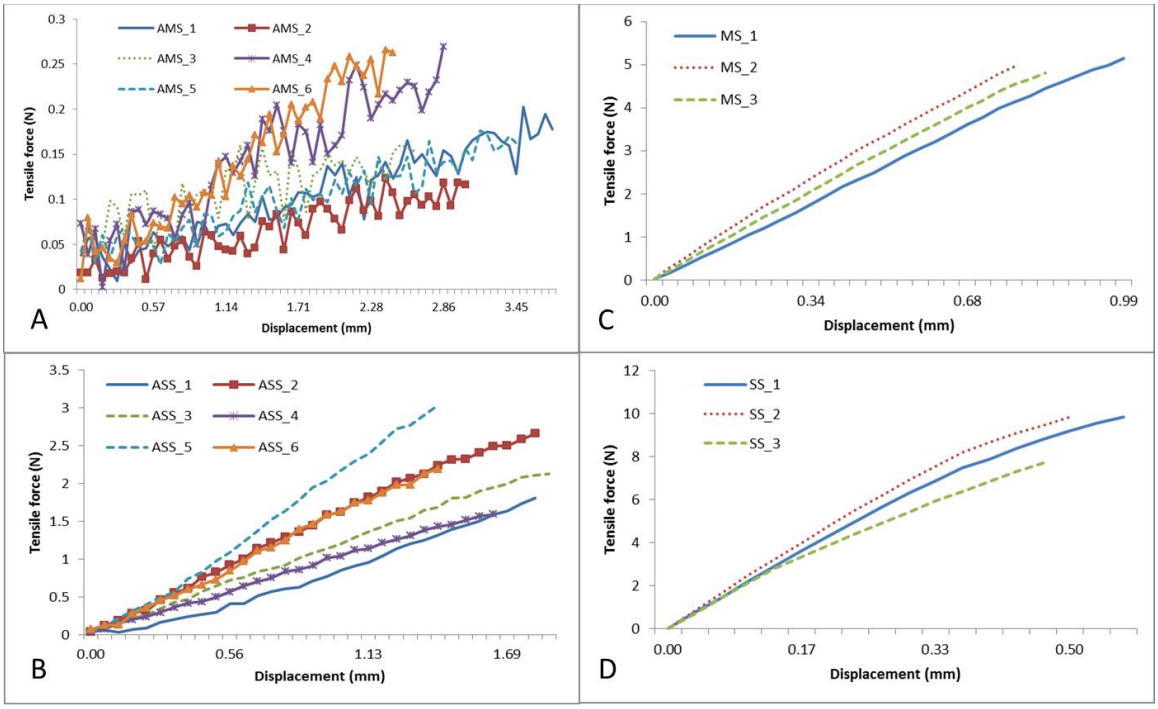

Figure 41. Results of force test (Machined samples: n=6, No machined samples: n=3)

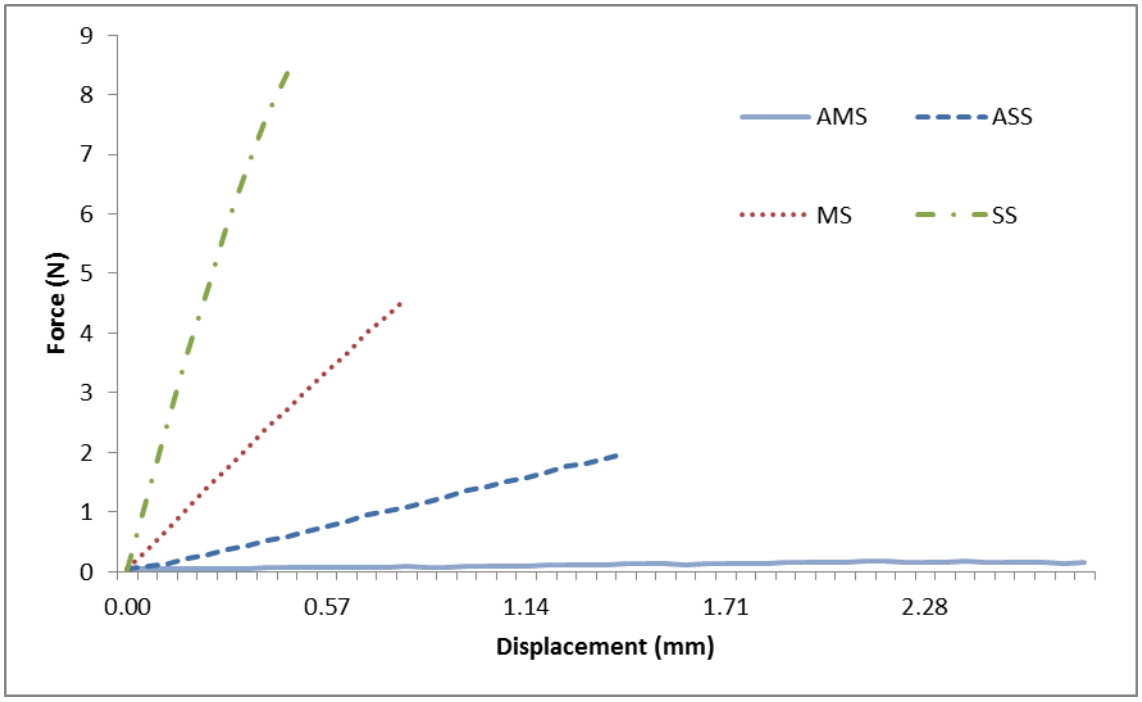

Figure 42. Average of force test (Machined samples n=6, No machined samples n=3)

6.3.2 Resistance test on the stage

Resistance vs. displacement for all four various force sensors including AMS, MS, ASS, and SS are shown in Figure 43. Figure 43A and C illustrate the change in resistance when displacement is applied for AMS and MS. The samples respectively showed a significant increase from approximately 2,000 Ω up to 17,000 Ω and 10,000 Ω in resistance when the displacement was increased from up to 2.28 mm and 0.89 mm. Figure 43B and D illustrate the effect of displacement on resistance for ASS and SS. Figure 44 shows the averaged values of the resistance tests (auxetic samples n=6, non- auxetic samples n=3). The slopes of resistance and displacement in average terms are respectively 1973.7 Ω/mm, 1925.3 Ω/mm, 1988.4 Ω/mm, and 2101.7 Ω/mm for AMS, ASS, MS, and SS. The four sensors demonstrate results of a similar magnitude regardless of the type.

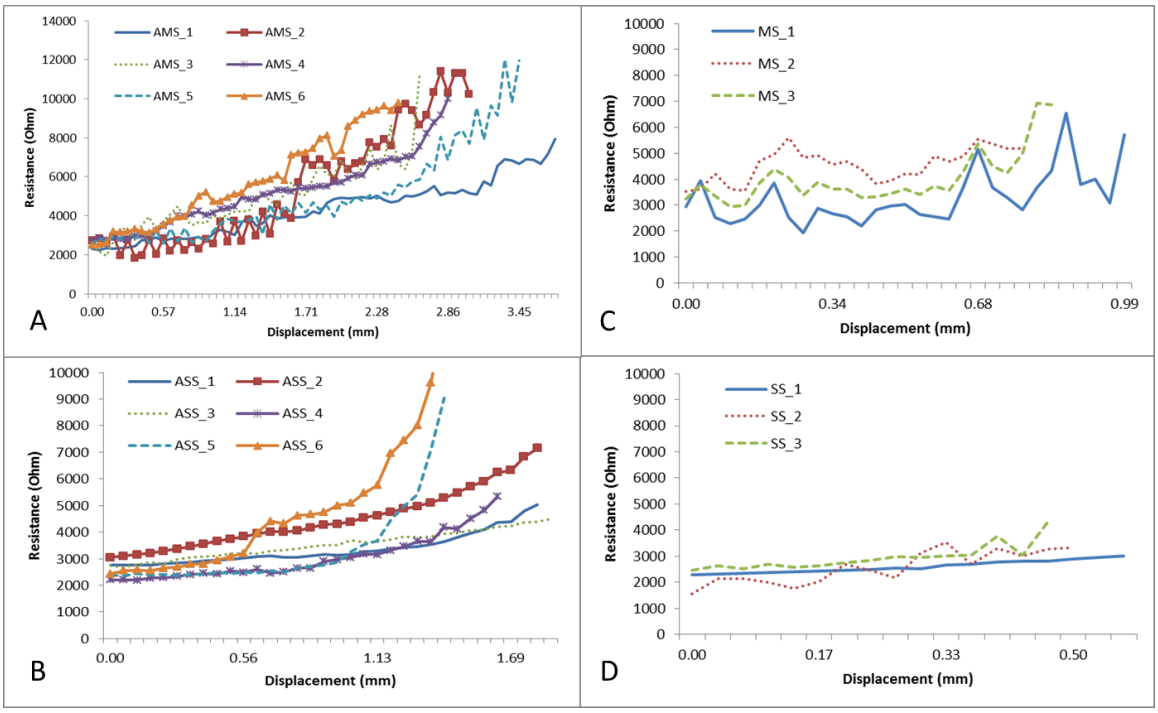

Figure 43. Results of resistance test (Machined samples: n=6, No machined samples: n=3)

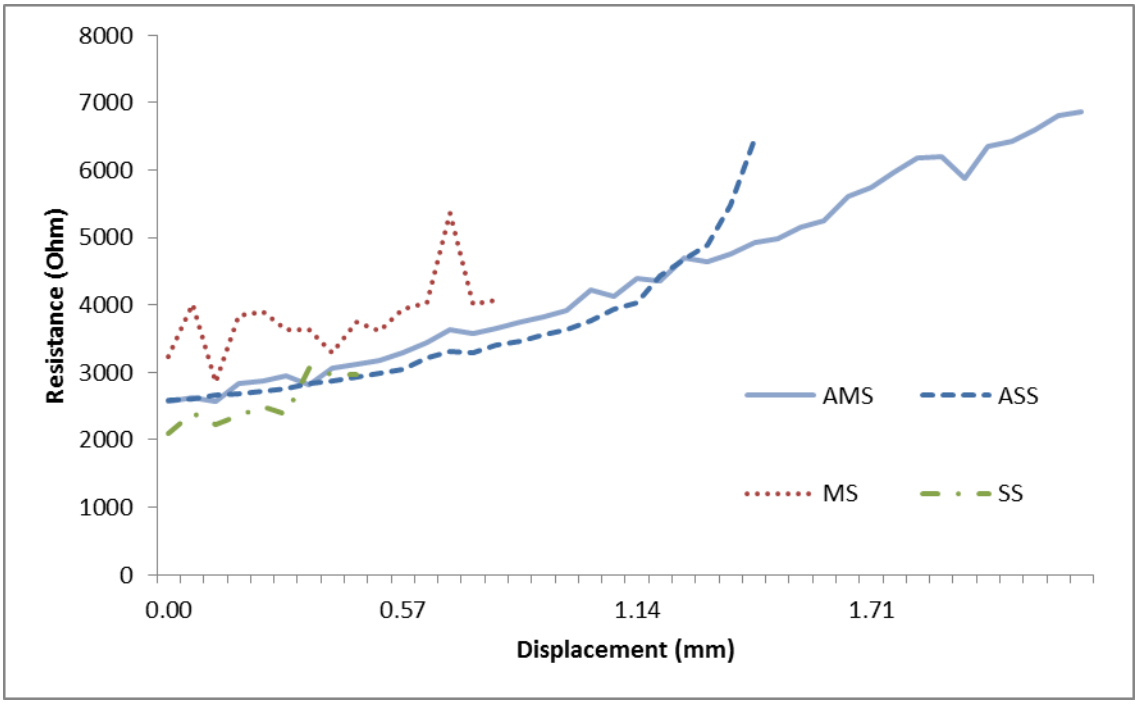

Figure 44. Average of resistance test (Machined samples: n=6, No machined samples: n=3)

6.3.3 Force & Resistance test on the stage

Results of applied force and measured resistance for all sets of force sensors -including AMS, ASS, MS, and SS samples- have been provided and the results are reported in Figure 45 (Figure 45B is enlarged from Figure 45A). All four samples may be electrically disconnected but mechanically connected; for example, the AMS sample was mechanically disconnected in displacement at 2.74 mm but the sample was electrically disconnected in 2.28 mm. In order to match the displacement between the mechanical and electrical results, we assumed all samples are electrically and mechanically disconnected when the samples show electrical disconnection. AMS sample shows a significant increase in resistance as shown in Figure 45 as the sample can be stretched with a small tensile force. It can be easily stretched using a small tensile force as it is auxetic in nature and uses PCL as the material making up the microfibers. The sensitivity of AMS is 14448.15 Ω/N. ASS presents a linear behavior between 0 and 1.8 N but shows an exponential curve after 1.8N. The sensitivity of ASS is 409.04 Ω/N. MS and SS are not auxetic (i.e., non-machined) so they require much more force than AMS and ASS in order to be stretched. MS shows wide fluctuation at a constant tensile force since gold particles could be moved among the microfibers due to viscoelastic nature of the fibers; however, it shows an overall resistance increase. The sensitivity of MS is 195.35 Ω/N. Of all samples presented, SS is the toughest sample to stretch as shown in Figure 41D. The variance of resistance is less than 1000 Ω because the sample is stretched within 0.5 mm. The sensitivity of SS is 175.62 Ω/N.

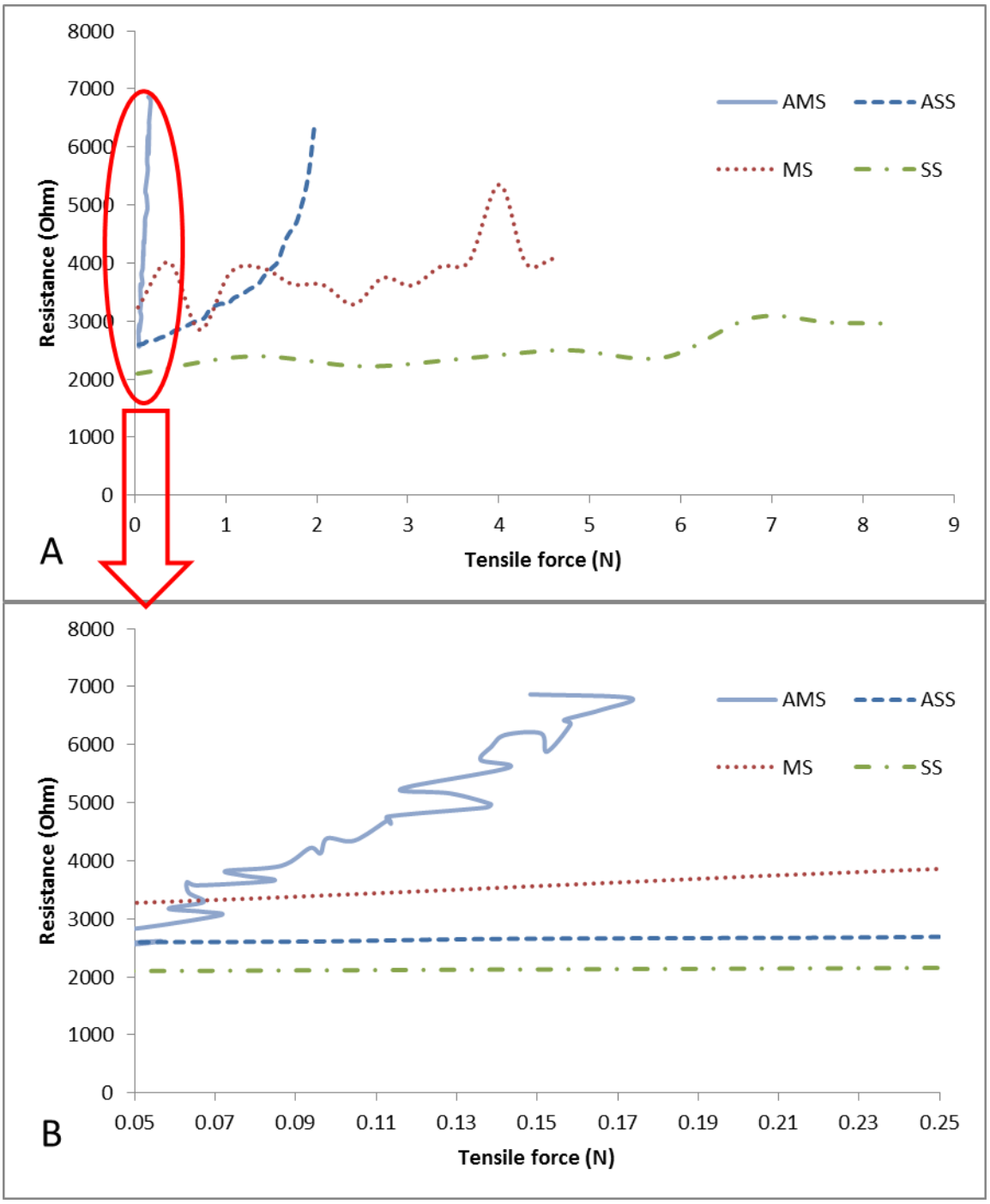

Figure 45. Results of Force & Resistance test

6.3.4 Resistance test on human skin

The resistance tests of ASS and AMS sensors were conducted on human skin. The sensors (ASS, AMS) were attached on the wrist of volunteer. The wrist was flexed from a

neutral position (0˚) to maximum bending position (70˚) - which is approximately 1.5mm in displacement - and subsequently returned to an initial position, with results shown in Figure 46. Figure 47A and B present results of the resistance test on the wrist skin for ASS and AMS, respectively. While ASS is increased from 2400 Ω to 4800 Ω, AMS is increased from 2500 Ω to 5500 Ω. Therefore, AMS was more sensitive than ASS with respect to displacement. Moreover, AMS demonstrated a more linear increase and decrease in resistance than ASS.

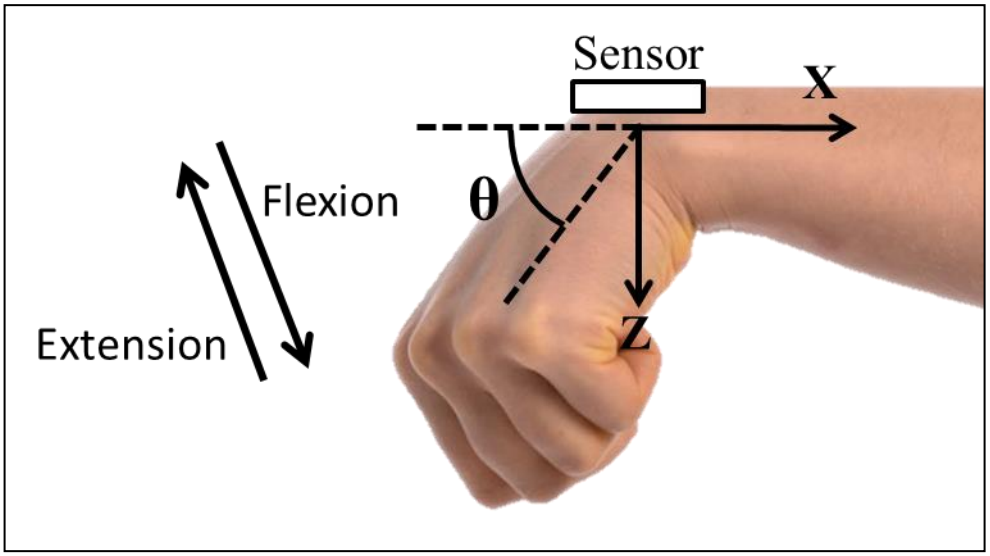

Figure 46. Schematic of motion for resistance test on human skin

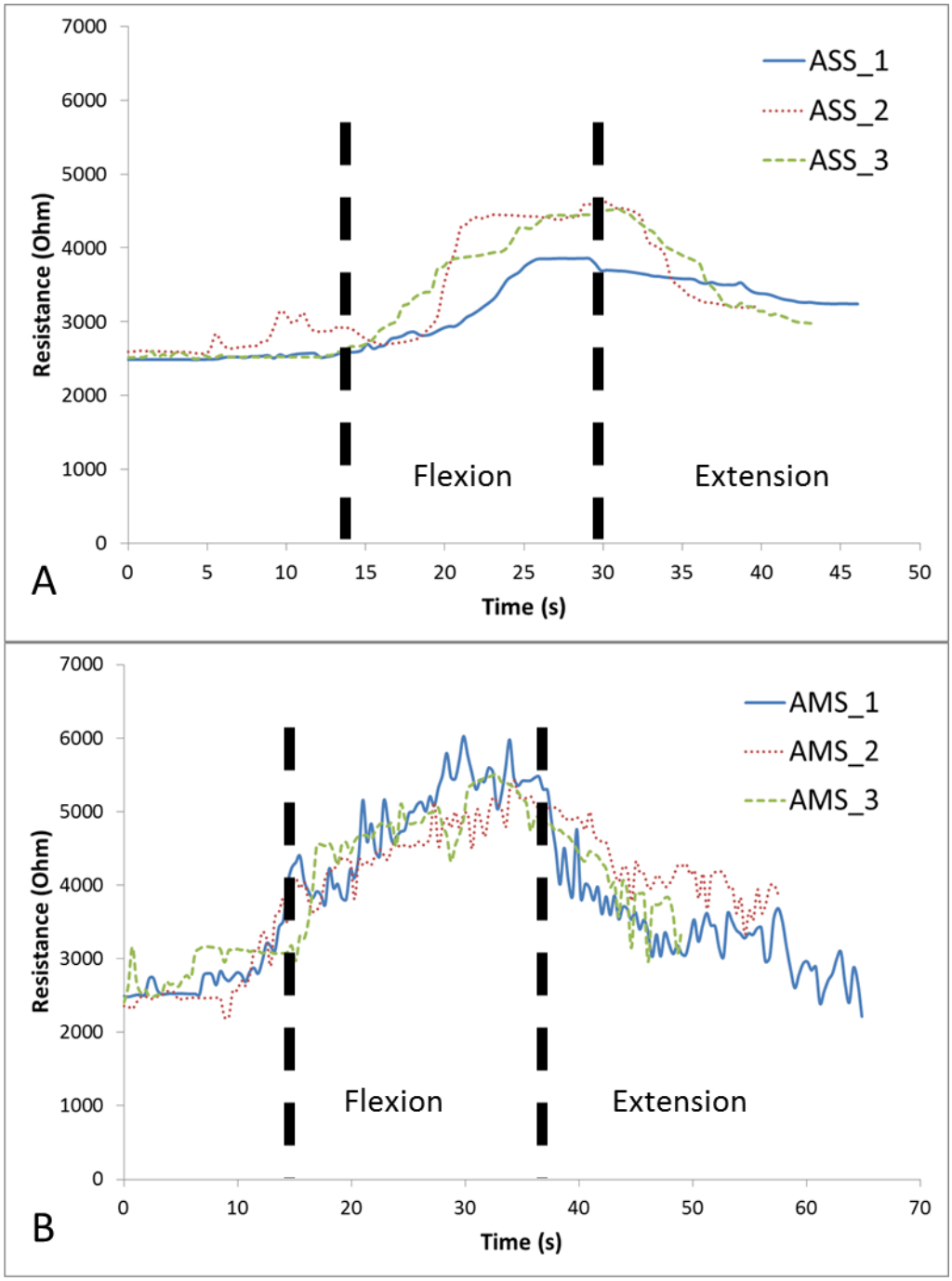

Figure 47. Results of resistance test on wrist skin (n=3)

6.4 Conclusion

In this study, the fabrication and characterization of PCL based stretchable force sensors were investigated using a melt electrospinning technique and rehabilitation applications.

We were able to successfully fabricate and characterize the mechanical and electrical properties of the novel force sensors, being AMS, ASS, MS and SS. We also successfully demonstrated the effects of applying force and displacement on the measured resistance of the sensors fabricated based on auxetic geometry via the combination of laser micromachining and melt electrospinning techniques. The sensitivities of such sensors were reported as 14448.15 Ω/N, 409.04 Ω/N, 195.35 Ω/N, and 175.62 Ω/N for AMS, ASS, MS, and SS, respectively. The AMS sensor showed the highest measurement sensitivity. Moreover, the AMS sensor demonstrated a more sensitive and linear in flexion and extension than ASS regarding displacement on human skin, as was expected.

Chapter 7. Conclusion and Future Work

7.1 Conclusion

- It has been shown that electrospun microfibers can be made from custom-made chamber, custom-made plunger, custom-made fixture of syringe pump, custom-made collecting drum, and custom-made nozzles that could be interchanged.
- It has been shown that fiber diameter can be controlled from 0.012mm to 0.220mm with various nozzle sizes, applied voltage, and distance between nozzle and counter electrode.
- The theoretical porosity of fibrous scaffolds fabricated by melt electrospinning incorporating various nozzle sizes and their yield strength results including Young's modulus and strain at break has been demonstrated.
- It has been confirmed by seeding neural progenitors derived from murine R1 embryonic stem cell lines that the fabricated fibrous scaffolds enable to survive, migrate, and differentiate into neurons.
- It has been shown that two reliable mathematical models are established in order to understand the parameters that determine the topography of scaffolds, which are melt electrospinning process model and accumulation model of the electrospun microfibers on flat and round surfaces. These models have been validated through the use of experimentally obtained data.

- It has been shown that topographical features of micro fibrous scaffolds could be predicted by the mathematical models and the models holds great promise for the fabrication of scaffold specifically for tissue engineering applications.
- It has been shown that the extended models replace parts that depend only experimental data with physical equations such as temperature effect, radius of helix, tension force on microfibers, and overlapped force in topology. The extended models have been confirmed more accurate by experiments.
- It has been shown that combination of melt electrospinning and particular leaching techniques can produce porous microfibers without any impacts and the porous rate on electrospun microfibers can be controlled by concentration of additives.
- It has been shown melt electrospinning is capable to fabricate four types of auxetic stretchable force sensors for hand rehabilitation, which are AMS (Auxetic Microfiber Sheet), ASS (Auxetic Solid Sheet), MS (Microfiber Sheet), and SS (Solid Sheet).
- We have successfully studied the effects of applied force and displacement on the measured resistance of the force sensors fabricated based on auxetic geometry via the combination of micromachining and melt electrospinnning techniques. Moreover, we have verified the desired sensors working practically on real human hand.

7.2 Future work

- Our customized nozzles are interchangeable since the melt chamber and nozzles have been mechanically connected using inside and outside threads. The threads in nozzle and chamber could not be perfectly sealed so they have been damaged when nozzles were changed. It is necessary to redesign the thread to the outside of chamber.

- In terms of mathematical modeling, the current models enable to predict results only in uniform electric and magnetic fields since the models are based on the related forces, not electric and magnetic fields. Thus, the current models are necessary to be developed in basis of the field form for predicting electrospun microfibers properties in various geometry setups.
- The current melt electrospinning technique enables efficiently to fabricate the desired microfibers but it is difficult to change structures of microfibers. I believe that coaxial melt electrospinning technique has an ability to solve the problem. Moreover, the coaxial melt electrospinning enables to fabricate mechanically stronger microfibers and hollow microfibers for more various applications.

Publications

1 Conference papers (19)

- **Junghyuk Ko**, Nima K. Mohtaram, Stephanie M. Willerth, and Martin B.G. Jun, Electrospinning of Nonaligned and Aligned Polycaprolactone Fibers For Tissue Engineering, 7th International Conference on Micro Manufacturing (ICOMM) 2012, Northwestern University, IL, USA

- Nima Khadem Mohtaram, **Junghyuk Ko**, Darcy Ippolito, Martin B.G. Jun, Stephanie M. Willerth, Development of Micro and Nano-structured Neural Tissue Engineering Scaffolds, 2012, The 16th Anuunal Meeting of the Pacific Centre for Advanced Materials and Microstructures (PCAMM), poster.

- Nima K. Mohtaram, Amy Montgomery, **Junghyuk Ko**, Michael Carlson, Marting B.G. Jun, and Stephanie M. Willerth, Multifuntional Electrospun Scaffolds for Promoting Neural Differentiation of Embryonic and Induced Pluripotent Stem Cells, 2012, BCStem Cells and Regenerative Medicine Initiative Retreat, Vancouver, BC, Canada

- Nima Khadem Mohtaram, **Junghyuk Ko**, Amy Montgomery, Kathleen Kolehmainen, Stephanie Morison, Martin Byung-Guk Jun, Stephanie M. Willerth, Using electrospun poly(ε-caprolactone) nanofibers to promote the differentiation of induced pluripotent stem cells into neural phenotypes, 2012, International Society for Stem Cell Research (ISSCR), 2012, Seattle, WA, USA.

- Mohtaram, NK; **Ko, J**; Montgomery, A; Gomez, JC; Wong, A; Agbay, A; King, C; Robinson, M; Jun MBG, Willerth, SM, Fabrication and Characterization of Hybrid Biomaterial Nerve Conduits for Neural Differentiation of Induced Pluripotent Stem Cells, 2012, Canadian Biomaterials Society (CBS), Ottawa, Ontario, Canada.

- Sukhwinder Bhullar, Farid Ahmed, **Junghyuk Ko**, Martin B.G. Jun, Design and Fabrication of Stent with Negative Poisson's Ratio, 8th International Conference on Micro Manufacturing (ICOMM) 2013, University of Victoria, BC, CANADA.

- Nima K. Mohtaram, **Junghyuk Ko**, Michael Carlson, Martin B.G. Jun, Stephanie M. Willerth, Nanofabrication of Electrospun Fibers for Controlled Release of Retinoic Acid, 8th International Conference on Micro Manufacturing (ICOMM) 2013, University of Victoria, BC, CANADA.

- **Junghyuk Ko**, Nima K. Mohtaram, Patrick C.D. Lee, Stephanie M. Willerth, Martin B.G. Jun, Parametric Studies of Melt Electrospinning Poly ε (caprolactone) Fibers for Tissue Engineering Applications, 8th International

Conference on Micro Manufacturing (ICOMM) 2013, University of Victoria, BC, Canada.

- **Junghyuk Ko**, Hanbin Choi, and Martin B.G. Jun, Electrospinning: the Hybrid Methods in Achieving the Optimal Scaffolds for Cell Growth, 2013, Canada-Korea Young Generation Conference (CKYGC), Toronto, Ontario, Canada

- Jinah Jang, **Junghyuk Ko**, Dong-Woo Cho, Martin B.G. Jun and Deok-Ho Kim, Elastin-sprayed tubular scaffolds with microstructures and nanotextures for vascular tissue engineering, the American Society of Mechanical Engineers 2013 summer bioengineering conference (ASME-SBC), Oregon, Sunriver, USA.

- Nima Khadem Mohtaram, **Junghyuk Ko**, Craig Kin, Lin Su, Martin Byung-Guk Jun and Stephanie M. Willerth, Fabriation and Characterization of Hybrid Biomaterial Nerve Conduits for Neural Differentiation of Induced Pluripotent Stem Cells, Canadian Biomaterials Society (CBS), Ottawa, Ontario, Canada.

- **Junghyuk Ko**, Yonghyun Cho, Sukhwinder Bhullar, and Martin B.G. Jun, "Fabrication and Characterization of Novel Stretchable Force Sensor Using Melt Electrospinning", 2014, 9th International Conference on Micro Manufacturing (ICOMM), Nanyang Technological University, Singapore.

- Nima Khadem Mohtaram, **Junghyuk Ko**, Craig King, Amy Montgomery, Lin Sun, Rishi Vasandani, Martin Byung-Guk Jun and Stephanie M. Willerth, "Neuronal Differentiation of Human Induced Pluripotent Stem Cells seeded on Melt Electrospun Microfibers", 2014, the Canadian Medical and Biological Engineering Society (CMBEC 37), Vancouver, BC, Canada.

- Nima Khadem Mohtaram, **Junghyuk Ko**, Amy Montgomery, Michael Carlson, Lin Sun, Alix Wong, Meghan Robinson, Martin Byung-Guk Jun, Stephanie M. Willerth, "Encapsulated Nanofiber Scaffolds for Neuronal Differentiation of Induced Pluripotent Stem Cells: A Promising Strategy for Spinal Cord Injury", 2014, International Collaboration On Repair Discoveries (ICORD), Vancouver, BC, Canada.

- Nima Khadem Mohtaram, **Junghyuk Ko**, Nathan Muller, Lin Su, Martin Byung-Guk Jun and Stephanie M. Willerth, Melt Electrospun Microfiber Scaffolds with Novel Architecture for Neuronal Differenentiation of Human Induced Pluripotent Stem Cells, 2014, Canadian Biomaterials Society (CBS), Halifax, Nova Scotia, Canada

- **Junghyuk Ko** and Martin B.G. Jun, 3D modeling of melt electrospinning process, 2014, 3rd International Conference on Electrospinning, San Francisco, California, USA.

- **Junghyuk Ko**, Seungwon Jun, Martin B.G. Jun, 3D mathematical modeling and fabrication of tubular scaffolds for vascular tissue engineering using melt electrospinning, 2014, International Conference on Biofabrication, Pohang, Korea.

- **Junghyuk Ko**, Jason K. Lee, Martin B.G. Jun, Production and Characterization of Coaxial Microfibers with Different Molecular Weight Using Coaxial Melt Electrospinning Technique, 2015, submitted to 10th International Conference on Micro Manufacturing (ICOMM).

- Jason K. Lee, **Junghyuk Ko**, Patrick C. Lee, Martin B.G. Jun, Melt electrospun coaxial microfiber processing and properties, 2015, submitted to 31st International conference of the polymer processing society.

2 Journal papers (12)

- **Junghyuk Ko**, Kathleen Kolehmainen, Farid Ahmed, Martin B.G. Jun, Stephanie M. Willerth, 2012, Towards high throughput tissue engineering: development of chitosan-calcium phosphate scaffolds for engineering bone tissue from embryonic stem cell, Am J Stem Cell, Vol.1(1), pp 81-89.

- **Junghyuk Ko**, Nima Khadem Mohtaram, Farid Ahmed, Amy Montgomery, Michael Carlson, Patrick C.D. Lee, Stephanie M. Willerth, Martin B.G. Jun, Fabrication of poly (ε-caprolactone) microfibers scaffolds with varying topography and mechanical properties for stem cell-based tissue engineering application, 2014, Journal of Biomaterials Science Polymer Edition, **25**(1), p. 1-17.

- Sukhwinder Bhullar, **Junghyuk Ko**, Farid Ahmed and Martin Byung-Guk Jun, Design and fabrication of stent with negative Poisson's ratio, 2014, International Journal of Mechanical, Industrial Science and Engineering, **8**(2), p. 2538-2544

- **Junghyuk Ko**, Sukhwinder Bhullar, Nima Khadem Mohtaram, Stephanie M. Willerth, and Martin B.G. Jun, Controlling Topographical Properties of Poly (ε-caprolactone) Melt Electrospun Scaffolds through Mathematical Modeling, 2014, Journal of Micromechanics and Microengineering, 24(6), doi:10.1088/0960-1317/24/6/065009

- **Junghyuk Ko**, Dayun Kan, and Martin B.G. Jun, "Enhanced cell attachments on scaffolds using melt electrospinning and particular leaching for tissue engineering applications", 2014, submitted to Manufacturing letter.

- Sukhwinder Bhullar, **Junghyuk Ko**, Yonghyun Cho, and Martin B.G. Jun, "Development of an Auxetic Biodegradable Non-Woven Polymer Stent", 2014, submitted to Mechanics of Materials.

- Nima Khadem Mohtaram, **Junghyuk Ko**, Amy Montgomery, Michael Carlson, Lin Sun, Alix Wong, Meghan Robinson, Martin Byung-Guk Jun, and Stephanie M. Willerth, Multifuntional Electrospun Scaffolds for Promoting Neuronal Differentiation of Induced Pluripotent Stem Cells, 2014, Journal of Biomaterials and Tissue Engineering, 14-184-R.

- Nima Khadem Mohtaram, **Junghyuk Ko**, Craig King, Lin Su, Nathan Muller, Martin Byung-Guk Jun and Stephanie M. Willerth, Electrospun biomaterial scaffolds with varied topographies for neuronal differentiation of human induced pluripotent stem cells, 2014, Journal of Biomedical Materials Research, JBMR-A-14-0924.

- **Junghyuk Ko**, Sukhwinder Bhullar, Yonghyun Cho, Martin Byung-Guk Jun, Design and Fabrication of Auxetic Stretchable Force Sensor for Hand Rehabilitation, 2014, submitted to Journal of Sensors and Actuator A

- Nima Khadem Mohtaram**, Junghyuk Ko,** Andrew Agbay, David Rattray, Paul O'Neill, Azra Rajwani, Rishi Vasandani, Hien Luong Thu, Marting Byung-Guk Jun and Stenphanie M. Willerth, Controlled Release of Glial cell-derived Neurotrophic Factor from Aligned Electrospun Nanofibers, 2014, submitted to Journal of Controlled Release.

- **Junghyuk Ko**, Nima Khadem Mohtaram, Patrick C.D. Lee, Stephanie M. Willerth, and Martin B.G. Jun, Mathematical model for predicting topographical properties of poly (ε-caprolactone) melt electrospun scaffolds in various temperature and linear transitional speed, 2014, submitted to Journal of Micromechanics and Microengineering.

- **Junghyuk Ko**, Seungwon Tim Jun, Jason Keonhag Lee, and Martin B.G. Jun, Effects of varying molecular weight with increasing temperature on poly (ε-caprolactone) melt electrospun fiber diameter, 2014, submitted to Journal of Polymer Engineering and Science.

References

1. Willerth, S.M. and S.E. Sakiyama-Elbert, *Approaches to neural tissue engineering using scaffolds for drug delivery.* Advanced Drug Delivery Reviews, 2007. **59**(4-5): p. 325-338.
2. Pfister, B.J., et al., *Biomedical engineering strategies for peripheral nerve repair: surgical applications, state of the art, and future challenges.* Crit Rev Biomed Eng, 2011. **39**(2): p. 81-124.
3. Abranches, E., et al., *Neural Differentiation of Embryonic Stem Cells In Vitro: A Road Map to Neurogenesis in the Embryo.* Plos One, 2009. **4**(7).
4. Robertson, M.J., P. Gip, and D.V. Schaffer, *Neural stem cell engineering: directed differentiation of adult and embryonic stem cells into neurons.* Frontiers in Bioscience-Landmark, 2008. **13**: p. 21-50.
5. Saha, K., et al., *Substrate Modulus Directs Neural Stem Cell Behavior.* Biophysical Journal, 2008. **95**(9): p. 4426-4438.
6. Krencik, R. and S.C. Zhang, *Stem cell neural differentiation: a model for chemical biology.* Current Opinion in Chemical Biology, 2006. **10**(6): p. 592-597.
7. Owen, S.C. and M.S. Shoichet, *Design of three-dimensional biomimetic scaffolds.* Journal of Biomedical Materials Research Part A, 2010. **94A**(4): p. 1321-1331.
8. Griffith, L.G. and M.A. Swartz, *Capturing complex 3D tissue physiology in vitro.* Nature Reviews Molecular Cell Biology, 2006. **7**(3): p. 211-224.
9. Antonios G, M.J., *Formation of highly porous biodegradable scaffolds for tissue engineering. Electronic Journal of Biotechnology.* Electronic Journal of Biotechnology, 2000. **3**(2).
10. Hollister, S.J., *Porous scaffold design for tissue engineering.* Nature Materials, 2005. **4**(7): p. 518-524.
11. Supaphol, P., et al., *Electrospinning of Biocompatible Polymers and Their Potentials in Biomedical Applications.* Biomedical Applications of Polymeric Nanofibers, 2012. **246**: p. 213-239.
12. Liao, S., et al., *Biomimetic electrospun nanofibers for tissue regeneration.* Biomedical Materials, 2006. **1**(3): p. R45-R53.
13. Li, D. and Y.N. Xia, *Electrospinning of nanofibers: Reinventing the wheel?* Advanced Materials, 2004. **16**(14): p. 1151-1170.
14. Bhardwaj, N. and S.C. Kundu, *Electrospinning: A fascinating fiber fabrication technique.* Biotechnology Advances, 2010. **28**(3): p. 325-347.
15. Brown TD, S.A., Thibaudeau L, Taubenberger A, Loessner D, Vaquette C, *Design and fabrication of tubular scaffolds via direct writing in a melt electrospinning mode.* Biointerphases, 2012. **7(1-4)**: p. 13.
16. Dalton, P.D., et al., *Direct in vitro electrospinning with polymer melts.* Biomacromolecules, 2006. **7**(3): p. 686-690.
17. H, Z., *Electrospun fibers from both solution and melt: processing, structure and property.* Cornell University, 2007.
18. Larrondo, L. and R.S.J. Manley, *Electrostatic Fiber Spinning from Polymer Melts .1. Experimental-Observations on Fiber Formation and Properties.* Journal of Polymer Science Part B-Polymer Physics, 1981. **19**(6): p. 909-920.

19. Larrondo, L. and R.S.J. Manley, *Electrostatic Fiber Spinning from Polymer Melts .2. Examination of the Flow Field in an Electrically Driven Jet.* Journal of Polymer Science Part B-Polymer Physics, 1981. **19**(6): p. 921-932.
20. Larrondo, L. and R.S.J. Manley, *Electrostatic Fiber Spinning from Polymer Melts .3. Electrostatic Deformation of a Pendant Drop of Polymer Melt.* Journal of Polymer Science Part B-Polymer Physics, 1981. **19**(6): p. 933-940.
21. Lyons, J., C. Li, and F. Ko, *Melt-electrospinning part I: processing parameters and geometric properties.* Polymer, 2004. **45**(22): p. 7597-7603.
22. Griffith, L.G. and G. Naughton, *Tissue engineering--current challenges and expanding opportunities.* Science, 2002. **295**(5557): p. 1009-14.
23. Langer, R. and J.P. Vacanti, *Tissue engineering.* Science, 1993. **260**(5110): p. 920-6.
24. Davis, M.W. and J.P. Vacanti, *Toward development of an implantable tissue engineered liver.* Biomaterials, 1996. **17**(3): p. 365-372.
25. Hutmacher, D.W., *Scaffolds in tissue engineering bone and cartilage.* Biomaterials, 2000. **21**(24): p. 2529-2543.
26. Ko, J., Kolehmainen, K., Ahmed, F., Jun, M. B-G. and Willerth, SM., *Towards high throughput tissue engineering: development of chitosan-calcium phosphate scaffolds for engineering bone tissue from embryonic stem cells* American Journal of Stem Cells, 2012. **1**(1): p. 81-89.
27. Kolehmainen, K. and S.M. Willerth, *Preparation of 3D fibrin scaffolds for stem cell culture applications.* Journal of visualized experiments : JoVE, 2012(61): p. e3641.
28. MacNeil, S., *Progress and opportunities for tissue-engineered skin.* Nature, 2007. **445**(7130): p. 874-880.
29. Willerth, S.M., *Neural tissue engineering using embryonic and induced pluripotent stem cells.* Stem Cell Research & Therapy, 2011. **2**(2): p. 17.
30. Xie, J.W., et al., *The differentiation of embryonic stem cells seeded on electrospun nanofibers into neural lineages.* Biomaterials, 2009. **30**(3): p. 354-362.
31. Martino, S., et al., *Stem cell-biomaterial interactions for regenerative medicine.* Biotechnology Advances, 2012. **30**(1): p. 338-351.
32. Willerth, S.M. and S.E. Sakiyama-Elbert, *Combining stem cells and biomaterial scaffolds for constructing tissues and cell delivery*, in *StemBook*2008: Cambridge (MA).
33. Nam, Y.S., J.J. Yoon, and T.G. Park, *A novel fabrication method of macroporous biodegradable polymer scaffolds using gas foaming salt as a porogen additive.* Journal of Biomedical Materials Research, 2000. **53**(1): p. 1-7.
34. Oh, S.H., et al., *Fabrication and characterization of hydrophilic poly(lactic-co-glycolic acid)/poly(vinyl alcohol) blend cell scaffolds by melt-molding particulate-leaching method.* Biomaterials, 2003. **24**(22): p. 4011-4021.
35. Pinto, A.R., et al., *Behaviour of human bone marrow mesenchymal stem cells seeded on fiber bonding chitosan polyester based for bone tissue engineering scaffolds.* Tissue Engineering, 2006. **12**(4): p. 1019-1019.
36. Suh, S.W., et al., *Effect of different particles on cell proliferation in polymer scaffolds using a solvent-casting and particulate leaching technique.* Asaio Journal, 2002. **48**(5): p. 460-464.

37. Yoshimoto, H., et al., *A biodegradable nanofiber scaffold by electrospinning and its potential for bone tissue engineering.* Biomaterials, 2003. **24**(12): p. 2077-2082.
38. Xie, J.W., et al., *Radially Aligned, Electrospun Nanofibers as Dural Substitutes for Wound Closure and Tissue Regeneration Applications.* Acs Nano, 2010. **4**(9): p. 5027-5036.
39. Xie, J.W., et al., *Electrospun nanofibers for neural tissue engineering.* Nanoscale, 2010. **2**(1): p. 35-44.
40. Pham, Q.P., U. Sharma, and A.G. Mikos, *Electrospinning of polymeric nanofibers for tissue engineering applications: A review.* Tissue Engineering, 2006. **12**(5): p. 1197-1211.
41. Reneker, D.H., et al., *Bending instability of electrically charged liquid jets of polymer solutions in electrospinning.* Journal of Applied Physics, 2000. **87**(9): p. 4531-4547.
42. Reneker, D.H., et al., *Electrospinning of nanofibers from polymer solutions and melts.* Advances in Applied Mechanics, Vol 41, 2007. **41**: p. 43-195.
43. Mohtaram, N.K., A. Montgomery, and S.M. Willerth, *Biomaterial-based drug delivery systems for the controlled release of neurotrophic factors.* Biomedical materials, 2013. **8**(2): p. 022001.
44. Dalton, P.D., et al., *Electrospinning of polymer melts: Phenomenological observations.* Polymer, 2007. **48**(23): p. 6823-6833.
45. Park, S.H., et al., *Development of dual scale scaffolds via direct polymer melt deposition and electrospinning for applications in tissue regeneration.* Acta Biomaterialia, 2008. **4**(5): p. 1198-1207.
46. Pedicini, A. and R.J. Farris, *Mechanical behavior of electrospun polyurethane.* Polymer, 2003. **44**(22): p. 6857-6862.
47. Lee, K.H., et al., *Mechanical behavior of electrospun fiber mats of poly(vinyl chloride)/polyurethane polyblends.* Journal of Polymer Science Part B-Polymer Physics, 2003. **41**(11): p. 1256-1262.
48. Vats, A., et al., *Embryonic stem cells and tissue engineering: delivering stem cells to the clinic.* Journal of the Royal Society of Medicine, 2005. **98**(8): p. 346-350.
49. Willerth, S.M., et al., *The effects of soluble growth factors on embryonic stem cell differentiation inside of fibrin scaffolds.* Stem Cells, 2007. **25**(9): p. 2235-2244.
50. Lopez-Gonzalez, R. and I. Velasco, *Therapeutic Potential of Motor Neurons Differentiated from Embryonic Stem Cells and Induced Pluripotent Stem Cells.* Archives of Medical Research, 2012. **43**(1): p. 1-10.
51. Li, W., K. Jiang, and S. Ding, *Concise review: A chemical approach to control cell fate and function.* Stem cells, 2012. **30**(1): p. 61-8.
52. Engler, A.J., et al., *Matrix elasticity directs stem cell lineage specification.* Cell, 2006. **126**(4): p. 677-689.
53. Christopherson, G.T., H. Song, and H.Q. Mao, *The influence of fiber diameter of electrospun substrates on neural stem cell differentiation and proliferation.* Biomaterials, 2009. **30**(4): p. 556-564.
54. Keung, A.J., et al., *Rho GTPases mediate the mechanosensitive lineage commitment of neural stem cells.* Stem cells, 2011. **29**(11): p. 1886-97.

55. Mahairaki, V., et al., *Nanofiber Matrices Promote the Neuronal Differentiation of Human Embryonic Stem Cell-Derived Neural Precursors In Vitro.* Tissue Engineering Part A, 2011. **17**(5-6): p. 855-863.
56. Dash, T.K. and V.B. Konkimalla, *Poly-epsilon-caprolactone based formulations for drug delivery and tissue engineering: A review.* Journal of Controlled Release, 2012. **158**(1): p. 15-33.
57. Subramanian, C., et al., *The melt electrospinning of polycaprolactone (PCL) ultrafine fibers.* Polymer-Based Smart Materials - Processes, Properties and Application, 2009. **1134**: p. 229-234.
58. Qiang-Sun Zheng, D.-B.O., Xiong-Tao Liu and Jing-Jing Guo, *Maintaining Embryonic Stem Cells*
and Induced Pluripotent Stem Cells, Embryonic Stem Cells: The Hormonal Regulation of Pluripotency and
*Embryogenesis*April, 2011: IN TECH. 672.
59. Bain, G., et al., *Embryonic Stem-Cells Express Neuronal Properties in-Vitro.* Developmental Biology, 1995. **168**(2): p. 342-357.
60. Haynes, W.M., *the CRC Handbook of Chemistry and Physics* 93RD Edition, 2012. **Chemical Rubber Company**.
61. Ronald P. Danner, M.S.H., *Handbook of Polymer Solution Thermodynamics.* Design Institute for Physical Property Data (DIPPR), American Institute of Chemical Engineers, 1993.
62. Huang, Z.M., et al., *A review on polymer nanofibers by electrospinning and their applications in nanocomposites.* Composites Science and Technology, 2003. **63**(15): p. 2223-2253.
63. Croisier, F., et al., *Mechanical testing of electrospun PCL fibers.* Acta Biomaterialia, 2012. **8**(1): p. 218-224.
64. Liao, T.Y., S. Adanur, and J.Y. Drean, *Predicting the mechanical properties of nonwoven geotextiles with the finite element method.* Textile Research Journal, 1997. **67**(10): p. 753-760.
65. Willerth, S.M. and S.E. Sakiyama-Elbert, *Cell therapy for spinal cord regeneration.* Advanced Drug Delivery Reviews, 2008. **60**(2): p. 263-276.
66. Oh, S., et al., *Stem cell fate dictated solely by altered nanotube dimension.* Proceedings of the National Academy of Sciences of the United States of America, 2009. **106**(7): p. 2130-2135.
67. Paul D. Dalton, C.V., Brooke L. Farrugia, Tim R. Dargaville, Toby D. Brown and Dietmar W. Hutmacher, *Electrospinning and additive manufacturing: converging technologies.* Biomaterials, 2013. **1**: p. 171-185.
68. Dalton, P.D., et al., *Patterned melt electrospun substrates for tissue engineering.* Biomedical Materials, 2008. **3**(3).
69. Ko, J., et al., *Fabrication of poly (-caprolactone) microfiber scaffolds with varying topography and mechanical properties for stem cell-based tissue engineering applications.* Journal of biomaterials science. Polymer edition, 2013.
70. Feng, J.J., *The stretching of an electrified non-Newtonian jet: A model for electrospinning.* Physics of Fluids, 2002. **14**(11): p. 3912-3926.
71. Feng, J.J., *Stretching of a straight electrically charged viscoelastic jet.* Journal of Non-Newtonian Fluid Mechanics, 2003. **116**(1): p. 55-70.

72. Buchko, C.J., et al., *Processing and microstructural characterization of porous biocompatible protein polymer thin films.* Polymer, 1999. **40**(26): p. 7397-7407.
73. Lyons J.M., M.-e.o.T.P.A.E.a.T.A., Thesis, Doctor of Philosophy, October 2004.
74. Megelski, S., et al., *Micro- and nanostructured surface morphology on electrospun polymer fibers.* Macromolecules, 2002. **35**(22): p. 8456-8466.
75. Lee, J.S., et al., *Role of molecular weight of atactic poly(vinyl alcohol) (PVA) in the structure and properties of PVA nanofabric prepared by electrospinning.* Journal of Applied Polymer Science, 2004. **93**(4): p. 1638-1646.
76. Ogata, N., et al., *Melt-electrospinning of poly(ethylene terephthalate) and polyalirate.* Journal of Applied Polymer Science, 2007. **105**(3): p. 1127-1132.
77. Sarkar, S., et al., *Fabrication of a layered microstructured polycaprolactone construct for 3-D tissue engineering.* Journal of Biomaterials Science-Polymer Edition, 2008. **19**(10): p. 1347-1362.
78. Agarwal, S., J.H. Wendorff, and A. Greiner, *Use of electrospinning technique for biomedical applications.* Polymer, 2008. **49**(26): p. 5603-5621.
79. Min, B.M., et al., *Electrospinning of silk fibroin nanofibers and its effect on the adhesion and spreading of normal human keratinocytes and fibroblasts in vitro.* Biomaterials, 2004. **25**(7-8): p. 1289-97.
80. Zhmayev, E., D. Cho, and Y.L. Joo, *Modeling of melt electrospinning for semi-crystalline polymers.* Polymer, 2010. **51**(1): p. 274-290.
81. Zhrnayev, E., H. Zhou, and Y.L. Joo, *Modeling of non-isothermal polymer jets in melt electrospinning.* Journal of Non-Newtonian Fluid Mechanics, 2008. **153**(2-3): p. 95-108.
82. Dash, T.K. and V.B. Konkimalla, *Poly-small je, Ukrainian-caprolactone based formulations for drug delivery and tissue engineering: A review.* Journal of controlled release : official journal of the Controlled Release Society, 2012. **158**(1): p. 15-33.
83. He, J.H., et al., *Mathematical models for continuous electrospun nanofibers and electrospun nanoporous microspheres.* Polymer International, 2007. **56**(11): p. 1323-1329.
84. Ziabicki, A., *High-Speed Fiber Spinning*. 2nd ed1991: Kreiger.
85. Raleigh, X.L., in *Dublin Philosophy*1884, Edinburgh: London. p. 184.
86. Junghyuk Ko, N.K.M., Patrick C.D. Lee, Stephanie M. Willerth, and Martin B. Jun, *Parametric Studies of Melt Electrospinning Poly ε (caprolactone) Fibers for Tissue Engineering Applications*, in *8th International Conference on Micro Manufacturing*2013: Victoria B.C. Canada.
87. Hohman, M.M., et al., *Electrospinning and electrically forced jets. I. Stability theory.* Physics of Fluids, 2001. **13**(8): p. 2201-2220.
88. Hohman, M.M., et al., *Electrospinning and electrically forced jets. II. Applications.* Physics of Fluids, 2001. **13**(8): p. 2221-2236.
89. Chung, S., et al., *Bioresorbable elastomeric vascular tissue engineering scaffolds via melt spinning and electrospinning.* Acta Biomaterialia, 2010. **6**(6): p. 1958-67.
90. Brown, T.D., P.D. Dalton, and D.W. Hutmacher, *Direct Writing By Way of Melt Electrospinning.* Advanced Materials, 2011. **23**(47): p. 5651-+.
91. Nagy, Z.K., et al., *Solvent-free melt electrospinning for preparation of fast dissolving drug delivery system and comparison with solvent-based electrospun*

and melt extruded systems. Journal of Pharmaceutical Sciences, 2013. **102**(2): p. 508-517.

92. Zhou, H.J., T.B. Green, and Y.L. Joo, *The thermal effects on electrospinning of polylactic acid melts.* Polymer, 2006. **47**(21): p. 7497-7505.
93. Farrugia, B.L., et al., *Dermal fibroblast infiltration of poly(epsilon-caprolactone) scaffolds fabricated by melt electrospinning in a direct writing mode.* Biofabrication, 2013. **5**(2).
94. Karchin, A., et al., *Melt electrospinning of biodegradable polyurethane scaffolds.* Acta Biomaterialia, 2011. **7**(9): p. 3277-3284.
95. Ko, J., et al., *Fabrication of poly (-caprolactone) microfiber scaffolds with varying topography and mechanical properties for stem cell-based tissue engineering applications.* Journal of biomaterials science. Polymer edition, 2014. **25**(1): p. 1-17.
96. Mazalevska, O., M.H. Struszczyk, and I. Krucinska, *Design of vascular prostheses by melt electrospinning-structural characterizations.* Journal of Applied Polymer Science, 2013. **129**(2): p. 779-792.
97. Ren, J., et al., *Melt-electrospun polycaprolactone strontium-substituted bioactive glass scaffolds for bone regeneration.* Journal of biomedical materials research. Part A, 2014. **102**(9): p. 3140-53.
98. Brown, T.D., et al., *Design and Fabrication of Tubular Scaffolds via Direct Writing in a Melt Electrospinning Mode.* Biointerphases, 2012. **7**(1-4).
99. Hao, M.F., et al., *Factors influencing diameter of polypropylene fiber in melt electrospinning.* Advanced Polymer Science and Engineering, 2011. **221**: p. 129-134.
100. Li, X.Y., et al., *Preparation and characterization of poly(epsilon-caprolactone) nonwoven mats via melt electrospinning.* Polymer, 2012. **53**(1): p. 248-253.
101. Hao, M.F., et al., *Experimental study of melt electrospinning in parallel electrical field.* Advanced Polymer Science and Engineering, 2011. **221**: p. 111-116.
102. Mota, C., et al., *Melt electrospinning writing of three-dimensional star poly(E-caprolactone) scaffolds.* Polymer International, 2013. **62**(6): p. 893-900.
103. Dalton, P.D., et al., *Melt electrospinning of poly-(ethylene glycol-block-epsilon-caprolactone).* Biotechnology journal, 2006. **1**(9): p. 998-1006.
104. Deng, R.J., et al., *Melt Electrospinning of Low-Density Polyethylene Having a Low-Melt Flow Index.* Journal of Applied Polymer Science, 2009. **114**(1): p. 166-175.
105. Kong, C.S., et al., *Effects of the Spin Line Temperature Profile and Melt Index of Poly(propylene) on Melt-Electrospinning.* Polymer Engineering and Science, 2009. **49**(2): p. 391-396.
106. Nayak, R., et al., *Effect of viscosity and electrical conductivity on the morphology and fiber diameter in melt electrospinning of polypropylene.* Textile Research Journal, 2013. **83**(6): p. 606-617.
107. Wang, X.N., et al., *Study on Technological Parameters Effecting on Fiber Diameter of Melt Electrospinning.* Advanced Textile Materials, Pts 1-3, 2011. **332-334**: p. 1550-1556.
108. Ko J, B.S., Mohtaram NK, Willerth SM, Jun MBG, *Using mathematical modeling to control topographical properties of poly (ε-caprolactone) melt electrospun*

scaffolds. Journal of Micromechanics and Microengineering, 2014. **24**(6): p. 065009.

109. Liu, Y., X.H. Li, and S. Ramakrishna, *Melt Electrospinning in a Parallel Electric Field.* Journal of Polymer Science Part B-Polymer Physics, 2014. **52**(14): p. 946-952.
110. Ko, J., et al., *Fabrication of poly (epsilon-caprolactone) microfiber scaffolds with varying topography and mechanical properties for stem cell-based tissue engineering applications.* Journal of Biomaterials Science-Polymer Edition, 2014. **25**(1): p. 1-17.
111. Sill, T.J. and H.A. von Recum, *Electro spinning: Applications in drug delivery and tissue engineering.* Biomaterials, 2008. **29**(13): p. 1989-2006.
112. Reignier, J. and M.A. Huneault, *Preparation of interconnected poly(epsilon-caprolactone) porous scaffolds by a combination of polymer and salt particulate leaching.* Polymer, 2006. **47**(13): p. 4703-4717.
113. Sangwon, C., et al., *Bioresorbable elastomeric vascular tissue engineering scaffolds via melt spinning and electrospinning.* Acta Biomaterialia, 2010. **6**(6): p. 1958-67.
114. Sung Jin, K., et al., *Fabrication and characterization of 3-dimensional PLGA nanofiber/microfiber composite scaffolds.* Polymer, 2010. **51**(6): p. 1320-7.
115. Xiuyan, L., et al., *Preparation and characterization of poly(-caprolactone) nonwoven mats via melt electrospinning.* Polymer, 2012. **53**(1): p. 248-53.
116. Hou, Q.P., D.W. Grijpma, and J. Feijen, *Porous polymeric structures for tissue engineering prepared by a coagulation, compression moulding and salt leaching technique.* Biomaterials, 2003. **24**(11): p. 1937-1947.
117. Liao, C.J., et al., *Fabrication of porous biodegradable polymer scaffolds using a solvent merging/particulate leaching method.* Journal of Biomedical Materials Research, 2002. **59**(4): p. 676-681.
118. Shea, L.D., et al., *Engineered bone development from a pre-osteoblast cell line on three-dimensional scaffolds.* Tissue Engineering, 2000. **6**(6): p. 605-617.
119. Wang, Y.Z., et al., *A novel method for preparing electrospun fibers with nano-/micro-scale porous structures.* Polymer Bulletin, 2009. **63**(2): p. 259-265.
120. Junghyuk Ko, M.B.J., Gabriele Gilardi, Edmund Haslam, Edward J. Park, *Fuzzy PWM-PID control of cocontracing antagonistic shape memory alloy muscle pairs in an artificial finger.* Mechatronics, 2011. **21**(7): p. 1190-1202.
121. Gilardi, G., et al., *A shape memory alloy based tendon-driven actuation system for biomimetic artificial fingers, part II: modelling and control.* Robotica, 2010. **28**: p. 675-687.
122. Bundhoo, V., et al., *A shape memory alloy-based tendon-driven actuation system for biomimetic artificial fingers, part I: design and evaluation.* Robotica, 2009. **27**: p. 131-146.
123. Suh, K.Y., N.L. Jeon, and C. Pang, *Wearable skin sensor using programmable interlocking of nanofibers.* 2013 8th Annual Ieee International Conference on Nano/Micro Engineered and Molecular Systems (Ieee Nems 2013), 2013: p. 132-135.

124. Pandya, H.J., et al., *MEMS based low cost piezoresistive microcantilever force sensor and sensor module.* Materials Science in Semiconductor Processing, 2014. **19**: p. 163-173.
125. Chen, W.H., et al., *A MEMS Based Sensor for Large Scale Force Measurement.* 2013 Ieee/Asme International Conference on Advanced Intelligent Mechatronics (Aim): Mechatronics for Human Wellbeing, 2013: p. 1278-1283.
126. Ahmed, M., et al., *MEMS Force Sensor in a Flexible Substrate Using Nichrome Piezoresistors.* Ieee Sensors Journal, 2013. **13**(10): p. 4081-4089.
127. Shukla, S., et al., *Electrospinning of hydroxypropyl cellulose fibers and their application in synthesis of nano and submicron tin oxide fibers.* Polymer, 2005. **46**(26): p. 12130-12145.
128. Ma, S.D., et al., *Intrinsically conducting polymer-based fabric strain sensors.* Polymer International, 2013. **62**(7): p. 983-990.
129. Tok, J.B.H. and Z.A. Bao, *Recent advances in flexible and stretchable electronics, sensors and power sources.* Science China-Chemistry, 2012. **55**(5): p. 718-725.

Appendix A-Drawing

- Chamber

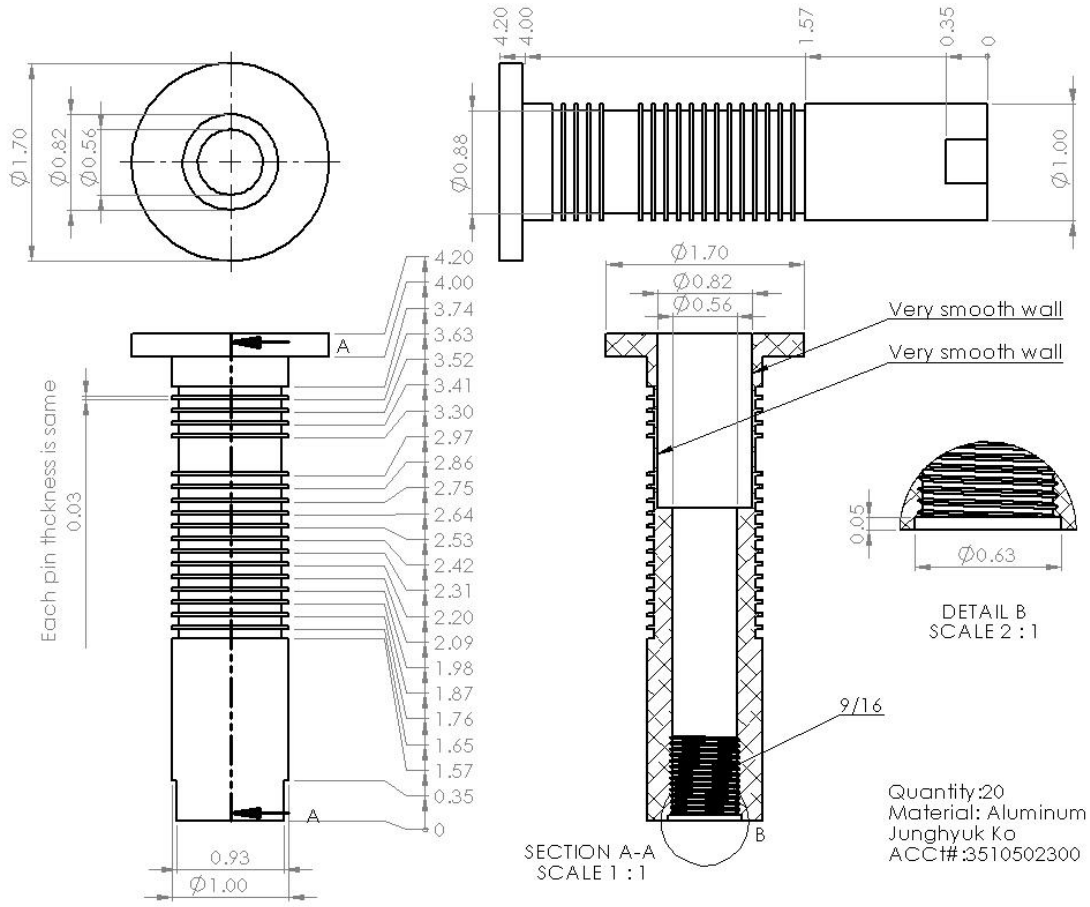

- Plunger

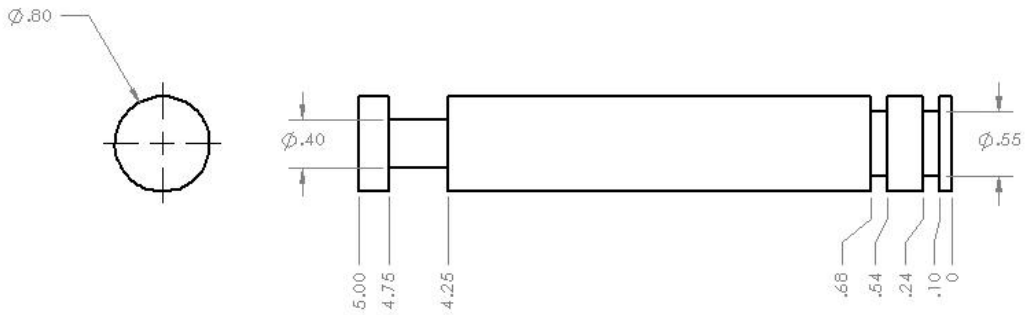

- Nozzle

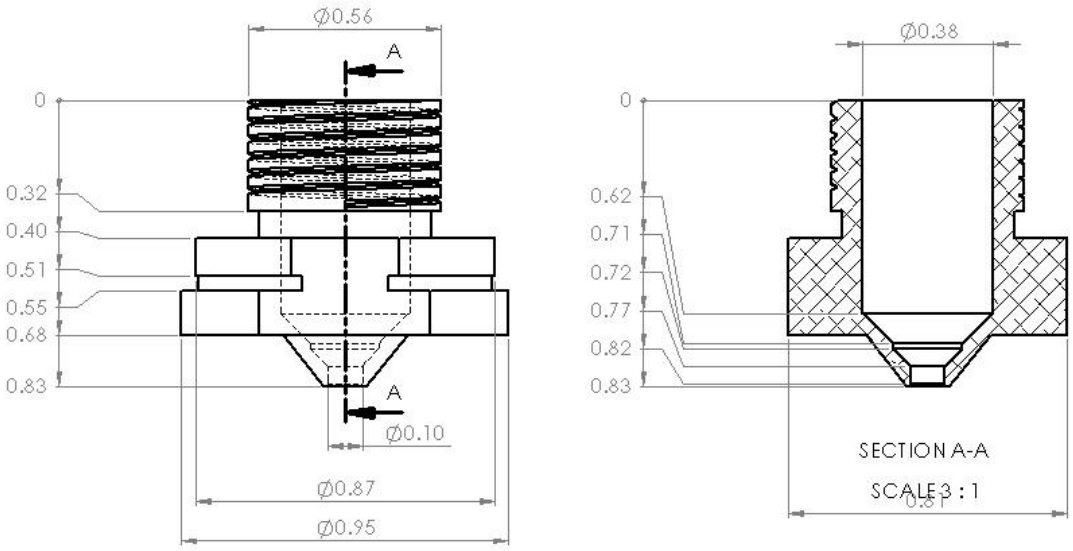

- Fixture for syringe pump

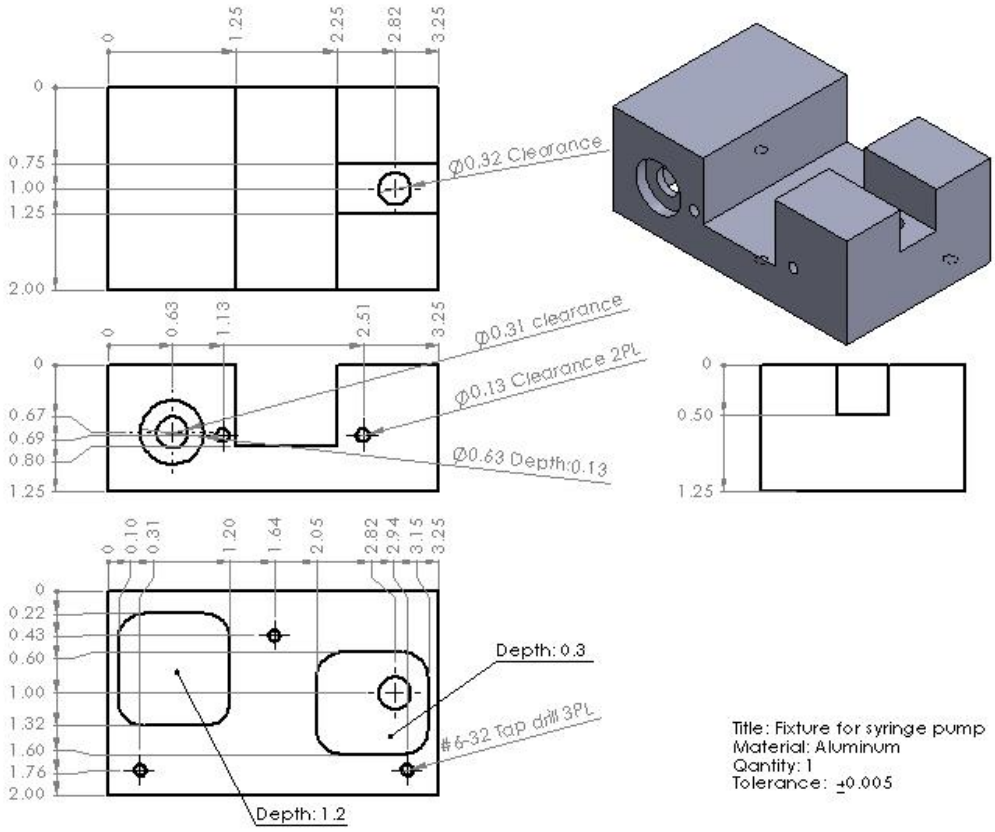

Appendix B-Temperature control system

- Schematic of temperature control system

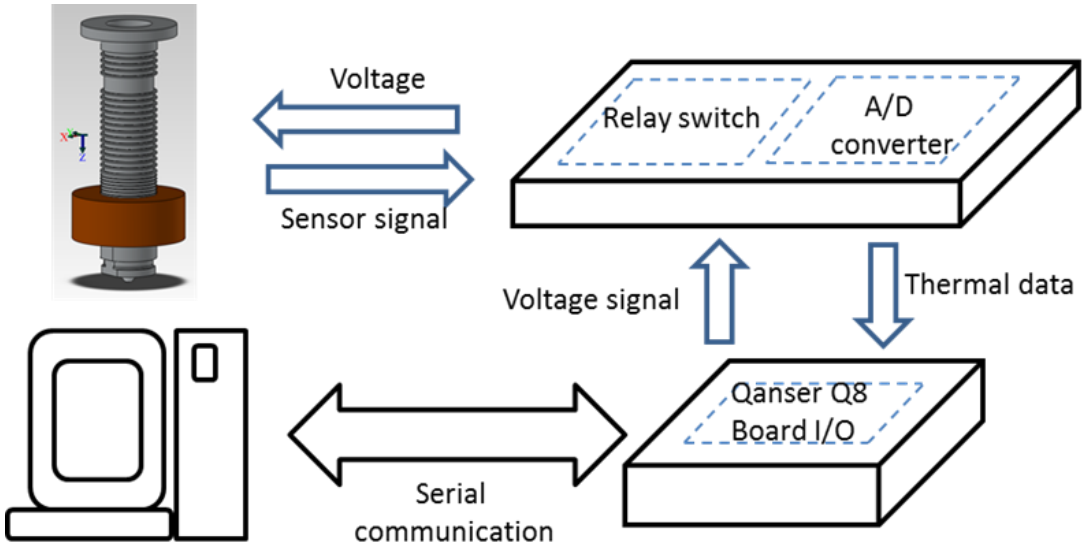

- Temperature control algorithm

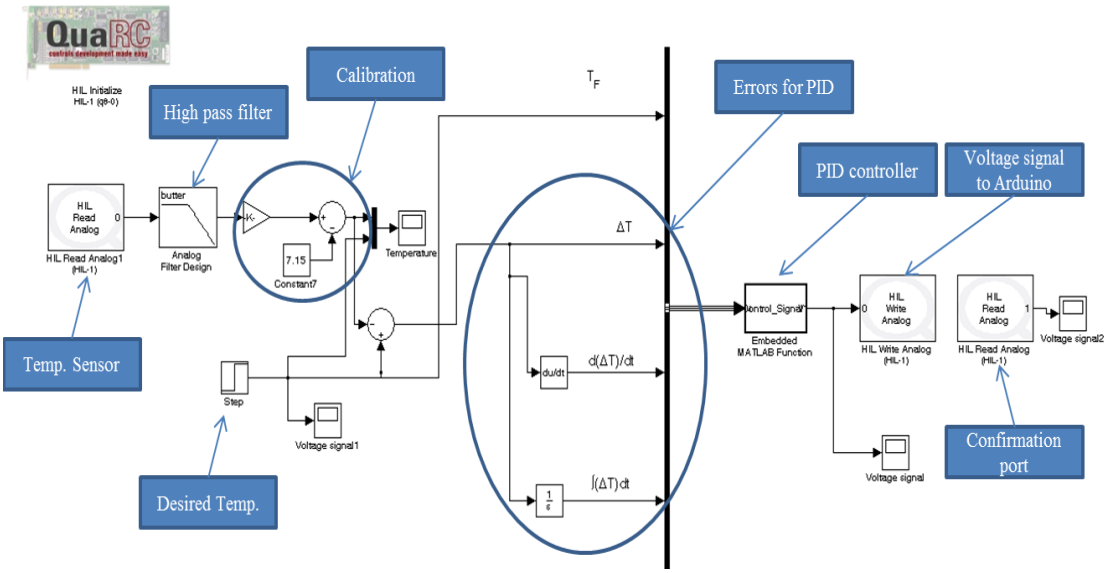

- Voltage signals for temperature control